

# REPORT DOCUMENTATION PAGE

Form Approved  
OMB No. 0704-0188

Public reporting burden for this collection of information is estimated to average 1 hour per response, including the time for reviewing instructions, searching existing data sources, gathering and maintaining the data needed, and completing and reviewing the collection of information. Send comments regarding this burden estimate or any other aspect of this collection of information, including suggestions for reducing this burden, to Washington Headquarters Services, Directorate for Information Operations and Reports, 1215 Jefferson Davis Highway, Suite 1204, Arlington, VA 22202-4302, and to the Office of Management and Budget, Paperwork Reduction Project (0704-0188), Washington, DC 20503.

1. AGENCY USE ONLY (Leave Blank)		2. REPORT DATE 9/3/98		3. REPORT TYPE AND DATES COVERED Final Technical 6/15/96 - 6/14/98	
4. TITLE AND SUBTITLE A Micro Fabricated Motor-Compressor for Fuel Cell Applications				5. FUNDING NUMBERS Grant DAAH04-96-1-0256	
6. AUTHORS A. Ayon, K. Breuer, K-S Chen, F. Ehrich, A. Epstein, L. Frechette, R. Ghodssi, S. Jacobson, J. Lang, C. Lin, K. Lohner, A. Mehra, J. Miranda, S. Nagle, D. Orr, E. Piekos, M. Schmidt, S. Senturia, G. Shirley, M. Spearing, C. Tan, Y. Tzeng, S. Umans					
7. PERFORMING ORGANIZATION NAME(S) AND ADDRESS(ES)  Massachusetts Institute of Technology 77 Massachusetts Ave., 31-264 Cambridge, MA 02139				8. PERFORMING ORGANIZATION REPORT NUMBER	
9. SPONSORING / MONITORING AGENCY NAME(S) AND ADDRESS(ES)  U.S. Army Research Office P.O. Box 12211 Research Triangle Park, NC 27709-2211				10. SPONSORING / MONITORING AGENCY REPORT NUMBER  ARO 35749-2-CH	
11. SUPPLEMENTARY NOTES The views, opinions and/or findings contained in this report are those of the author(s) and should not be construed as an official Department of the Army position, policy, or decision, unless so designated by other documentation.					
12a. DISTRIBUTION / AVAILABILITY STATEMENT  Approved for public release; distribution unlimited.				12b. DISTRIBUTION CODE	
13. ABSTRACT (Maximum 200 words)  This effort is directed at research leading to microfabricated motor-driven compressors suitable for the pressurization of fuel cells in the 50-150 watt range and microblowers (lower pressure rise, high air flows) for instrument aspiration. Micromachined from silicon, these are high power microelectrical and mechanical systems (MEMS). The design performance for the compressor is pumping 0.1 g/sec of air at a pressure ratio of 2:1 while consuming approximately 15-20 watts of electrical power.					
14. SUBJECT TERMS MEMS, turbomachinery, micromotors, micro systems				15. NUMBER OF PAGES 105	
				16. PRICE CODE	
17. SECURITY CLASSIFICATION OF REPORT UNCLASSIFIED	18. SECURITY CLASSIFICATION OF THIS PAGE UNCLASSIFIED	19. SECURITY CLASSIFICATION OF ABSTRACT UNCLASSIFIED		20. LIMITATION OF ABSTRACT UL	

19981222 081

*Gas Turbine Laboratory  
Department of Aeronautics and Astronautics  
Massachusetts Institute of Technology  
Cambridge, MA 02139*

Final Technical Report  
on Grant #DAAH04-96-1-0256

entitled

**A MICROFABRICATED MOTOR-COMPRESSOR  
FOR FUEL CELL APPLICATIONS**

prepared for

US Army Research Office  
P.O. Box 12211  
Research Triangle Park, NC 27709

ATTN: Dr. Richard Paur

**INVESTIGATORS:**

Prof. K. Breuer  
Prof. A. Epstein (Principal Investigator)  
Prof. J. Lang  
Prof. M. Schmidt  
Prof. S. Senturia  
Prof. M. Spearing  
Dr. C. Tan

**AUTHORS:**

A. Ayon	J. Miranda
K. Breuer	S. Nagle
K-S Chen	D. Orr
F. Ehrich	E. Piekos
A. Epstein	J. Protz
L. Frechette	M. Schmidt
R. Ghodssi	S. Senturia
S. Jacobson	G. Shirley
J. Lang	M. Spearing
C. Lin	C. Tan
A. Mehra	S. Umans

August 1998

## SUMMARY

The objective of this research effort is to demonstrate microfabricated micromotor-compressor and blower devices occupying less than a cubic centimeter. The compressor has been sized to provide pressurization for fuel cells in the 50-150 watt range. It consists of an integral silicon micromotor and centrifugal compressor approximately 8 mm in diameter and 1 mm thick. The design flow rate is 0.1 g/sec of air at a pressure ratio of 2:1. The blower is a lower pressure ratio, higher air flow version of the same device. The motor-compressor development is synergistic with an ARO-sponsored effort to develop a micro-gas turbine generator by the year 2000. Also, a compressed gas-driven turbine-generator is being developed as an intermediate milestone/product.

A large fraction of the technology development effort - that for bearings, compressor fluid mechanics, electromechanics, structures, and microfabrication technology - has been common among these devices and projects. The effort is an admixture of research and engineering design since the project goals are device-oriented. The work is nominally divided into six principal topical areas: (1) systems design and integration, (2) turbomachinery fluid dynamics, (3) electrical machinery, (4) structures, (5) bearings, and (6) silicon fabrication technology. This final report summarizes the work of the first two years of this effort. Only the system design and motor electrodynamics are reported in detail. The remainder has been detailed in the annual reports.

The fluid mechanics of the turbomachinery at small scale has been explored with 2-D and 3-D CFD designs of compressors and turbines, and a superscale (75 times size) compressor test rig. The numerical analysis predicted overall compressor efficiencies of about 50%, which have now been confirmed by preliminary rig data. This level of performance is sufficient for a viable compressor or blower and significant improvements may be possible. The analysis shows that the compressor performance is driven primarily by poor diffuser behavior stemming from the 2-D prismatic design constraints imposed by current micromachining technology. At the size range of interest here (millimeter long airfoils), viscous effects (Reynolds number) are of lesser importance. Improved diffuser designs are under investigation. Also, performance has been degraded in the tested design by tip drag and an overly simplified inlet.

High speed turbomachinery requires low friction bearings and freedom from the host of rotor dynamic instabilities which plague high speed rotating machinery. Microturbomachinery is no different in this respect. Preliminary analysis showed that gas bearings have high load bearing capacity at this size scale and are amenable to microfabrication. So, considerable effort was expended on establishing several first principles design and analysis tools for micro-gas bearings including a new 3-D, nonlinear, time-accurate, arbitrary geometry, moving bearing simulation. The analysis suggested that a 10 micron wide, 300-600 micron long journal bearing

should adequately support a 4 mm diameter rotor. Eccentric operation of the rotor within the journal is needed for stability; the design implemented displaces the rotor to 1-2 microns from the wall by an externally imposed side pressurization scheme.

To evaluate gas bearing behavior in the micro regime, a conventionally-fabricated, 26 times scale-up rotordynamics-bearing test rig (with a 4 inch dia. rotor) was built and instrumented to measure time-dependent rotor motion and the pressure distribution within the bearings. This rig has been operated up to about 30% of the scaled design engine operating speed, about 6 times the first critical frequency, in a mixed hydrodynamic-hydrostatic operating mode. Analysis suggested that full-speed operation of this rotor on a hydrodynamic film (the design intent) requires the rotor to be approximately in balance. A full-scale (4 mm diameter) "microbearing test rig", essentially the motor-compressor rotor but without the generator and with turbine rather than compressor airfoils, was constructed and tested. The first die-scale units could operate only at low speed (10,000 rpm) because as fabricated they did not meet the design intent due to manufacturing process limitations. The devices have been redesigned, the necessary manufacturing processes developed at wafer scale, and the manufacturing largely completed.

Electrostatic bearings were examined as an alternative technology to gas bearings. Analysis and simulation showed that electrostatic bearing cannot be engineered to provide sufficient load bearing capability within the microengine design constraints. They can be used to add damping to gas bearings under limited circumstances.

The motor-generator is an electric induction machine which achieves the very high power densities desired from a combination of high rotational speed, high synchronous frequency (3 MHz), and high electric field strength ( $10^8$  v/m). The performance of this type of electrical machine can only be considered in conjunction with the integral power electronics which are required for excitation. Several analytical models of the motor-generator have been formulated to aid in the design process. These models have suggested that a 6 phase, 131 pole (per phase) machine operating at  $\pm 300$  V best meets the motor-compressor design and fabrication constraints. This design requires unusual electrical properties for the rotor conductor and insulator layers. Experiments have shown that properly doped polysilicon can meet these requirements. Construction is under way on a "tethered" micromotor in which the rotor is supported by mechanical flexures so that electrical torque can be measured directly without the complication of bearing and fluid drag forces. The results from this experiment will be used to refine the analytical models and machine designs.

The success of this project is predicated on the ability to fabricate microstructures whose mechanical behavior and complexity were on the very edge of the state-of-the-art at the start of this work, so that much of the effort has been directed toward the development of appropriate



microfabrication technology. Work to date has concentrated on silicon machines and processes. A time-multiplexed deep etcher (TMDE) was purchased under this program and considerable effort expended on developing the methodology for the fabrication of highly anisotropic etched structures which are central to the micromachinery designs being pursued. This research has been very successful, including demonstration of 10 micron wide, 300-600 micron deep channels desired for the microbearing journals. An aligner wafer bonder was also acquired and process development has proceeded on the fabrication of multiwafer, laminated structures. The microbearing test rig (which is also very similar in structure to the motor-compressor and the turbine-generator) has been the central focus of this fabrication technology development. Early die level assemblies did not meet the design intent. The device was redesigned for wafer level fabrication and process development is now in progress. The complete unit requires 14 masks and 4 wafer bonds, making it one of the most complex multiwafer MEMS device ever reported.

Two micromotor-compressors are under development. One with a pressure ratio of two and an air flow of 0.1 g/s is designed for small fuel cell pressurization, and the second as a lower pressure rise (20" of H<sub>2</sub>O) blower. The blower is the technically less challenging since it does not require as high a rotational speed or as much power as does the compressor. The first units to be produced are intended as experimental test units to qualify design codes and serve as proof of principle for several of the technologies, especially the motor. To maximize flexibility, these devices will require external interconnection rather than be self-contained. Although a system optimization suggested that a 6-8 mm rotor diameter would produce the most power, the first devices were designed as 4 mm to maintain commonality with the ongoing bearing and electrical machine development. The first experimental devices are being fabricated and will be tested in 1998.

## 1.0 SYSTEM DESIGN AND INTEGRATION

This report describes the development status of an integrated electric micromotor-driven compressor. This microfabricated device is to provide a source of pressurized gas, operating from an electrical power source. This system shares technology with the other microengine projects at MIT. This report focuses on the technology developed for the micromotor-compressor project, specifically system design and electromechanics. Details relating to bearings and microfabrication can be found in the annual progress reports [1].

This device serves two distinct but overlapping roles in the micro-engine program. The first role of the motor-compressor is to be used as a stand-alone device to supply small amounts of pressurized gas. Applications such as the pressurization of fuel cells in the 50-150 W size range could require about 0.1 g/s of air at a relatively high pressure rise of 2 atm or more. A different application is aspiration for analytical instruments such as air samplers. This requires less pressure rise (20 inches of H<sub>2</sub>O). In the latter version, the motor-compressor can be more properly thought of as a microblower. Second, it allows the incremental integration of electric components (the motor) with mechanical components (turbomachinery and bearings) and will be one of the most complex MEMS devices ever fabricated.

The micromotor-compressor development plan starts with the design, fabrication and testing of a set of experimental devices to establish the operational characteristics of various aspects of the motor-compressor system. This process is then iterated to evolve the configuration into one which meets application requirements. The experimental devices consist of: 1) a micromotor test rig (non-rotating rotor held by flexible tethers to "access" the electric motor) design, fabrication and operation, and 2) a rotating version of the micromotor, incorporating the electric motor with air bearings and turbomachinery. Currently, the experimental devices have been designed and the fabrication masks drawn, and motor fabrication is on-going. At this stage of the program (June 1998), the primary technical concerns are: 1) the relatively high level of viscous dissipation of the air in the motor gap, which reduces the power available for compression and generates excess heat; 2) the micro-electrostatic motor has not yet been demonstrated in the lab; and 3) not all fabrication techniques necessary to build the motor have been developed. These issues will be addressed experimentally during the coming year. Development of the fabrication techniques necessary for the motor-compressor is ongoing and fabrication of the first set of experimental devices should take place in the second half of 1998, as will operation of the tethered-motor. Testing is planned through the end of 1998.

In the following sections, the micro-compressor components are described and models of their performance are summarized. The operational requirements and constraints characterizing this type of device are presented, followed by the experimental device configurations and the system trade-offs that guide the design of a motor-compressor. The fabrication process and main fabrication issues are then discussed, followed by a description of the electromechanical

development, including the tethered motor. Finally, the work plan is summarized.

### 1.1 Overall System Description

The motor-compressor is composed of the following components, illustrated in the schematic cross-section (Fig. 1.1):

1. Radial impeller and diffuser
2. Journal and thrust bearings
3. Electrostatic induction motor
4. Fluid piping and electrical connections

At the completion of the fabrication process, the motor-compressor is composed of only two parts: the static structure and the rotor. The in-plane motion of the rotor disk is supported by a gas journal bearing on its periphery, while the axial loads are borne by thrust bearings on each side of the disk. The electrostatic induction motor applies the torque through a thin resistive layer on the backside of the disk. This applied torque spins the rotor, and therefore the impeller blades. The radial pressure gradient created by the impeller entrains inlet air and then discharges it to an external load.

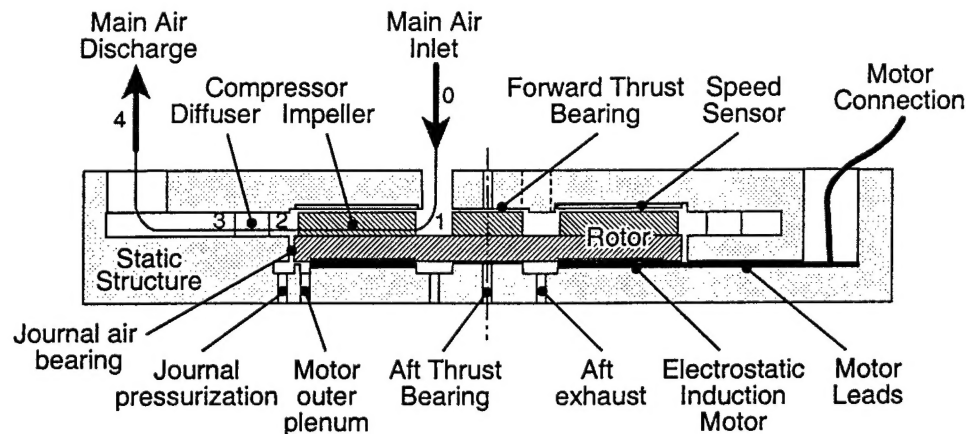


Fig. 1.1: Schematic of motor-compressor cross-section illustrating the main system components.

### 1.2 Performance Modeling

To define the dimensions and operating parameters of the motor-compressor, simple models of the system components have been developed as an aid to matching the components and determining the overall behavior of the complete system.

#### 1.2.1 Power Balance

At design conditions, the system must be sized such that the power delivered by the motor is sufficient to drive the compressor and overcome all the viscous losses in the system. To

explore design trade-offs, the power accounting is viewed in terms of the torque balance on the rotor. The main metric is the net power available for compression, which is equal to the net mechanical power supplied by the motor minus the viscous losses in the bearings and on the back side of the rotor.

$$P_{comp} = P_{motor} - P_{visc}$$

The viscous losses are estimated from models of the components from which they arise, defining the net power. The tip clearance losses in the compressor and the viscous dissipation in the motor gap are attributed to the compressor and motor respectively. Efficiency of the system is determined by these component efficiencies and the other losses such as inlet and discharge pressure drops, power electronics resistive losses, and heat transfer to or from the main flow. The following sections describe the modeling of each system element.

### 1.2.2 Compressor

The net power consumed by the compressor is equal to the sum of the compression work done on the flow plus the viscous dissipation such as the clearance over the tip of the impeller blades:

$$P_{comp} = \dot{W}_{comp} + \dot{W}_{visc,tip}$$

$$\dot{W}_{comp} = \dot{m} \cdot C_p (T_{t,3} - T_{t,1})$$

where compression work is defined as the product of the mass flow and enthalpy rise across the compressor. The flows in the tip clearance region have a combined effect of modifying the fluid turning across the impeller (i.e. the compression work) and generating viscous losses. Tip clearance flows are an active area of research in the turbomachinery community. So for design purposes, their effect will be simply represented by a lowered compressor efficiency (an equivalent higher total temperature rise for a specific pressure rise):

$$\eta_{comp} = \frac{\left( \frac{P_{t,3}}{P_{t,1}} \right)^{(\gamma-1)/\gamma} - 1}{\left( \frac{T_{t,3}}{T_{t,1}} \right) - 1}$$

The impeller and diffuser blade designs used for the motor-compressor are described in the progress reports. These designs have been investigated numerically and tested experimentally at high rotation speeds, demonstrating pressure ratios in excess of 2:1 at 400 m/s peripheral speed. The compression power is predicted to be approximately 9 to 10 watts at an air flow rate of 0.1 g/s. Net compression power, and therefore pressure rise, are approximately quadratic functions of rotational speed.

### 1.2.3 Electrostatic Induction Motor

The net power delivered by the motor is calculated by first determining the electrostatic torque, then subtracting the viscous drag in the motor gap. The net motor power is represented as:

$$P_{motor} = P_{elec} - \dot{W}_{visc,motor}$$

$$P_{elec} = T_{elec}\Omega$$

As described in Section 2.0, a small motor gap is desired for large electrical powers; however, the viscous drag in the motor gap increases as the gap is reduced. Accurate modeling of electrical and fluid aspects of the motor is necessary to produce an optimized design. This modeling effort is described in Appendices A and B respectively.

#### 1.2.3.1 Electrostatic Torque

The discrete-electrode, quasi-steady model of the electrical machine is used to predict the motor electrical power for the motor-compressor design purposes (see Section 2.0).

#### 1.2.3.2 Motor Gap Viscous Torque

Since the viscous dissipation in the motor gap limits viable motor-compressor designs, it has been studied in greater depth than other fluid loss sources. This section summarizes this analysis. More details are presented in Appendix B.

In general terms, the motor gap can be modeled as an annular disk extending from  $r_{mi}$  to  $r_{mo}$ , rotating over a flat surface (the electrode surface). Static pressures are imposed at the outer radius ( $P_{mo}$ ) and inner radius ( $P_{mi}$ ), with  $P_{mo} > P_{mi}$  for the nominal motor-compressor configuration. At ambient pressure, rarefaction of the air is important for gaps of less than 1 micron. Since the gap here is chosen to be in the 1-5 micron range for operability considerations, the fluid can be treated as a continuum and thus modeled by the Navier-Stokes equations. Two different gap geometries are described in this section: a gap with a smooth wall electric stator (electrode surface) and a gap with a radial channel stator.

**Smooth stator** - Both tangential and radial velocity components are of interest in the gap. The radial velocities define the mass flow through the motor gap, while the tangential velocities near the disk surface define the viscous torque. An order of magnitude analysis shows that viscous effects dominate the motor gap flow. The inertial terms (including Coriolis and centrifugal forces) do not affect the tangential velocity profile, such that the tangential component of the Navier-Stokes equations reduces to a simple Couette flow:

$$\frac{\partial \tau_{\theta}}{\partial z} = 0 \rightarrow \tau_{\theta} = \mu \frac{\partial V_{\theta}}{\partial z} = \mu \frac{\Omega r}{g_m}$$

The fluid shear stress ( $\tau_\theta$ ) is therefore a linear function of radius ( $r$ ), rotational speed ( $\Omega$ ), and viscosity ( $\mu$ ); and is inversely proportional to the motor gap height ( $g_m$ ). The total viscous drag or torque in the motor gap is the integral from the inner to outer radius of the shear stress times radius and times area ( $A$ ):

$$T_{g_m} = \int_{r_{mi}}^{r_{mo}} r \cdot \tau_\theta dA = \mu \frac{\pi \Omega}{2 g_m} (r_{mo}^4 - r_{mi}^4)$$

The power dissipated in the motor is then:

$$\dot{W}_{visc, g_m} = T_{g_m} \cdot \Omega = \tau = \mu \frac{\pi \Omega^2}{2 g_m} (r_{mo}^4 - r_{mi}^4) \quad (1.1)$$

The effects of rotation were confirmed to be negligible by a numerical calculation of the motor gap flows. These CFD calculations have also shown that the flow entering the motor gap at the outer radius is rapidly spun up to the disk speed, i.e. the radial inertia in the entrance region is negligible. A simple Couette flow approximation is therefore appropriate for modeling the flow in the gap region of a micromotor with a smooth wall (electrode surface). Appendix B presents an expanded discussion on the effects of rotation and discusses the validity of this approximation.

**Grooved stator** - The electrode fabrication techniques planned will not result in a smooth stator, since the electrodes are to be formed by patterning a 1 micron thick polysilicon layer. Also, etching trenches deeper than 1 micron between the electrodes can reduce the viscous drag in the motor gap. A more realistic motor gap geometry is therefore a disk rotating over several hundred thin radial trenches, whose depth is a design variable. Viscous CFD calculations of the flow in a motor gap with a grooved stator were performed to quantify the influence of these trenches on drag. Comparison of 2-D and 3-D solutions has shown that the radial flow and effects of rotation do not significantly affect the drag predicted, so that the 3-D domain can be decomposed as 2-D sections, normal to the radial direction. Figure 1.2 shows such a 2-D section, labeled with parameters describing the geometry at a given radius: the motor gap height ( $g_m$ ), the electrode and trench widths ( $w_e$  and  $w_t$  respectively) and the trench depth ( $h_t$ ).

The drag on the rotor for such a configuration can be characterized in terms of four non-dimensional parameters, including the duty-cycle ( $dc$ ) and the gap Reynolds number ( $Re_g$ ):

$$l^* = \frac{l}{g_m}; \quad h^* = \frac{h_t}{g_m}; \quad dc = \frac{w_e}{w_e + w_t}; \quad Re_g = \frac{\rho \Omega r g_m}{\mu}$$

The design graphs using these parameters are presented in the appendix. The drag reduction in percent from the smooth stator case are shown as a function of the three first non-dimensional parameters:  $l^*$ ,  $h^*$ , and  $dc$  (initial analysis have shown that the gap Reynolds number has little

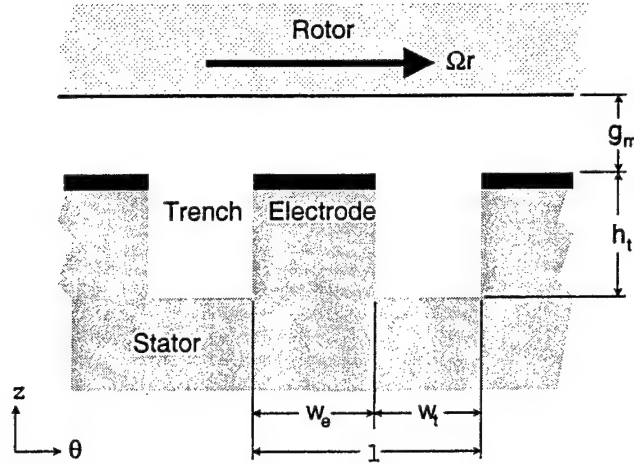


Fig. 1.2: Trenched stator cross-section at a given radius,  $r$ .

influence on the drag). We note that drag is always reduced by the presence of inter-electrode trenches, and that deeper, wider trenches produce greater drag reductions. This suggests that a trade-off exists between drag and electrical power. Experimental results will be used to assess this further.

#### 1.2.4 Thrust Bearings

The first set of experimental motor-compressor devices has been designed with hydrostatic thrust bearings. The drag in this type of thrust bearings can be approximated with the same model as used for the drag in the motor gap with a smooth stator (Eq. (1.1)). Once again, the tangential flow is dominated by viscous effects, such that Couette flow is a good model.

#### 1.2.5 Journal Bearing

The journal bearing nominally operates at a relatively high eccentricity ( $\epsilon$ ), generating circumferential pressure gradients. The tangential velocity profile between the rotor outer rim and the stationary journal wall (distance,  $c$ ) is therefore a superposition of Couette and Poiseuille flows. Since the pressure is periodic around the annulus, the increase in drag on the disk in the positive pressure gradient region on the annulus was found to compensate a decrease in drag in the adverse pressure gradient region. Thus, the drag torque ( $T_{jb}$ ) can be predicted approximately by integrating the shear stress due to a pure Couette flow around an off-centered rotor:

$$T_{jb} = \frac{2\pi}{\sqrt{1-\epsilon^2}} \mu \Omega r_{jb}^3 \frac{l}{c}$$

$$\dot{W}_{visc,jb} = T_{jb} \cdot \Omega = \frac{2\pi}{\sqrt{1-\epsilon^2}} \mu (\Omega r_{jb})^2 r_{jb} \frac{l}{c}$$



This approximation has been shown to be applicable to the current hydrodynamic journal bearing configurations [2]. Further analysis is however required in order to model the effects on drag of flow unsteadiness and any hydrostatic forces in the journal bearing.

#### **1.2.6 Aft Plenums and Seal**

Other areas on the aft side of the disk will also generate viscous losses, which must be accounted for in the power balance. To reduce the drag on these areas, the local stator-rotor gaps are increased as much as possible. In the plenum areas, the drag is then small and can be simply modeled as fully-developed Couette flow (Eq. (1.1)). The velocity profile over the seal is also assumed to be Couette flow.

### **1.3 System Design Considerations**

This section addresses the principal system issues that impose requirements and constraints on the operation of a micromotor-compressor. The performance models previously described with these constraints are then used to arrive at an experimental device configuration. Finally, design trade-offs are discussed in light of future design refinements needed to meet application requirements.

#### **1.3.1 Operational Requirements and Constraints**

Many issues guide and constrain the motor-compressor design space, including thermal balance, disk deflection, mechanical integrity, axial force balance and positional stability, and motor electrical limitations. These are described in the following sections.

##### **1.3.1.1 Thermal Balance**

At high-speed, power dissipated in small air gaps produces considerable heat which will increase the temperature of both the fluid and structure. The viscous dissipation in the motor gap can be of the same order as the motor electrical power (which would result in zero net motor power output). High temperature operation is undesirable from many standpoints: 1) gas viscosity is larger, increasing loss; 2) rotor creep rates increase; 3) motor electrical properties can drift, and 4) the structure may lose mechanical integrity. Due to the high conductivity of silicon and the short length scales, the micromotor-compressor components will reside at approximately uniform temperature (different for the rotor than the static structure however). Initial analysis predicts that the rotor will equilibrate at a temperature of 40-50°C above that of the static structure. The temperature level is governed by the heat transfer rates to the air within the motor-compressor (the main flow) and to the device surroundings. The precise distribution of the heat sources (such as the motor gap) is not important since the high conductivity of silicon and small length scales essentially create a thermal short across the structure. The main air flow through the impeller and

the diffuser serves to cool both the rotor and the static structure. Additional cooling of the static structure, and consequently the rotor, can be accomplished through convection or conduction to the surroundings. The secondary flows (such as bearing pressurization air) are not useful for cooling since these mass flows (and thus their heat convection capacities) are small. Preliminary analyses show that the static structure operating temperature will vary between 300 and 600 K depending on the external boundary conditions. Acceptable operating temperatures will be guaranteed for the first experimental devices through controlled external cooling. Results from these experiments will suggest strategies for achieving appropriate temperatures in a packaged micromotor-compressor.

#### 1.3.1.2 Stress and Mechanical Deflection Considerations

Mechanical integrity of the rotating structure and the deformation under centrifugal loads are always a concern for high-speed rotating machinery. The micromotor-compressor is especially sensitive to out-of-plane deflection since a rotor 4000 microns in diameter is enclosed within micron gap thrust bearings and incorporates in a motor with a 3 micron gap. The rotor structural integrity was analyzed using finite element modeling last year (ARO Progress Report, 1996) for the macro-compressor test rig. When scaled for the motor-compressor rotor, the analysis suggests acceptable maximum stresses (at the blade leading edges, the most critical region) and rim deflections of 0.37 micron at 200 m/s rim speed. This deflection is about 10% of the motor gap. In nominal operation, a clearance of 1.1 microns will remain underneath the disk at the outer radius, i.e. between the disk and the seal. Higher rotational speed devices will require greater attention to the issue of disk deformation.

#### 1.3.1.3 Axial Balance and Stability

Air bearings have been incorporated into the design to enable operation at high rotational speeds. Ideally, these bearings must support the sum of all the loads on the rotor (including rotordynamic, gyroscopic, pressure, and electrostatic) to insure that the rotor remains centered. This is difficult to achieve in the area available. As is commonly done in high speed machinery, a pressurized chamber is provided on the back side of the rotor to relieve some of the static load, in this case to cancel out the electrostatic attractive force of the motor ( $\sim 0.5$  N). The pressure will be set in this plenum located at the outer radius of the motor (referred to as the "motor outer plenum" in Fig. 1.1), at about 0.5 atm above the compressor discharge pressure. The axial force balance on the disk is conceptually illustrated in Fig. 1.3.

A different strategy will be needed for a packaged motor-compressor since pressurized external air will not be available. Many options exist, such as opposing the electrostatic force with a second motor on a tip shroud, however these increase the fabrication complexity. They

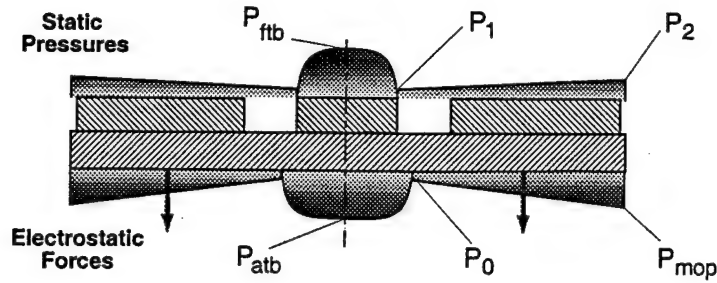


Fig. 1.3: Axial thrust balance of the rotor is accomplished by setting the motor outer plenum pressure ( $P_{mop}$ ) such that the pressure forces are equal and opposite to the electrostatic forces.

have therefore been avoided in the first set of experimental devices.

In transient operation, the disk will not in general remain centered but may be displaced axially. The electrostatic and pressure forces acting on the rotor must provide a net negative spring stiffness to restore the disk to the centered position. The components of axial force sensitive to displacement are the thrust bearings and the motor electrostatic attraction. To ensure an adequate restoring force, the aft thrust bearing diameter was increased from 0.5 mm to 0.7 mm. The resulting change in axial force with the motor gap is shown in Fig. 1.4. It is the sum of the thrust bearing and electrostatic variation of force with distance.

This axial equilibrium problem is a more difficult to resolve for a packaged motor-compressor device, since external air will not be available for the motor outer plenum nor the thrust bearing pressurization. These challenges will be left for the second iteration of micromotor-compressor devices.

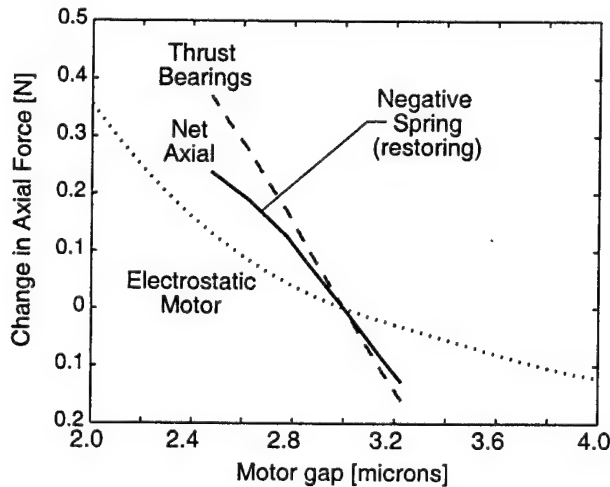


Fig. 1.4: Restoring axial force as a function of the motor gap (nominal motor gap is 3 microns).

#### 1.3.1.4 Motor Electrical Constraints

Several considerations define the practical design space of the motor parameters:

- Electrical breakdown - Pachen's curve for electrical breakdown suggests that an ideal air gap of this order ( 3 microns) should withstand voltage differences up to 350 Volts. Above this, ionization induces breakdown of the electrical fields. The voltage applied between adjacent electrodes must therefore be limited to prevent breakdown, but otherwise maximized since the electrical power delivered is proportional to the square of the voltage.
- Minimum feature size - Fabrication techniques available to create the electrodes limit their width to a few microns. For a given motor inner radius, the maximum number of electrodes is therefore limited. To reduce the fabrication risk, the minimum feature size is taken to be somewhat larger than this fabrication limit.
- Electrical frequency – The maximum operating electrical frequency is limited by the capability to generate the high frequency, high voltage drive signal and deliver it to the distributed electrodes. Power electronics based on available transistors are limited to ~3 MHz, while resonant LC drive circuits promise larger bandwidth. At frequencies higher than 3 MHz however, the phase lag and voltage drop between the first and last electrodes can become significant.

These limitations are currently being investigated analytically and experimentally with microfabricated test structures. For the experimental devices, the following constraints have been adopted: maximum inter-electrode voltage of 300V, minimum feature size of 4 microns, and maximum electrical frequency of 3 MHz.

#### 1.3.2 Experimental Device Configuration

The objectives of the first set of devices fabricated includes development of motor fabrication techniques and demonstration of an electrically-driven, high-speed microfabricated turbomachine. The experimental devices make extensive use of the experience to date of the micro-gas turbine project:

- *Fabrication techniques* developed for the microturbine bearing rig
- *Compressor blade design* investigated numerically and tested experimentally in the macro-scale compressor rig
- *Journal bearing geometry* investigated numerically and analytically and tested experimentally in both the micro and macro bearing rigs
- *Hydrostatic thrust bearings* tested in both micro and macro bearing rigs.

The motor design used here is identical to that of the tethered motor, so that its experimental results are directly applicable. This commonality between the motor-compressor and current microcomponent designs reduces risk on this first iteration. However this reduced risk comes at the price of an unoptimized, relatively low output power device. Although these first experimental devices are not predicted to satisfy the requirement for fuel cell pressurization (2:1 pressure rise at 0.1 g/s), they should be useful for lower pressure rise applications.

Packaging and operating restrictions have also been relieved for the first experimental devices. Similar to the current micro and macro bearing rigs, an external high-pressure air source will be used to supply the hydrostatic thrust bearings, as well as the journal bearing (for side pressurization). External convection and conduction will also be used to cool the devices and allow lower temperature operation, i.e. reduced viscous losses, as needed.

### 1.3.2.1 *Design*

Based on these guidelines and on the operational requirements, the motor-compressor experimental devices were defined. Table 1.1 summarizes the geometric parameters describing the motor-compressor experimental devices.

The device layout illustrated in Fig. 1.5, showing the five etched wafers before assembly, with the electrical layers elevated. Figure 1.6 shows the air flow paths, including the forward thrust bearing supply, the main flow path, the aft thrust bearing supply, the motor outer plenum supply, and the aft exhaust.

**Table 1.1: Design Parameters of the Motor-Compressor Experimental Devices**

Component		
Disk	Outer radius	2 mm
Compressor	Impeller: blade design	MIT-I99 (2:1)
	Number of blades	6 blades
	Blade radial extent	$r = 0.98$ to $1.95$ mm
	Diffuser: blade design	MIT-H36 (2:1)
	Number of blades	11 blades
	Blade radial extent	$r = 2.37$ to $2.96$ mm
Motor	Type	Electrostatic induction
	Number of poles and phases	131 x 6 phases
	Number of electrodes	786 electrodes
	Excitation	$\pm 300$ Volts, sinusoidal
	Gap	3 microns
	Geometry: electrode radial extent	$R = 1$ to $1.9$ mm
	Width	4 to 11.2 microns
	Inter-electrode spacing	4 microns, constant w/ radius
	Rotor insulator thickness	10 microns
Forward thrust bearing	Type	Hydrostatic
	Clearance	1.5 microns
	Outer radius	0.5 mm
	Orifices: number and location	8 @ $r = 0.35$ mm,
	Diameter	10 microns
	Length	100 microns
Aft thrust bearing	Type	Hydrostatic
	Clearance	1.5 microns
	Outer radius	0.7 mm
	Orifices: number and location	8 @ $r = 0.55$ mm,
	Diameter	10 microns
	Length	100 microns
Journal bearing	Type	Hydrostatic/hydrodynamic
	Length	300 microns
	Clearance	10 microns

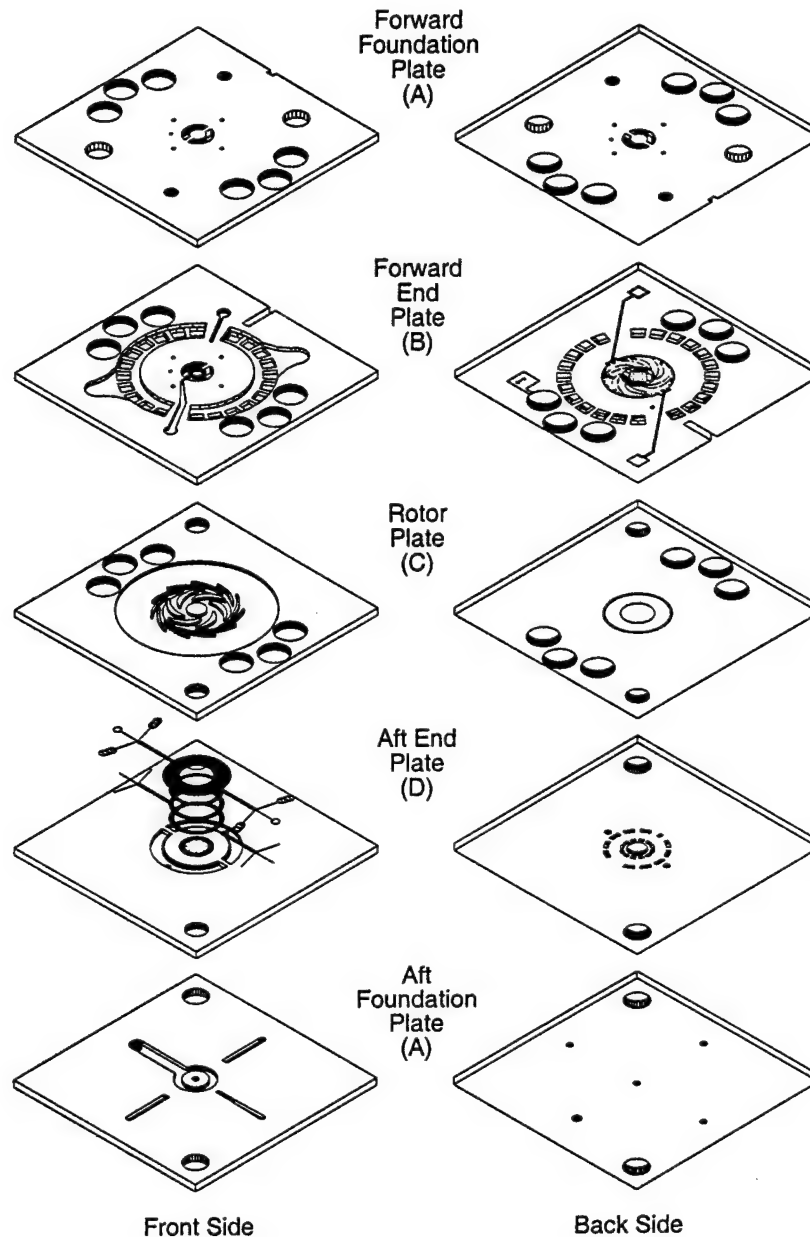


Fig. 1.5: Motor-compressor experimental device assembly drawing.

### 1.3.2.2 *Performance Predictions*

Using the performance models described in Section 1.2, the power available for compression is found to be a maximum of 1.09 W at approximately 200 m/s rim speed. As the speed is increased, viscous losses increase more rapidly than the electrical power. The design speed for the experimental devices was therefore chosen as 200 m/s, 50% of the nominal 400 m/s motor-compressor wheel speed. The breakdown of power consumption of the development device at this speed is summarized in Table 1.2, along with the design point operating parameters.

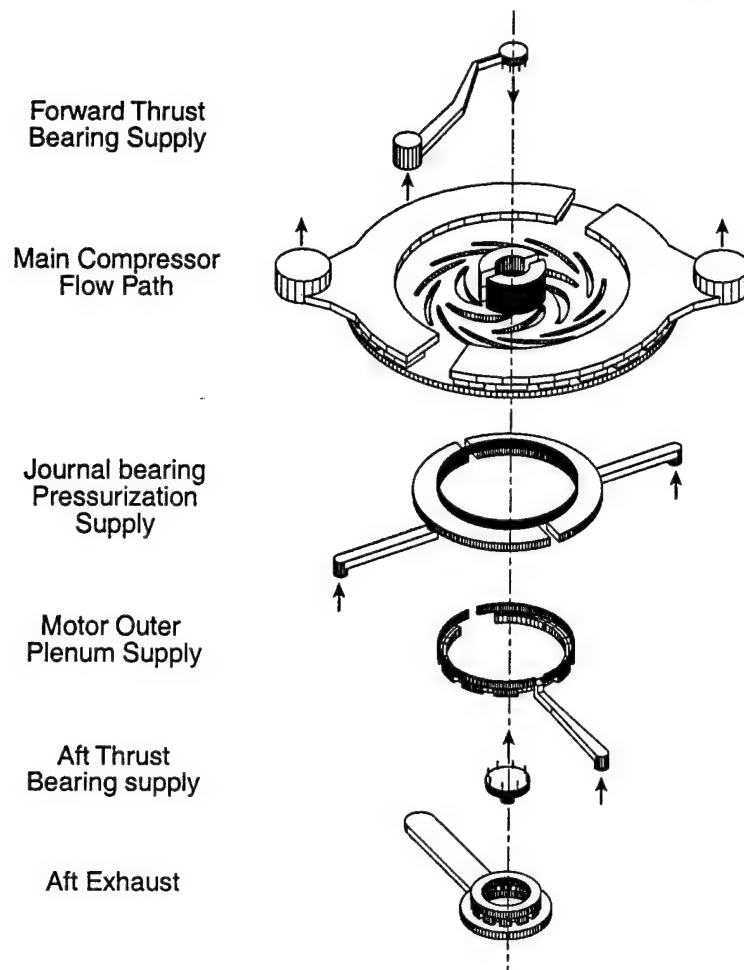


Fig. 1.6: Main and secondary air flow paths.

To ensure the ability to reach high speed even if less power is available than predicted, some rotors will be fabricated without blades. The bladeless devices have a reduced aerodynamic load, so higher rotational speeds should be reached. Measurement of the limiting speed of these bladeless rotors will aid in deducing the distribution of the losses among components. Since the vaned diffuser performance is very sensitive to the inlet swirl angle, and since off-design operation will be explored, devices with bladed rotors will be built in two configurations, with vaned and vaneless diffusers. Thus, three variations of experimental devices will be fabricated:

1. *Vaned diffuser blower*: nominal configuration with both impeller blades and diffuser vanes.
2. *Vaneless diffuser blower*: impeller blades but no diffuser vanes.
3. *Bladeless rotor*: without impeller blades or diffuser vanes.



**Table 1.2: Predicted Design Point Power Balance**

Design point parameters	
Rotational speed	200 m/s
Mass flow	0.05 g/s
Pressure rise: total-to-static	1.09 : 1
total-to-total	1.16 : 1
Compressor power consumed	1.09 W
Net motor power produced	1.99 W
Motor viscous losses	1.07 W
Motor electrical power	3.06 W
Bearing viscous losses	0.48 W
Aft thrust bearing	0.04 W
Forward thrust bearing	0.01 W
Journal bearing	0.43 W
Other viscous losses	0.28 W
Total viscous losses in all components	1.83 W

(Assuming: room temperature operation, 2.6 MHz motor excitation, compressor efficiency of 65%, and a smooth stator) Note: a slight excess of power remains at 200 m/s since the precise predicted crossing of the load and motor curves is at 205 m/s.

The planned operation consists of setting the various plenum pressures, then applying the excitation voltage to the motor electrodes in a step fashion, at a frequency slightly higher than the desired rotation frequency. The electrostatic torque induced will then spin up the disk until the load (compressor power and viscous dissipation) is equal to the electrical power delivered by the motor. Fig. 1.7 shows the motor electrical power curve and the load curves for the blower and bladeless rotor (assuming linearly varying mass flow with speed for the bladed disk and Couette flow for the bladeless rotor). The intersections of the motor and load curves are the predicted operating points.

### **1.3.3 Design Trade-Offs and Configuration Optimization**

Based on the experimental results from these devices as well as on progress in the component technologies, a final design for the second set of micro-compressor systems will be synthesized. Parametric studies of the motor-compressor performance have shown that a variety of configurations are viable. This section discusses the principal design trade-offs, and suggests configurations capable of delivering increased power and pressure rise.

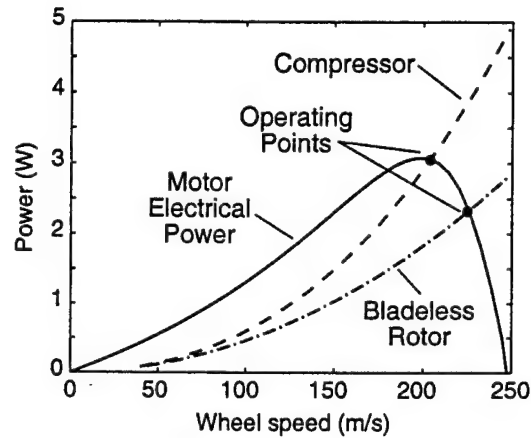


Fig. 1.7: Motor electrical power and load curves for the experimental devices.

The principal design parameters are disk radius, motor outer radius and rotational speed. For a large pressure rise, high wheel speeds are required since the work done by the compressor is proportional to the square of the wheel speed,  $(\Omega r)^2$ . The speed, however, is limited by structural considerations in the rotor, both out-of-plane deformation and maximum allowable stress. Both structural and turbomachinery fluid requirements therefore guide the choice of a wheel speed.

Rotational speed, disk radius, and motor outer radius are traded with several system considerations in mind, including motor electrical power, viscous drag in the motor gap and bearings, journal bearing stability, and fabrication constraints.

To realize an increased net power from the motor, the electrical power must be increased while limiting viscous drag in the motor gap:

- *Electrical power:* The machine area, geometry, applied voltage and frequency mainly set the achievable electrical torque. Voltage is limited by breakdown across the air gap and between electrodes. A minimum spacing and a maximum voltage are therefore imposed. Electrical frequency required is the product of the number of poles around the annulus and the rotational speed. Since the minimum electrode width and spacing is constrained by current fabrication capabilities, there is a maximum number of poles for a given inner motor radius. Given these voltage and geometric restrictions, the electrical power is proportional to rotational speed, through electrical frequency.
- *Viscous drag in the motor gap:* The viscous drag in the motor gap is related to the electrical power through geometry (inner radius, outer radius, and gap) and rotational speed. To first order, both scale with area and inversely to gap. The viscous dissipation however, varies as the square of the rotational speed while the electric power varies linearly with the speed. Net output power is therefore inversely proportional (to first order) to rotational speed.

Higher power motor-compressors capable of delivering higher pressure rise can be realized

by increasing the disk and motor radii and reducing the rotational speed (maintaining a high wheel rim speed). Output powers of more than 10 watts are possible for a 400m/s wheel speed and 4 mm radius configuration (double the nominal disk size of the current experimental devices). However, larger output power comes at the cost of other system issues and components:

- *In-plane rotordynamic stability* is conserved only if the journal bearing length-to-diameter ratio is kept constant. Doubling the rotor diameter requires doubling the journal length from 300 to 600 microns. This increases *fabrication difficulty*. Process development must be pursued to provide acceptable vertical walls at these depths with small gap widths.
- If the disk thickness is not increased proportionally to the radius, the out-of-plane *deflection of the disk* due to centrifugal loading will increase and may require backside geometric features (and thus increased fabrication complexity) to compensate.
- Larger rotor diameter configurations generate more electrical power but also incur high *viscous dissipation*. All the energy dissipated is transformed into heat, which must be transferred to the compressor flow path or to the surroundings. Packaging is complicated by heat dissipation issues.

Future motor-compressor configurations offering high power and pressure rise are possible but the above technical issues must be resolved in order to realize a practical micro-compression system. Less demanding requirements such as those for blowers for air sampling systems, allow the short-term development of a working, practical device.

## **1.4 Fabrication**

The micromotor-compressor will be fabricated using microfabrication technologies which are discussed in detail in the progress reports. This section will summarize the fabrication process flow and the new fabrication challenges introduced by the motor-compressor device.

### **1.4.1 Process Flow**

The fabrication process is an extension of the microturbine bearing rig process, i.e. a stack of five deep reactive ion etched silicon wafers, which are align bonded to form the device. Laser assisted etching will also be used to release the rotor after bonding. To the microturbine bearing rig fabrication process are added the steps required to build the electrical layers of the motor. Additional thick and thin film processing is done on the back of the rotor plate and the front of the aft end plate. Fabrication of the motor-compressor electrical layers will be done in coordination with the tethered-motor electrical fabrication which is intended to be identical for both devices. The process flow for the motor-compressor uses 18 masks and is illustrated in Fig. 1.8 (the thickness dimension is greatly exaggerated for clarity).

### Forward Foundation Plate

- 1) Deep etch Si through wafer (Mask A1)

### Forward End Plate

- 1) 1st and 2nd shallow etches for the FTB and tip clearance (Masks B1, B2)
- 2) Speed sensor thin films (SiO<sub>2</sub> and PolySi) (Mask B3)
- 3) 1st deep etch for plenums and nozzles (back side) (Mask B4)
- 4) 2nd deep etch (front side) (Mask B5)

### Rotor Plate

- 1) 1st and 2nd shallow etches, deposit thick SiO<sub>2</sub> (Masks C1, C2)
- 2) Deposit rotor conductor PolySi and pattern (Mask C3)
- 3) 1st deep etch for blades and plenums (Mask C4)
- 4) 2nd deep etch for journal bearing (Mask C5)

### Aft End Plate

- 1) Deposit thick SiO<sub>2</sub>
- 2) Deposit PolySi I and pattern interconnections rings (Mask D2)
- 3) Deposit thin SiO<sub>2</sub> film, CMP, and pattern the vias (Mask D3)
- 4) Deposit 1 micron PolySi II, pattern electrodes and leads, and CMP electrode surface (Mask D4)
- 5) Deep etch through SiO<sub>2</sub> and Si (100 microns total) (Mask D5)
- 6) Deep etch to connect with the front side (Mask D6)

### Aft Foundation Plate

- 1) Deep etches on both sides (Masks E1, E2)

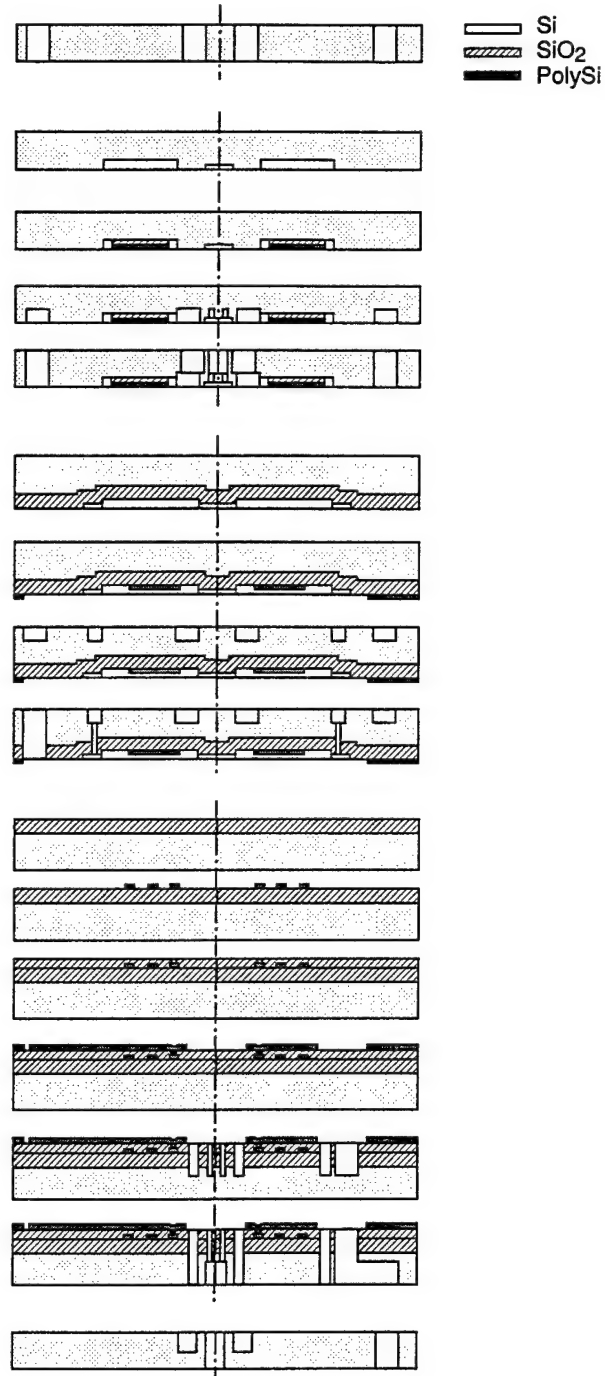


Fig. 1.8: Motor-compressor process flow. (Note: thickness is exaggerated for clarity.)

### 1.4.2 Fabrication Challenges

The fabrication of the electrostatic induction motor and the integration into the micro-compression system requires several fabrication techniques not yet demonstrated in power MEMS. The process development is ongoing for most of these steps and will continue as the motor-

compressor and tethered-motor are fabricated. The processes which need to be developed include:

- Thick film characterization ( $\text{SiO}_2$  10-20 microns):
  - Deposition
  - Etching
  - Bonding
- Thin film characterization (PolySi 0.5-2 microns,  $\text{SiO}_2$  1 micron)
  - Rotor conductor material
  - Electrodes and interconnects
- Chemical-mechanical polishing for the planarization of wafer surface (1-10 micron  $\text{SiO}_2$  topology)
- Deep reactive ion etching through thin films, thick films, and the underlying substrate
- Aligned wafer level bonding for wafer with thin and thick films
  - Surface reaction
  - Wafer curvature (due to film residual stress)

The challenge consists in evolving these processes in a timely fashion to levels acceptable for proper device operation.

## 2.0 ELECTROMECHANICAL ENERGY CONVERSION

### 2.1 Introduction

We continue to study electromechanical energy conversion as it is effected through the subsystem shown in Fig. 2.1. This subsystem comprises three primary components: an electromagnetic machine, its power electronics and its controller. The subsystem can convert energy in either direction. To convert mechanical energy to electrical energy, the electromagnetic machine is excited as a generator by a mechanical source and energy flows from left to right with the electrical load. To convert electrical energy to mechanical energy, the electromagnetic machine is excited as a motor by an electrical source, and energy flows from right to left into the mechanical load.

In general, the electromagnetic machine in Fig. 2.1 can be either electric or magnetic in character. Nearly all macro-scale electromagnetic machines in operation today are magnetic because the achievable power density of macro-scale magnetic machines greatly exceeds that of macro-scale electric machines. At the micro scale, however, the achievable power densities are more comparable. Given this, we have chosen an electric machine as our energy converter because the materials from which it can be fabricated are more compatible with microfabrication, and with high-temperature, high-speed and high-frequency operation, when compared to the materials from which a magnetic machine can be fabricated.

While there are many electric machines from which to choose, only two electric machines need be considered here from a practical viewpoint: the induction and variable-capacitance machines. Having analyzed both, we believe that the induction machine is simpler to fabricate, and that it will perform better than the variable-capacitance machine from an electromechanical viewpoint. Thus, for our purposes, the machine in Fig. 2.1 is an electric induction machine.

The electric induction machine employed here is shown in Figs. 2.2, 2.3 and 2.4. On one side of its air gap, stator electrodes are supported by an insulator deposited on a conducting

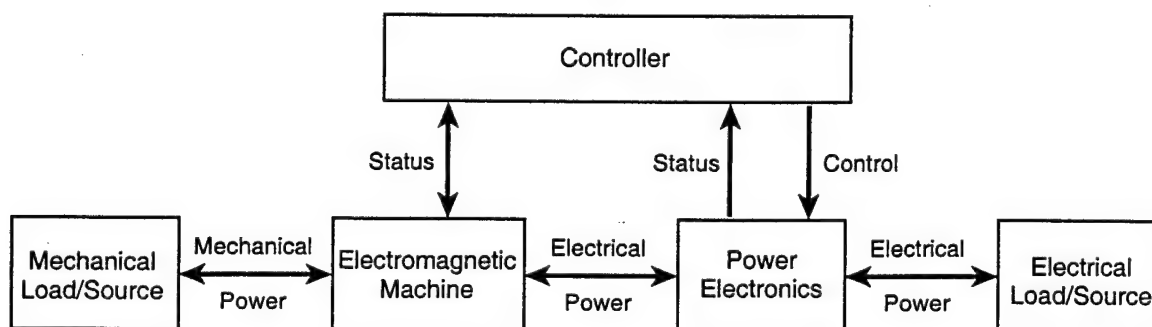


Fig. 2.1: Electromechanical energy conversion subsystem.

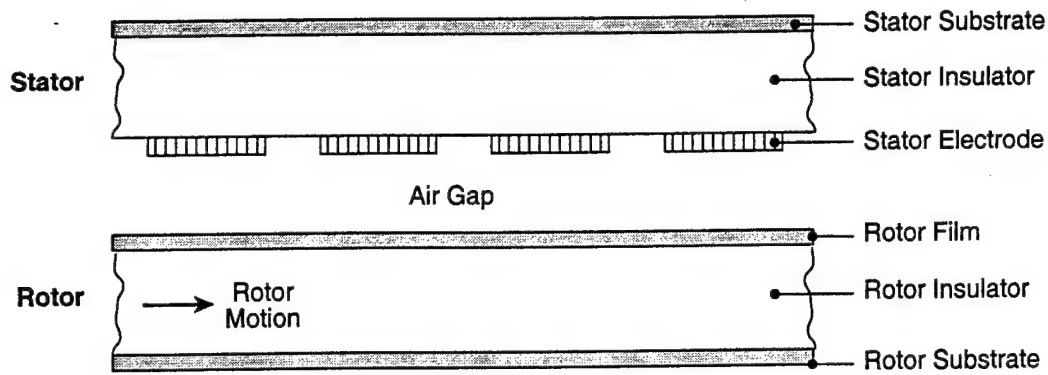


Fig. 2.2: Side view of the micro-scale electric induction machine; not drawn to scale.

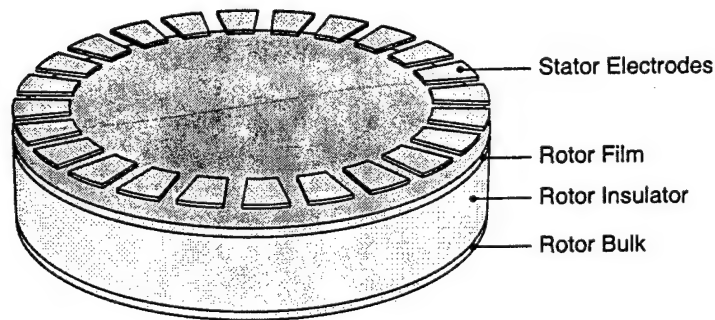


Fig. 2.3: Perspective view of the micro-scale electric induction machine; the stator insulator and substrate are not shown.

substrate. The electrodes can be connected to form one or more phases, and are used to impose a potential wave which travels around the stator. On the other side of the air gap is the rotor, which rotates as a disk. The rotor consists of a weakly conducting film supported by an insulator deposited on a conducting substrate.

During motoring operation, the power electronics excite the stator electrodes to produce a potential wave which travels around the stator with a speed exceeding that of the rotor. This wave, through the corresponding charges which reside on the stator electrodes, induces image charges on the rotor film. Since the speed of the traveling potential wave exceeds the mechanical speed of the rotor, rotor motion alone can not synchronize the rotor charges with the traveling wave, as must happen in steady state. Thus, the rotor charges must conduct through the rotor film to maintain synchronism. The conduction process must in turn be driven by a tangential electric field, and so the rotor charges lag behind the potential wave to produce that field, as shown in Fig. 2.4. Finally, the tangential electric field acts on the rotor charges to impart a tangential surface stress on the rotor, which in turn results in a motoring torque. During generating operation, the rotor speed exceeds that of the traveling potential wave, and the process is reversed.



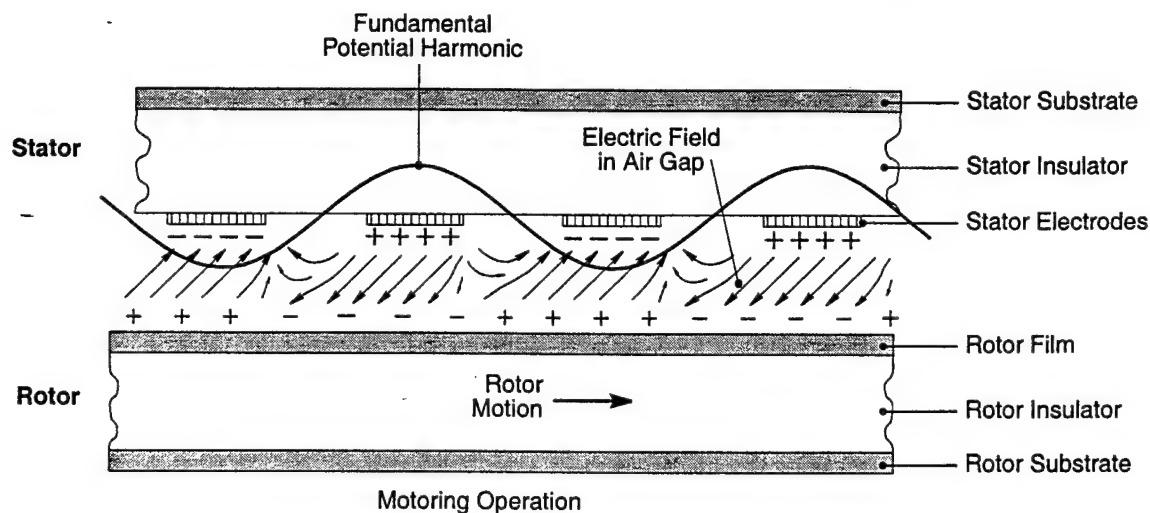


Fig. 2.4: Electric charges and fields within an electric induction motor.

To develop the electric induction machine, and the complete electromechanical subsystem of Fig. 2.1, we have focused our efforts on several topics over the past year. First, we have continued to refine our models for the electric induction machine, and the electromechanical subsystem in total. Second, we have initiated experiments to study several important physical phenomena, specifically rotor film conductivity, thick insulator deposition, and electrical breakdown between stator electrodes. Third, we have completed the design of a micro-scale tethered motor and a micro-scale motor-compressor, and will begin their fabrication soon. Fourth, we have outlined several candidate power electronic configurations and controllers for those motors, and have begun their development. Fifth, we have completed a study of whether electrostatic bearings can improve the stability of the gas journal bearings which support the rotor of the electric machine and its host microturbo-machinery. Finally, we have continued to study an experimental macro-scale induction generator. Our progress on each of these topics is discussed below.

## 2.2 Modeling

Our modeling focuses on the electric induction machine shown in Figs. 2.2 and 2.3. To simplify this modeling, the machine geometry is first unwrapped to become linear and then extended laterally to become two-dimensional. To accommodate the actual geometry of the machine, the resulting models are ultimately truncated and then wrapped back into a disk shape. We have developed geometric constraints to determine when this process is valid, and in all cases of interest it appears to be. In total, four models have been developed to date for the electric induction machine shown in Figs. 2.2, 2.3 and 2.4. These models are summarized below, and the first three are presented in more detail in Appendix A.

The first model is a two-dimensional representation and assumes that the stator electrodes

are excited in temporal sinusoidal steady-state, and that their geometry excites only a single spatial harmonic of electric potential around the stator. It also assumes that the rotor rotates with a constant velocity. Under these assumptions, Maxwell's equations are solved for the electric potential, field and charge within the machine. These 2-D results are then transformed to 3-D results in the second model and used to compute machine torque, electrical and mechanical power, and efficiency as functions of the geometry, material properties, speed and electrical excitation of the machine. This model is used for examining global performance trends and for making major design decisions.

The third model takes into account the discrete geometry of the stator electrodes, and the fact that they produce many spatial harmonics of electric potential around the stator. This model is constructed as a Fourier superposition of the second model evaluated over the relevant spatial harmonics. As with the first and second models, the third model computes machine torque, electrical and mechanical power, and efficiency as functions of the geometry, material properties, speed and electrical excitation of the machine. This model is used for making detailed design decisions.

The fourth model is a transient model which relaxes the assumption of a temporal sinusoidal-steady-state excitation of the stator electrodes. It is essentially a Fourier superposition of the third model over the temporal harmonics within the stator excitation, although it is not expressed in this manner. Rather, it is expressed in state-space form so that it may be coupled to a state-space model of the power electronics and controller in Fig. 2.1. It is used to perform detailed steady-state and transient electrical simulations of the entire electromechanical subsystem operating at a constant, or relatively slowly varying, speed.

## **2.3 Physical Phenomena**

There are several physical phenomena which are important to the design and performance of our micro-scale electric induction machine, and fabrication dependent. These phenomena include the conductivity of the rotor film, the maximum achievable thickness of the rotor and stator insulators, and electrical breakdown between the stator electrodes. Because they are fabrication dependent, we have undertaken experimental studies of these phenomena, as described below.

### **2.3.1 Rotor Conductivity**

For an electric induction machine to operate as designed, its rotor film conductivity must fall within a relatively narrow range of its design value. If the conductivity is too low, then little rotor charge and torque develops. If the conductivity is too high, then little tangential electric field is required to drive charge conduction through the rotor film, and again little torque develops.

Thus, for a given rotor speed and electrical excitation frequency, there is an optimal rotor film conductivity, and it is desirable to fabricate a rotor film having this conductivity; see Appendix A and Fig. 2.7 in [1] for an example of this. In addition, if the conductivity varies with the temperature of the rotor film, then it may be desirable to design a controller that tracks conductivity and adjusts the electrical excitation frequency of the machine. This would minimize the reduction of torque caused by conductivity variations. However, to do so it is desirable to know the variability of the rotor film conductivity with temperature. In summary, rotor film conductivity is a material property which must be well characterized, and then controlled during fabrication.

In general, it is desirable for the electromechanical subsystem to operate over a wide temperature range. Therefore, selecting a material for the rotor film is problematic because the conductivity of most materials varies significantly with temperature. However, if the temperature range is limited then material selection becomes easier. As a starting point, we assume that the operating temperature of the electric machine will remain below 200°C. This permits the use of doped polysilicon for the rotor film, and is appropriate for the stand-alone tethered motor, motor-compressor and turbine-generator described in Sections 2.4 and 2.5. In the future, we will develop conductors capable of higher-temperature operation suitable for use in the gas turbine generator.

To gain adequate control over the conductivity of the rotor film during fabrication, we have initiated experiments to measure the conductivity of doped polysilicon with a structure similar to that of the electric induction machine. The experimental structure is shown in Fig. 2.5. The structure consists of two interdigitated electrodes, on top of a thin layer of silicon dioxide, on top of a thin layer of doped polysilicon, on top of a thick layer of silicon dioxide, on top of a conducting substrate. This structure is identical to that of the electric induction machine, except that the gap is replaced by a thin layer of silicon dioxide. Further, it provides an indirect contactless measurement

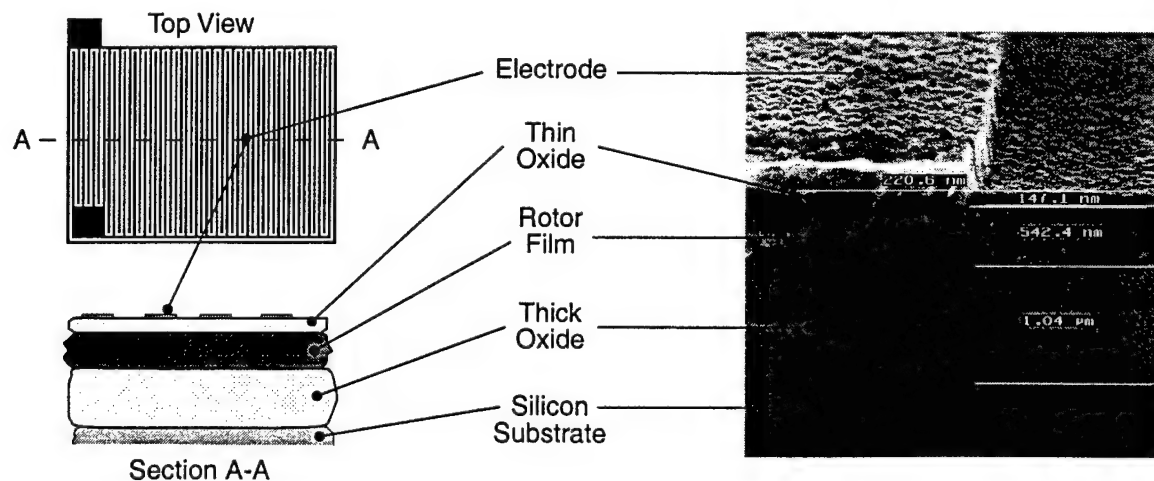


Fig. 2.5: The polysilicon, rotor film, conductivity test structure.

of conductivity which eliminates errors caused by charge injection at the metal-silicon interface formed with a contacting probe.

Devices having the structure shown in Fig. 2.5 have been fabricated over a wide range of polysilicon doping. These devices have also been subjected to varying high-temperature anneals to simulate subsequent motor fabrication steps. To determine the conductivity of the polysilicon as a function of doping and annealing, the admittance of each device is measured as a function of frequency. The admittance measurements are then fit to a model, and the conductivity for the corresponding doping is extracted from the model parameters. To date, we have measured conductivity only at room temperature, but we will extend these experiments to higher temperatures shortly.

We have fabricated structures doped with either phosphorus or boron impurities. Our experiments with phosphorous-doped structures showed that phosphorous doping cannot be used to obtain the desired rotor film conductivity. This is most likely the result of phosphorous segregation to the polysilicon grain boundaries [8], which occurs at low dopant concentrations. Boron, on the other hand, does not segregate to the grain boundaries. Our experiments with boron-doped structures have been more successful. The results presented below are all obtained from these structures.

Figures 2.6 and 2.7 show results which are typical of the rotor film conductivity experiments. These experiments have shown that rotor film conductivity increases with both boron implant concentration and the number of high temperature anneals beyond implant activation.

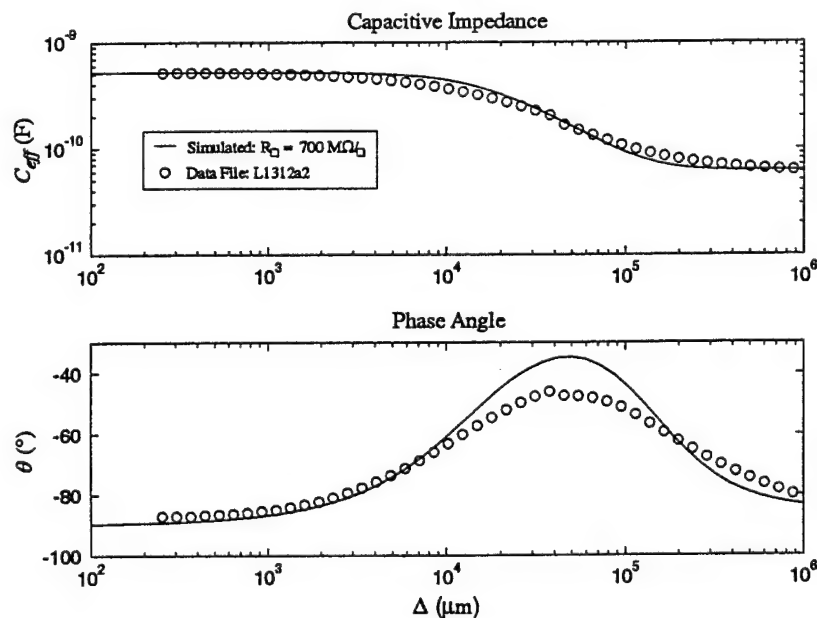


Fig. 2.6: Magnitude and phase of the capacitive admittance from a rotor film conductivity experiment.

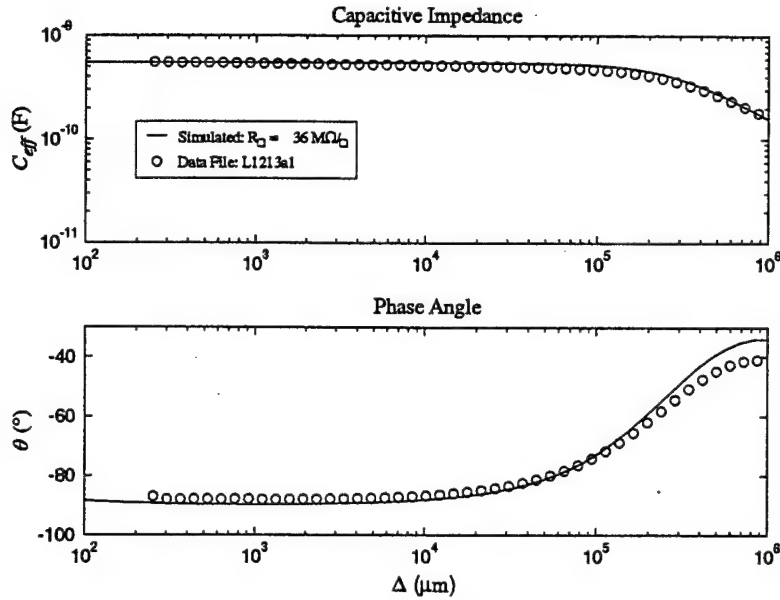


Fig. 2.7: Magnitude and phase of the capacitive admittance from a rotor film conductivity experiment.

Phase peaks at higher frequencies are indicative of a higher rotor film conductivity. Figure 2.6 corresponds to a high boron implant doping density of  $2 \times 10^{13} \text{ cm}^{-2}$  with only a single anneal beyond implant activation, and thus explores the upper bound of conductivity when only one anneal is permitted after activation. Figure 2.7 corresponds to a low implant doping density of  $3 \times 10^{12} \text{ cm}^{-2}$  with a double anneal beyond implant activation, and thus explores the lower bound of conductivity when two or more anneals are required during fabrication after activation. Both figures show a measured and modeled admittance as a function of frequency; note that the magnitude of each admittance is divided by frequency, and is thus presented as a capacitance. Each modeled admittance has a rotor film conductivity chosen to make a best-fit match to the measured admittance:  $5.5 \times 10^{-4} \text{ S/cm}$  in the case of Fig. 2.6 and  $7.9 \times 10^{-5} \text{ S/cm}$  in the case of Fig. 2.7. In general, the match between measured and modeled admittances is quite good, and demonstrates that the devices are working properly. Most importantly, the conductivities extracted from the admittances bracket that which is needed for our micro-scale electric induction machines, on the order of  $1 \times 10^{-4} \text{ S/cm}$  for a  $0.5 \text{ μm}$ -thick rotor film, demonstrating that we can fabricate the required film. While more experiments are necessary to establish repeatability over the required narrow range of conductivity, this is a significant result. We expect to complete the experiments, including temperature variations, during Fall 1998 in preparation for micro-scale motor fabrication.

### 2.3.2 Insulator Deposition

From an electromechanics viewpoint, it is undesirable for the stator electrodes and conducting rotor film to operate in the vicinity of relatively conducting substrates. Yet, due to the

manner in which the electric machine is fabricated within its host turbomachinery, such operation is inevitable. For its part, the conducting stator substrate increases the parasitic stator capacitance which ultimately reduces machine efficiency and makes the power electronics more difficult to implement. Similarly, the conducting rotor substrate acts to short out the rotor film thereby limiting machine performance. Consequently, it is desirable to remove the conducting substrates from the vicinity of the air gap. This is the role of the stator and rotor insulators.

To determine the maximum achievable insulator thickness, we have undertaken an experimental study of the plasma-enhanced chemical-vapor deposition of very thick films of silicon dioxide. The results of this study indicate that it is possible to deposit such films up to 10  $\mu\text{m}$  in thickness before they crack due to internal stress. This is adequate for our electric induction machines; even a large increase beyond this thickness is calculated to yield only a modest performance improvement of about 15%. By way of illustration, Fig. 2.8 shows the predicted output torque of the tethered motor discussed in Section 2.4 as a function of the rotor insulator thickness. At present, the design of this machine employs a 10- $\mu\text{m}$ -thick rotor insulator.

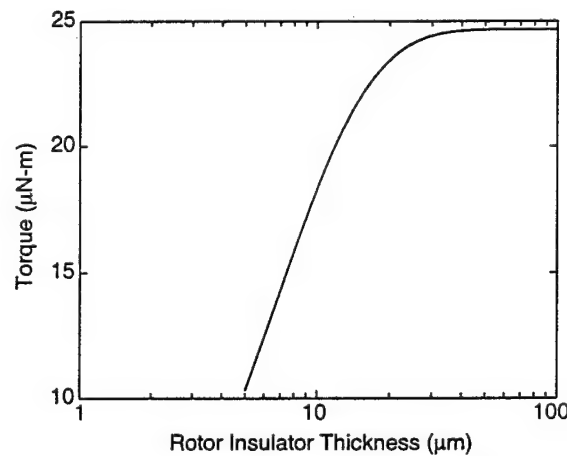


Fig. 2.8: Predicted output torque of the tethered motor discussed in Section 2.4 as a function of its rotor insulator thickness.

### 2.3.3 *Electrical Breakdown*

Electrical breakdown between the stator electrodes will limit the voltage which may be applied between them, and hence will limit the torque and power of the electric induction machine. In micromechanical devices, it has already been shown that voltages of 300 V and electric fields of  $10^8$  V/m may be applied across the micron-scale gaps between the electrodes of our machines, and similarly across the rotor-stator gap without breakdown [3, 4]. However, previous experience at these dimensions was at frequencies much lower than those planned for our machines, and with different electrode geometries. Therefore, to determine the limit for our machines, we have begun

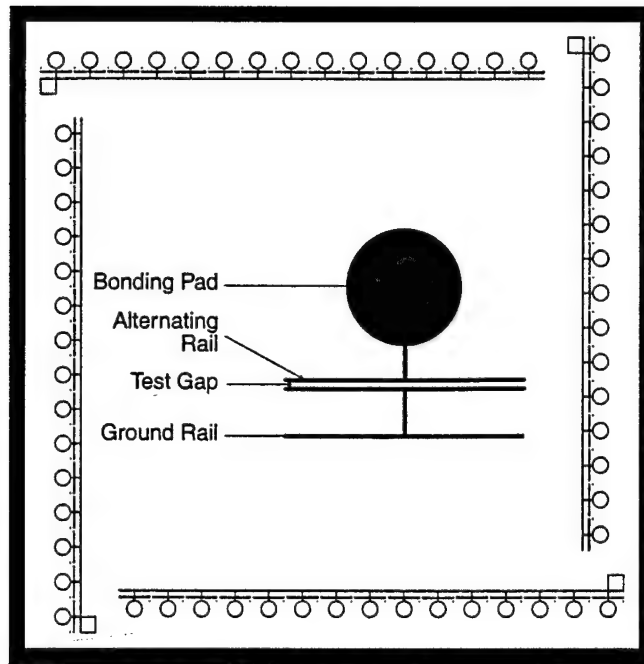


Fig. 2.9: Top view of the electrical breakdown experiment. An expanded view of one test gap is shown in the center of the figure.

an experimental study of electrical breakdown.

The experiment consists of die containing 60 individual electrode pairs which may be individually tested. Electrode pairs having gap lengths of 2, 3, 4, 5 and 10 microns are included in equal number on each die. The configuration of a die is shown in Fig. 2.9, together with a magnified view of one test gap. The gaps have been tested at 300 V dc and withstand that excitation indefinitely. Testing of the 4 micron gaps at 3 MHz shows that they can withstand a 300 V peak excitation indefinitely, with the actual test times being up to a few hours. However, these gaps break down almost immediately when excited with peak voltages on the order of 325 V to 350 V. 3 MHz testing of the 2 micron gaps shows that they break down with excitations on the order of 220 V peak, while the 3 micron gaps break down with excitations on the order of 250 V peak.

## 2.4 Tethered Motor

Our first functional electric induction machine will be a tethered motor. A tethered motor is one in which the rotor is suspended within the stator by flexible mechanical tethers. The torque produced by such a motor is directly measurable through the bending of its tethers, which is easily calibrated using independent test structures. Because the rotor is tethered, and hence stationary, the torque measurements are not obscured by bearing behavior, and are expected to be very accurate. Thus, a major objective of the tethered motor is to accurately measure the torque produced by a



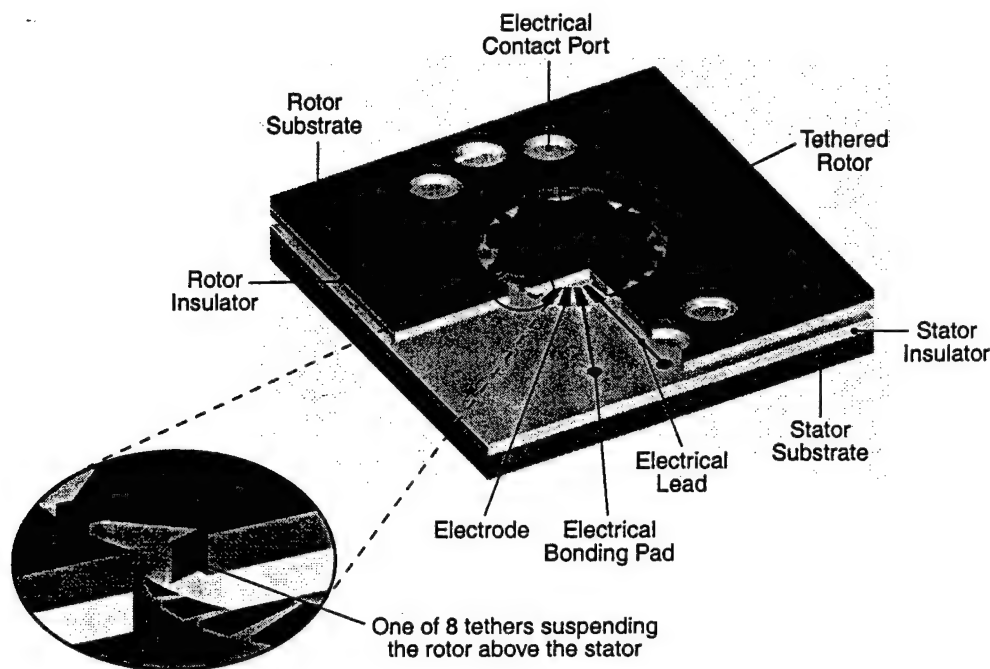


Fig. 2.10: Micro-scale tethered electric induction motor.

micro-scale electric induction motor, and to experimentally validate the models described above. Additionally, since the tethered motor has no bearings, it is simpler to fabricate than a rotating motor and is therefore also ideal for studying the microfabrication of an electric induction machine.

Our tethered motor is shown in Fig. 2.10; note that in this figure the stator is on the bottom and the rotor is on the top. The active portion of the motor has a 4-mm outside diameter and a 2-mm inside diameter. Its stator carries 786 electrodes connected in 6 phases; 6 phases were chosen to reduce the voltage between neighboring electrodes, and hence reduce the effects of electrical breakdown. Its rotor is supported by 8 tethers having aspect ratios of 50:1, and carries a 0.5- $\mu\text{m}$ -thick doped polysilicon film on a 10- $\mu\text{m}$ -thick silicon dioxide insulator. The gap between the stator and rotor is 3  $\mu\text{m}$ . This design is electrically identical to the motor-compressor described in Section 2.5.

The predicted torque of the tethered electric induction motor is shown in Fig. 2.11 as a function of its electrical excitation frequency and air gap separation, assuming that the amplitude of that excitation is 300 V. At peak torque, we expect the rotor to rotate approximately  $1.5^\circ$  against its tethers. To measure this rotation, the rotor has a grating etched into its top surface which can be used to create Moire patterns sensitive to well within  $0.1^\circ$  of rotation [6, 7]. With the same excitation, the tethers should be sufficiently stiff so that the vertical deflection of the rotor is less than 0.5  $\mu\text{m}$ ; the expected vertical force on the rotor is shown in Fig. 2.12 as a function of electrical excitation frequency and air gap separation, given a stator electrode excitation amplitude of 300 V.

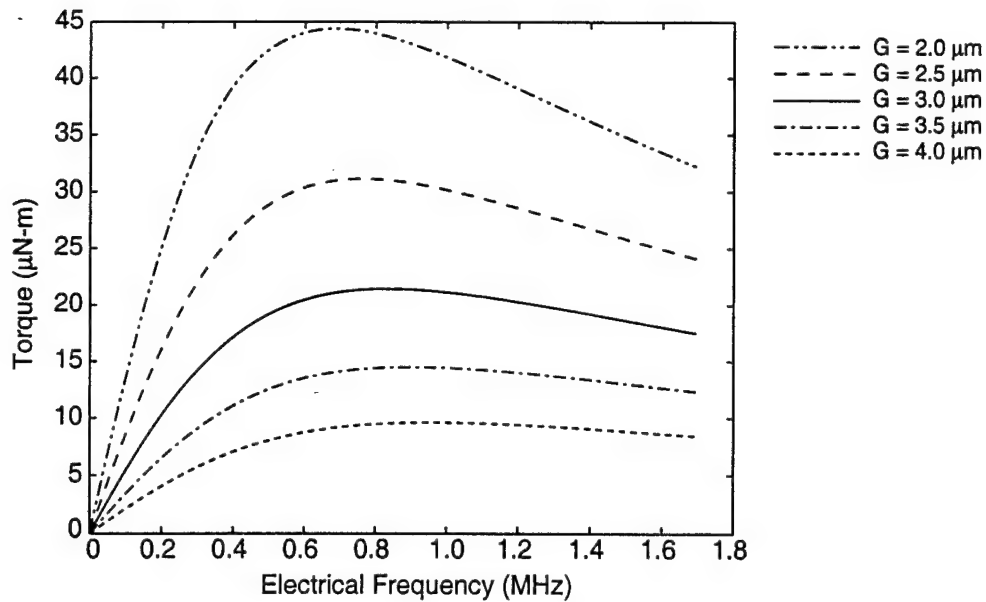


Fig. 2.11 Predicted rotor torque of the tethered electric induction motor for various gap spacings,  $G$ , as a function of the electrical excitation frequency.

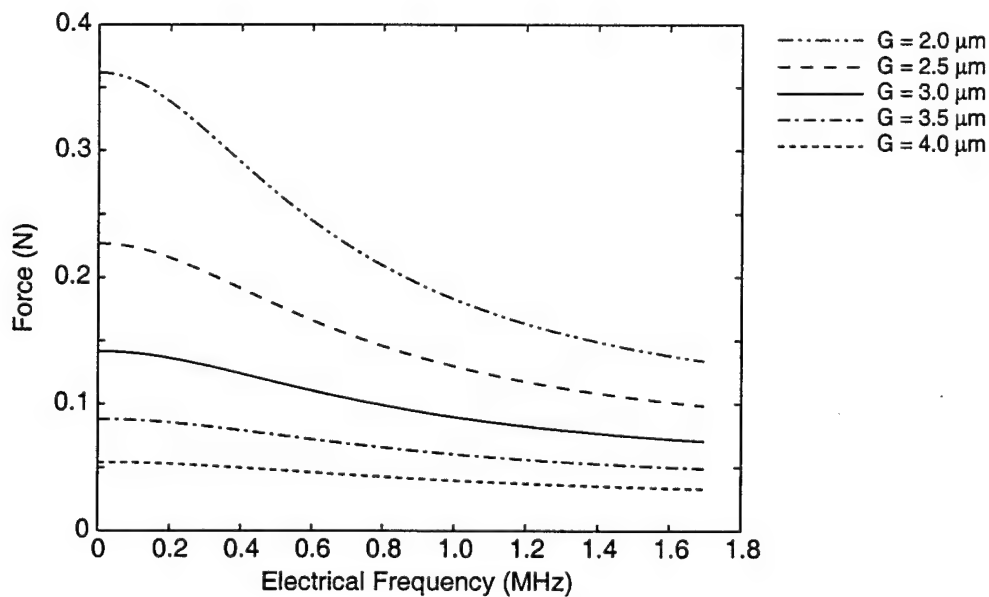


Fig. 2.12 Predicted rotor pull-in force of the tethered electric induction motor for various air gap spacings,  $G$ , as a function of the electrical excitation frequency.

## 2.5 Power Electronics

The purpose of the power electronics in Fig. 2.1 is to excite the stator electrodes of the electric machine with sinusoidal or square-wave voltages of equal amplitude and proper phase so as to create a traveling potential wave around the stator in the direction of rotor rotation. If the

speed of this wave exceeds that of the rotor, then the machine acts as a motor. If the speed of the rotor exceeds that of the wave, then the machine acts as a generator. Thus, the magnitude and sign of the power produced by the electric machine is governed by the speed and amplitude of the traveling wave, which are ultimately set by the controller in Fig. 2.1 in response to an operational objective.

Recently, we have focused on developing power electronics for the tethered motor and motor-compressor. Both motors will require stator excitations having amplitudes up to 300 V and frequencies up to 5 MHz. Under these conditions, it is difficult to operate small transistors efficiently, particularly since the parasitic capacitance associated with the stator electrodes draws added reactive power from the power electronics. Because of this, we will employ resonant power electronics to boost the output voltage.

The output stage of one phase of the power electronics is shown in Fig. 2.13. It consists of two transistors in a bipolar push-pull configuration followed by an inductor which connects to the electrodes of one phase. For the purposes of discussion here, that phase of the electric machine is modeled, when looking into the electrodes, as an equivalent series capacitor and resistor. During operation, the transistor pair is used to present an alternating voltage to the inductor, and this voltage drives the resonant circuit formed by the inductor and electrode capacitance to boost the voltage at the electrodes. In this way, the power electronics can be constructed from simple low-voltage components. Further, simple control electronics may be employed to regulate the output amplitude and frequency of the electrode voltage, and the relative phase shift of each motor phase.

The real power absorbed by the electric machine, and losses in the inductor, limit the output voltage and frequency range over which the power electronics can operate. To explore these limits, we have constructed and tested the power electronics for one phase from readily available components. Based on the success of these tests, we have designed, constructed, and tested a complete 6-phase resonant power electronics. By varying the values of its resonant

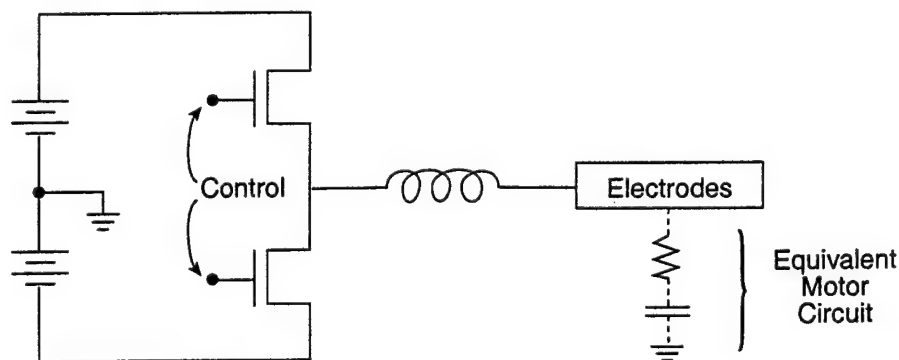


Fig. 2.13: One phase of the resonant power electronics.

inductors, this electronics can drive the tethered motor and motor-compressor at frequencies up to 3 MHz and voltages up to 300 V peak.

## 2.6 Electric Bearings

- In response to concerns about the stability of the gas bearings, we have undertaken and completed a study of electric bearings. The goal of the study was to determine whether electric bearings, operating in parallel with the gas bearings, could be used to enhance the stability of the gas bearings. The results of the study are reported in detail elsewhere [5], and are summarized here.

The essential features of a gas/electric journal bearing are shown in Fig. 2.14. The figure shows a rotor rotating within a housing. The center of the rotor is offset from the center of the housing in the transverse direction. To keep the rotor adequately centered within the housing, the gap between the rotor and housing is filled with a gas to form a gas journal bearing. In parallel with the gas bearing, an electric bearing is formed by lining the inner surface of the housing with three or more electrodes. One electrode is grounded, while the others are driven by voltage sources to produce an electric field across the gap which terminates on the rotor. The field in turn produces a transverse force on the rotor. By adjusting the voltage sources, the direction and magnitude of the electric force can be dynamically adjusted within the limits of electrical breakdown to provide bearing stiffness, damping, or both.

To study the capabilities of the electric bearing, we developed a dynamic model for the lateral deflections of the rotor. This model combined the fluid dynamics of the gas bearing with the electromechanical dynamics of the electric bearing. Next, an equilibrium state for the rotor

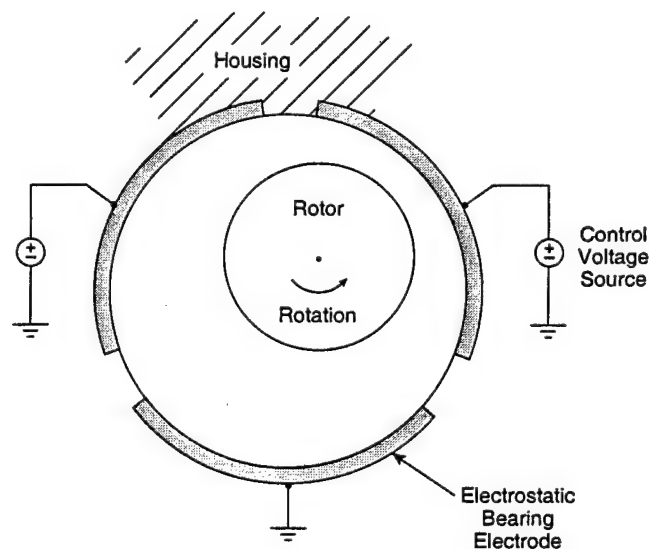


Fig. 2.14 Cross section of a gas/electric journal bearing; note that the bearing gap is exaggerated.

was defined, and a controller was designed for the electric bearing so as to maintain the desired equilibrium. Simulations of the gas/electric bearing were then used to evaluate the capabilities of the electric bearing and the combined gas/electric bearing.

From the simulations, it appears that the electric bearing can stabilize the otherwise unstable gas bearing up to eccentricities of approximately 0.2. However, the stabilized equilibrium must be static, and the electric bearings cannot provide any significant shock absorption. The electric bearings cannot stabilize the gas bearing at larger eccentricities, or when the equilibrium rotor state involves significant whirl. The primary reason for this limited capability is that both the magnitude and direction of the electric force are significantly limited by electric breakdown above even moderate eccentricities.

## **2.7 Macro-Scale Electric Induction Generator**

During the past year we constructed and began to test the macro-scale electric induction generator shown in Fig. 2.15. The purpose of this generator was to support the study of self-excited generation and the development of power electronics and controllers for micro-scale machines. This generator also became a test-bed for our modeling, and in so doing it pointed out critical issues which must be considered during the design and operation of micro-scale electric induction machines.

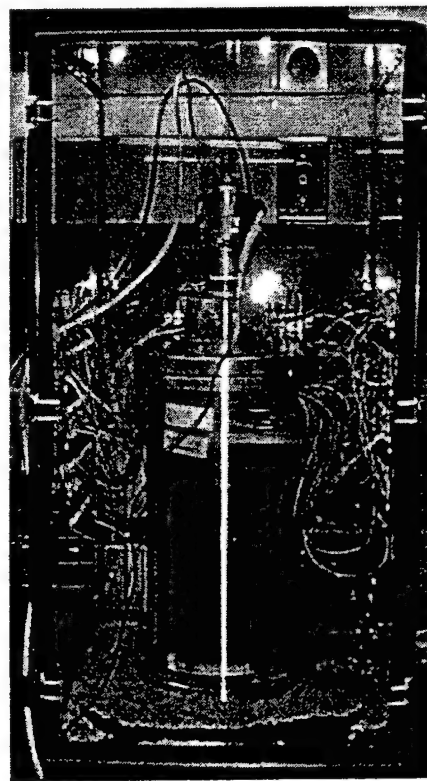


Fig. 2.15: The experimental macro-scale electric induction generator.

In comparison to the polysilicon doping to be employed for the micro-scale machines, the process for obtaining an appropriate rotor film conductivity for the macro-scale generator was somewhat less precise; a coating of anti-static spray was applied to the rotor, which was machined from a cylinder of G-10 fiberglass/epoxy composite. The resulting conductivity was difficult to predict and control, and it varied significantly with the ambient humidity. Since the rotor film conductivity must be maintained within a relatively narrow range to permit self excitation, this posed a significant problem with respect to operating the macro-scale generator.

Initial experiments with the macro-scale generator, and subsequent analysis, also demonstrated that parasitic capacitance associated with its stator electrodes significantly masked its effective rotor impedance as seen from its stator terminals. This limited the power which the generator could supply for a given terminal voltage. As a result, our analysis indicated that it was necessary to use a very-low-loss inductor to achieve self-excitation. Such inductors are not readily available. This experience emphasized the significance of parasitic capacitance, which is to a great extent unavoidable in machines of this type, and caused us to re-evaluate our approach to the development of power electronics for micro-scale electric induction machines.

In summary, self-excitation of the macro-scale generator has not yet been demonstrated. Given the difficulties involved in controlling its rotor film conductivity and finding very-low-loss inductors, we have decided to set aside the macro-scale generator for the time being and concentrate our experimental efforts on micro-scale machines. This decision appears justifiable in view of the impending availability of the micro-scale machines, and the fact that we have gained considerable knowledge from our experimental work on the macro-scale generator.

### 3.0 SUMMARY AND PLANS

All of the elements (fluid mechanics, structures, bearings and rotordynamics, electromechanics, circuit design) needed to realize the design of micromotor compressors have been put in place. This effort has culminated in the design of several micro devices, and the development of the microfabrication technology needed to realize these devices has been started.

The microblower/compressor designs are summarized in Tables 3.1-3.3. Design data are presented for the Level 0 test devices (for which construction has started), Level 1 blowers (the first self-contained units), and Level 2 blowers (the second iteration on level 1 and the first units packaged for users). Note that not all of the information is present since not all of it is currently known. Also, except for the Level 0 devices, the details represent plans only and therefore are subject to change. Table 3.1 presents the information of primary interest to users, including airflow and pressure rise, power consumption, heat dissipation, and size. Table 3.2 gives the overall design and performance levels, showing the power and loss breakdowns. Table 3.3 details the subcomponent design parameters, especially those of the motor.

This work is continuing under a follow-on ARO/DARPA grant. Plans call for the fabrication and testing of the Level 0 devices in 1998. the Level 2 devices will be completed before the end of 1999.

**Table 3.1: Micromotor Blower/Compressor External Description**

User Characteristics	Level 0 Test Device	Level 1 Breadboard Blower	Level 2 Packaged Blower	Nominal MicroCompressor
Airflow	0.05 g/s	0.11 g/s	0.11 g/s	0.11 g/s
Pressure rise	1.02:1 (8 in of H <sub>2</sub> O)	1.06:1 (24" of H <sub>2</sub> O)	1.06:1 (24" of H <sub>2</sub> O)	1.76:1 (309" H <sub>2</sub> O)
Electric power required	8.0 W	26.6 W	14.7 W	107 W
External bearing air required	Yes	No	No	No
Device dimensions	15x15x2.5 mm	19x19x1.5mm	19x19x1.5mm	19x19x3.0mm
Electronics dimensions	250x250x100 mm	250x250x100 mm	20x20x10 mm	20x20x10 mm
Device heat dissipation	5.6 W	16.4 W	8.1 W	65.5 W
Electronics heat dissipation	2.0 W	8.0 W	4.4 W	32.2 W

**Table 3.2: Design and Performance**

Design Characteristics	Level 0 Test Device	Level 1 Breadboard Blower	Level 2 Packaged Blower	Nominal MicroCompressor
Airflow	0.05 g/s	0.11 g/s	0.11 g/s	0.11 g/s
Pressure rise	1.02:1 (8" of H <sub>2</sub> O)	1.06:1 (24" of H <sub>2</sub> O)	1.06:1 (24" of H <sub>2</sub> O)	1.76:1 (309" H <sub>2</sub> O)
Rotor diameter	4 mm	8 mm	8 mm	8 mm
Blade height	0.2 mm	0.2 mm	0.2 mm	0.1 mm
Rotational speed	193 m/s	200 m/s	200 m/s	400 m/s
Electric power in	8.0 W	26.6 W	14.7 W	107.3 W
Electrical losses – device	3.9 W	11.6 W	3.3 W	24.0 W
Electrical losses – electronics	2.0 W	8.0 W	4.4 W	32.2 W
Fluid viscous losses	1.7 W	4.8 W	4.8 W	41.4 W
Net mechanical power available	0.7 W	2.2 W	2.2W	9.7 W
Net mechanical power delivered	0.1 W	1.3 W	1.3 W	5.5 W
Overall device efficiency	1.1 %	5.0 %	9.1 %	5.1 %

**Table 3.3: Device Design Details**

Major assumptions	Level 0 Test Device	Level 1 Breadboard Blower	Level 2 Packaged Blower	Nominal MicroCompressor
Operating temperature	273 K	298 K	298 K	298 K
Number of motors	1	1	1	2
Peak voltage	300 V	300V	300V	300V
Electrical frequency	2.6 MHz	1.8 MHz	1.8 MHz	5.8 MHz
Number of electrical poles	131	175	175	306
Number of phases per pole	6	6	6	6
Motor air gap	3 microns	3 microns	3 microns	2.5 microns
Rotor insulator thickness	10 microns	20 microns	20 microns	20 microns
Motor inner radius	1 mm	1 mm	1 mm	1.75 mm
Motor outer radius	1.9 mm	3.5 mm	3.5 mm	3.5 mm
Inter-electrode gap	4 $\mu$ m	4 $\mu$ m	4 $\mu$ m	4 $\mu$ m
Minimum electrode width	4 $\mu$ m	2 $\mu$ m	2 $\mu$ m	2 $\mu$ m
Compressor bleed air	5 % of main air	5 % of main air	5 % of main air	5 % of main air
Compressor efficiency	25%	25%	25%	60%
Journal bearing eccentricity	80%	80%	80%	80%



#### 4.0 REFERENCES

1. Epstein, A.H. *et al.*, "Micro Gas Turbine Generators", Interim Technical Progress Reports for Grant DAAH04-95-1-0093, Submitted to the US Army Research Office, January 1996, January 1997.
2. Piekos, E.S., Orr, D.J., Jacobson, S.A., Ehrich, F.F., Breuer, K.S., "Design and Analysis of Microfabricated High Speed Gas Journal Bearings," AIAA Paper AIAA 97-1666, presented at 28<sup>th</sup> AIAA Fluid Dynamics Conference & 4<sup>th</sup> Shear Flow Control Conference, Snowmass Village, CO, June 1997.
3. Bart, S.F., Lober, T.A., Howe, R.T., Lang, J.H. and Schlecht, M.F., "Design Considerations for Micromachined Electric Actuators", *Sensors & Actuators*, Vol. 14, pp. 269-292, 1988.
4. Bart, S.F., Mehregany, M., Tavrow, L.S., Lang, J.H. and Senturia, S.D., "Electric Micromotor Dynamics", *IEEE Transactions on Electron Devices*, Vol. 39, pp. 566-575, March 1992.
5. Mur-Miranda, O., "Feasibility of Electrostatic Bearings for Micro Turbomachinery", M. Eng. Thesis, EECS Department, MIT, Cambridge, MA, December 1997.
6. Malacara-Doblado, D., "Measuring the Curvature of Spherical Wavefronts with Talbot interferometry," *Optical Engineering*, Vol. 36, No. 7, pp. 2016-24, 1997.
7. Tran, A.T.T.D., Lee, J.J., Zhang, K., Lo, Y.-H., "Ultrafine Motion Detection of Micromechanical Structures using Optical Moire Patterns," *IEEE Photonics Technology Letters*, Vol. 8, No. 8, pp. 1058-60, 1996.
8. Karmins, T., *Polycrystalline Silicon for Integrated Circuit Applications*, Kluwer Academic Publishers, Boston, 1988.

## APPENDIX A - ELECTROMECHANICAL MODELING

### A.1 Introduction

The Tethered Motor and the Motor-Compressor host identical micro-scale electric induction machines. Figure A.1.1 provides a simplified perspective drawing of such a machine within a host device. The purpose of the tethered motor is to provide a test bed for the induction machine that is free of many of the complexities of the motor-compressor, such as bearings and fluid connections. Simulation results for both the tethered motor and the motor-compressor are similar, so for brevity, this appendix will present results only in the context of the motor-compressor. The appendix is intended to be a description of the models used to understand and design the micro-scale electric induction machine.

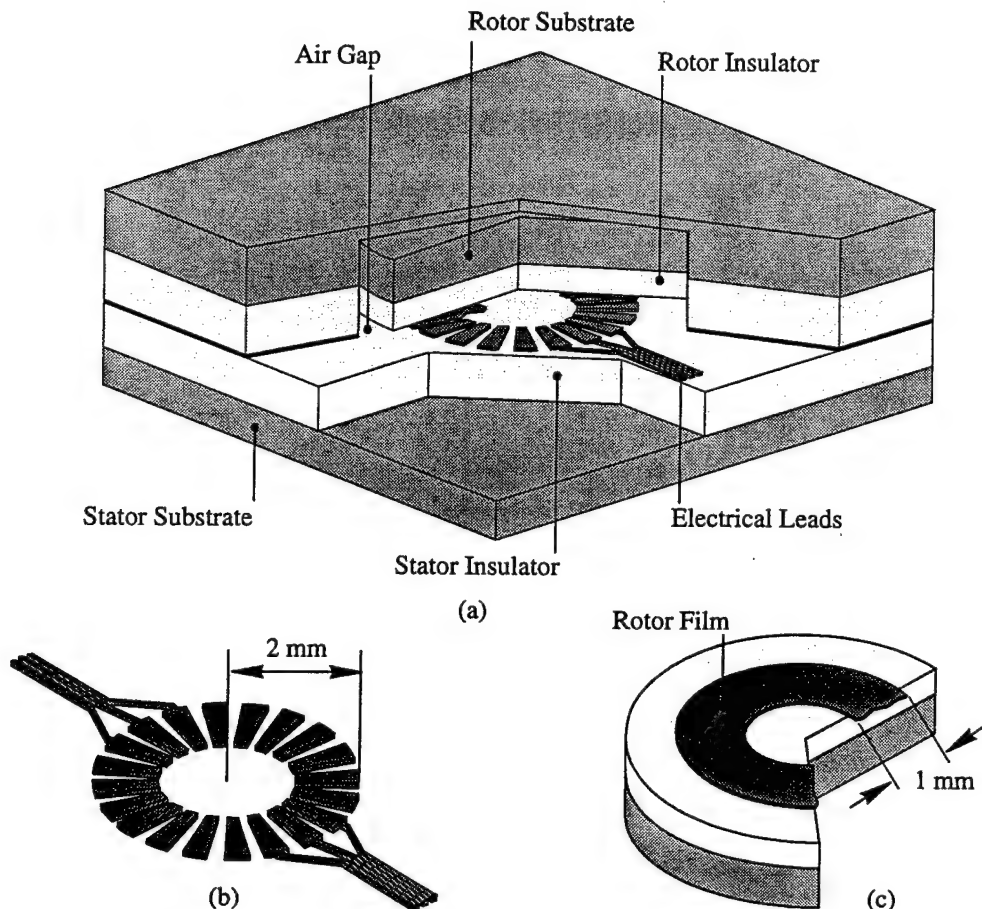


Figure A.1.1: A simplified three-dimensional model of a micro-scale electric induction machine showing (a) an assembled device, (b) the stator electrodes, and (c) the rotor disk, turned over to show the slightly conducting rotor film. This picture shows only features relevant to the electromechanical design; for example, turbine/compressor blades or tethers are removed. Also, the material thicknesses are not to scale and the actual device would have many more stator electrodes than shown in part (b).

Figure A.1.1 depicts the four major characteristics most relevant to an electromechanical description of the induction machine. First, the figure shows insulating layers that serve to separate the heart of the machine from the outer bulk substrates. Second, Figure A.1.1(c) shows the location and extent of the slightly-conducting rotor film. The rotor film will be designed to have a specific electrical conductivity. That conductivity will be chosen in conjunction with the electrical excitation frequency and the desired rotation speed of the rotor disk. Maintenance of the conductivity will be critical for successful operation of the device. The area of the rotor film is the only torque producing area of the machine and will be referred to as the active area of the electric induction machine. Third, the rotor is a three-dimensional (3D) disk which carries the annular rotor film on its bottom surface; and it rotates around a vertical axis. Finally, part (b) of the figure highlights the finite number and discrete geometry of the stator excitation electrodes, as well as their connection to the outside world via only six electrical leads.

Figure A.1.1 is not drawn to scale; it is merely an illustration designed to introduce the micro-scale electric induction machine. Some differences between the picture and reality are particularly relevant to the discussion of the following sections, so they will be pointed out now. In particular, fabrication constraints limit the thickness of the insulating layers to approximately 1/40th the thickness of the substrate layers; which is much thinner than the illustrated thickness. Also, the width of the electrodes is greatly exaggerated while their number is greatly reduced. The actual number and width would not be resolvable on the scale of the drawing. The actual device will contain over 30 times the number of electrodes shown in the figure. The actual number has been chosen to approximate a sinusoidal traveling wave of electric potential on the stator electrodes and a high number results in a more powerful machine. Furthermore, the machine will have six connections to the outside world, and will be operated as a six-phase electric machine. The implications of this number will be discussed in the last section of this appendix.

The appendix is organized to provide a description of the specific steps taken toward an electromechanical understanding of the machine in Figure A.1.1. Along the way, three different models are used to develop the description; after the first, each model builds on the previous. The models can be summarized with respect to the four major characteristics of an electric induction machine that were described in the second paragraph. To begin, Section A.2 describes a two-dimensional (2D) model. This model preserves the first two characteristics but not the remaining two. With respect to the third characteristic, the model describes the electromechanics of a 2D plane sliding past a stationary plane, rather than a 3D disk rotating past a stationary disk. In addition, the model assumes that the stator is excited with a travelling wave made of a single spatial harmonic. Thus, it does not account for the finite number of discrete electrodes actually used in the machine. Next, in Section A.3, the 2D single-harmonic model is transformed to define

an approximate cylindrical 3D single-harmonic model which more closely resembles the actual geometry. The 2D model is effectively warped to follow the surface of the rotor disk. In this way, the 3D single-harmonic model preserves the first three characteristics, but not the last. Finally, in Section A.4, a more accurate 3D model is described which accounts for the discrete nature of the stator electrodes. This model preserves all four major characteristics of the electric machine pictured in Figure A.1.1 and represents the most complete electromechanical description of the micro-scale electric induction machine that has been developed to date.

## **A.2 The 2D Single-Harmonic Model**

A simple two-dimensional model can be a useful tool for understanding the micro-scale electric induction machine, such as that illustrated in Figure A.1.1. It is possible to analyze a precise cylindrical three-dimensional model of the machine, and this has been done; but that solution need not be used. It contains series combinations of high-order Bessel functions within integral equations. These equations provide a description that is computationally excessive for both design purposes and a fundamental understanding of electromechanical phenomena. This section describes the 2D single-harmonic model, providing the foundation for an approximate cylindrical 3D description to be developed in Section A.3.

### **A.2.1 Geometry**

A precise cylindrically-symmetric 3D model of the device shown in Figure A.1.1 is more computationally intense than required for a useful analysis. A much simpler model is constructed in this section. Instead of a disk which rotates past the stator, the 2D single-harmonic model describes a semi-infinite rotor half-space that moves linearly past a semi-infinite stator half-space, as depicted in Figure A.2.1. This is similar to analyzing a very thin outer region of a very large disk-shaped machine when the  $x$ -coordinate points in the radial direction. The rotor and stator half-spaces are defined in a complete  $x$ ,  $y$ , and  $z$  coordinate frame, but one need only consider the  $y$  and  $z$  directions. All quantities are assumed to be independent of the  $x$ -coordinate direction. Therefore, the two half-spaces effectively become two half-planes. Section A.3 will describe a more geometrically accurate 3D model, obtained by warping this 2D model onto a disk-shaped surface.

One other major difference between the device in Figure A.1.1 and the 2D single-harmonic model is that the model assumes a single harmonic of potential traveling on the stator. In other words, the model assumes that in some way a single frequency travelling wave can be produced across the electrode surfaces in the  $y$ -coordinate direction, as shown in Figure A.2.1. In reality, the potential would be constant across the surface of each electrode and smoothly varying between neighboring electrodes. Here the 2D model effectively assumes an infinite number of

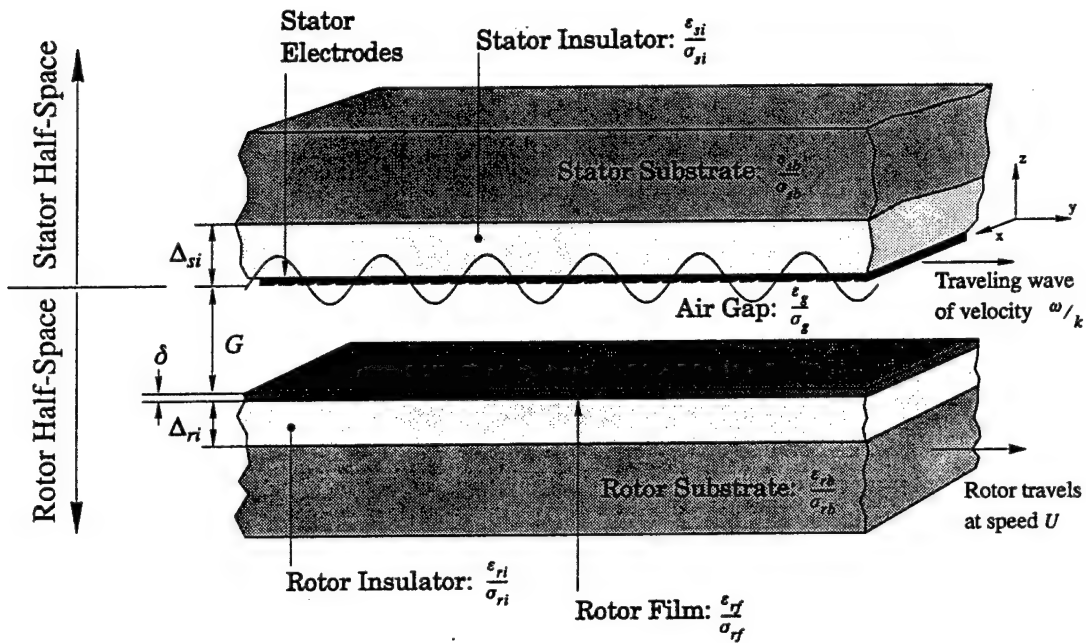


Figure A.2.1: The 2D single-harmonic model of the electric induction machine. The ratio labeling each of the six regions is the charge relaxation time for that region. The thicknesses of the substrate regions are not labeled since the model assumes infinite thicknesses. The picture is inverted when compared to Figure A.1.1(a).

independent electrodes with no space between them. Section A.4 will describe an approximate 3D model which more accurately models the electrodes as finite in number and separated by insulating space. That model will superpose multiple harmonics of differing wavenumber to produce a more accurate wave shape. For now, the 2D single-harmonic model provides insight into the device in Figure A.1.1.

To analyze the device as modeled in Figure A.2.1, it is convenient to segment the device into six regions: stator substrate, stator insulator, air gap, rotor film, rotor insulator and rotor substrate. The potentials on the interfaces bounding these regions then become the fundamental electromagnetic quantities from which all other electromechanical quantities may be determined. To find the boundary potentials, it is necessary to solve Laplace's equation for each region in terms of the boundary potentials and then combine the solutions through boundary conditions [1]. Because the potential is externally enforced on the stator electrodes at the interface of the stator insulator and the air gap, the solutions to Laplace's equation in the two half-planes are independent of one another. Only the rotor half-plane will be analyzed in detail here. The stator half-plane has been analyzed for its relevance to external power electronic excitation of the stator electrodes, but in the interest of brevity the results are not described here.

### A.2.2 Electromagnetic Analysis

To begin the electromagnetic analysis of the 2D single-harmonic model, it is assumed that the stator electrodes impose a traveling wave of electric potential of the form

$$\phi(x, y, z = 0) = \Re \left\{ \hat{V} e^{j(ky - \omega t)} \right\} \quad \text{A.2.1}$$

over their surface adjoining the air gap. The quantity  $\hat{V}$  is the complex potential amplitude of the traveling wave and  $k$  is its wavenumber. In terms of the wavenumber, or spatial frequency, and the temporal electrical excitation frequency  $\omega$ , the phase velocity of the stator potential wave is  $\omega/k$ , in the  $y$ -coordinate direction.

For convenience, this document will work primarily with complex quantities. However, at times real quantities are necessary. So for brevity, the notation

$$X(x, y, z, t) = \Re \left\{ \hat{X}(x, y, z, t) \right\} \quad \text{A.2.2}$$

is defined for use throughout this document.

In each of the six regions, Laplace's equation for the complex electric potential  $\hat{\phi}(x, y, z, t)$  in cartesian coordinates takes the form

$$\frac{\partial^2 \hat{\phi}}{\partial x^2} + \frac{\partial^2 \hat{\phi}}{\partial y^2} + \frac{\partial^2 \hat{\phi}}{\partial z^2} = 0. \quad \text{A.2.3}$$

The solution to Laplace's equation in the air gap of the 2D single-harmonic model with  $z = 0$  at the electrode surface can be written as

$$\hat{\phi}_g(x, y, z, t) = \frac{\hat{V} \sinh[k(z + G)] - \hat{\Phi}_{ri} \sinh(kz)}{\sinh(kG)} e^{j(ky - \omega t)} \quad \text{A.2.4}$$

where  $\hat{V}$  is the complex amplitude of the potential waveform on the stator surface. This applied potential induces a potential waveform on the rotor film whose complex amplitude is  $\hat{\Phi}_{ri}$ . Similarly, the solution of Laplace's equation in the rotor insulator is

$$\hat{\phi}_{ri}(x, y, z, t) = \frac{\hat{\Phi}_{ri} \sinh[k(z + G + \Delta_{ri})] - \hat{\Phi}_{rb} \sinh[k(z + G)]}{\sinh(k\Delta_{ri})} e^{j(ky - \omega t)} \quad \text{A.2.5}$$

where  $\hat{\Phi}_{rb}$  is the induced potential amplitude at the interface of the rotor insulator and the rotor substrate. In Equations A.2.4 and A.2.5 the variables  $G$  and  $\Delta_{ri}$  refer to the air gap thickness and

rotor insulator thickness, respectively, as shown in Figure A.2.1.

In arriving at Equation A.2.5, the rotor film has been treated as a sheet of zero thickness. Specifically, this assumes that the potential at the interface of the air gap and rotor film is exactly the same as the potential at the interface between the rotor film and rotor insulator. This is valid as long as the rotor film thickness  $\delta$  in Figure A.2.1 is very much smaller than one spatial wavelength  $2\pi/k$  of the potential solution. This condition is easily satisfied in all cases examined in this appendix.

There are two unknowns in Equations A.2.4 and A.2.5:  $\hat{\Phi}_{ri}$ , and  $\hat{\Phi}_{rb}$ . Determination of their values would require the simultaneous solution of two equations. However, the analysis may be simplified. The rotor substrate is expected to be several orders of magnitude more conductive than either the rotor film or the rotor insulator. This is not a preferred situation since a very conductive rotor substrate tends to short out the rotor film, which will be made of a very resistive but not perfectly insulating material. As a result, the rotor insulator is included in an attempt to ensure that the potential from the rotor film is permitted to decay well before reaching the rotor substrate. Any non-zero potential that penetrates the insulator leads to a loss in overall performance. Unfortunately, fabrication constraints limit both the thickness of the rotor insulator and the choice of the rotor substrate material. The rotor substrate will be silicon here and can be modeled as a perfect conductor when its conductivity is compared to that of either the rotor film or the insulator, which will be silicon dioxide.

Treating the rotor substrate as a perfect conductor simplifies the analysis. Specifically, the potential within the rotor substrate becomes constant. Further, since the stator excitation averages to zero in time and space, the constant rotor substrate potential is zero. Thus,

$$\hat{\Phi}_{rb} = 0.$$

This simplifies Equation A.2.5 so that the two relevant potential descriptions are now, repeating Equation A.2.4,

$$\hat{\phi}_g(x, y, z, t) = \frac{\hat{V} \sinh[k(z + G)] - \hat{\Phi}_{ri} \sinh(kz)}{\sinh(kG)} e^{j(ky - \omega t)} \quad \text{A.2.4}$$

$$\hat{\phi}_{ri}(x, y, z, t) = \frac{\hat{\Phi}_{ri} \sinh[k(z + G + \Delta_{ri})]}{\sinh(k\Delta_{ri})} e^{j(ky - \omega t)} \quad \text{A.2.6}$$

Equations A.2.4 and A.2.6 may be used to find all other electromagnetic and electromechanical quantities in the air gap and in the rotor insulator. For example, the electric field is given by

$$\hat{\vec{E}} = -\nabla\hat{\phi} \quad \text{A.2.7}$$

in each region. The electric field is then used to find the displacement field, which is defined in terms of the isotropic material permittivity  $\epsilon$  as

$$\hat{\vec{D}} = \epsilon\hat{\vec{E}}.$$

And finally, the displacement field is used to find the free surface charge density at the interface between any two regions [2]

$$\hat{\rho} = \hat{n}_{ba} \cdot (\hat{\vec{D}}_a - \hat{\vec{D}}_b)$$

where  $\hat{n}_{ba}$  is a unit vector directed from region  $b$  to region  $a$ .

At this point, the only unknown in Equations A.2.4 and A.2.6 is the complex potential amplitude  $\hat{\Phi}_{ri}$ . This unknown may be found by applying charge conservation at the rotor film.

Charge conservation at the rotor film involves the conduction surface charge on the rotor film, given by

$$\hat{\rho}_{rf} = \hat{n} \cdot (\bar{\vec{D}}_g - \bar{\vec{D}}_{ri}) = \epsilon_{ri} \frac{\partial \hat{\phi}_{ri}}{\partial z} \Big|_{z=-G^-} - \epsilon_g \frac{\partial \hat{\phi}_g}{\partial z} \Big|_{z=-G^+} \quad \text{A.2.8}$$

and can be stated as

$$\left( \frac{\partial}{\partial t} + U \frac{\partial}{\partial y} \right) \hat{\rho}_{rf} + \frac{\partial}{\partial y} \delta \sigma_{rf} \hat{E}_{riy} + \sigma_{ri} \frac{\partial \hat{\phi}_{ri}}{\partial z} \Big|_{z=-G^-} = 0 \quad \text{A.2.9}$$

since the conductivity of the air gap  $\sigma_g$  is assumed to be zero. In this equation, the first term is a convective derivative to account for the speed  $U$  of the rotor and the grouping  $\delta \sigma_{rf}$  will henceforth be referred to as the rotor film sheet conductivity  $\sigma_{rfs}$ . In the second term,  $\hat{E}_{riy}$  is the tangential component of the electric field at the interface of the rotor insulator and the rotor film, or  $z = -G$ .

All quantities in Equation A.2.9 may be expressed in terms of Equations A.2.4 and A.2.6 and then expanded in terms of their definitions. The result of that expansion is



$$\frac{1}{\omega} \left[ k\sigma_{rfs} + \sigma_{ri} \frac{\cosh(k\Delta_{ri})}{\sinh(k\Delta_{ri})} \right] \hat{\Phi}_{ri} = \quad \text{A.2.10}$$

$$j \frac{(\omega - kU)}{\omega} \left[ \frac{\epsilon_g}{\sinh(kG)} \hat{V} - \left( \epsilon_g \frac{\cosh(kG)}{\sinh(kG)} + \epsilon_{ri} \frac{\cosh(k\Delta_{ri})}{\sinh(k\Delta_{ri})} \right) \hat{\Phi}_{ri} \right]$$

This equation can be solved for  $\hat{\Phi}_{ri}$  and simplified to yield

$$\hat{\Phi}_{ri} = \frac{1}{\beta} \cdot \frac{j\tau_R \omega S}{1 + j\tau_R \omega S} \cdot \hat{V} \quad \text{A.2.11}$$

where the variables have been grouped in terms of quantities inspired by physical phenomena. For example,  $\tau_R$  is the equivalent charge relaxation time [3] of the combined rotor and air gap and is defined here as

$$\tau_R \equiv \frac{\epsilon_{eff}}{\sigma_{eff}} \quad \text{A.2.12}$$

Further, the quantities

$$\sigma_{eff} = k\sigma_{rfs} + \sigma_{ri} \frac{\cosh(k\Delta_{ri})}{\sinh(k\Delta_{ri})} \quad \text{A.2.13}$$

and

$$\epsilon_{eff} = \epsilon_g \frac{\cosh(kG)}{\sinh(kG)} + \epsilon_{ri} \frac{\cosh(k\Delta_{ri})}{\sinh(k\Delta_{ri})} \quad \text{A.2.14}$$

are the effective conductivity and the effective permittivity, respectively, of the air gap and rotor shown in Figure A.2.1. Recall that  $\omega$  is simply the electrical excitation frequency. Next the slip  $S$  in Equation A.2.11 is defined as the difference between that frequency and the effective mechanical frequency  $kU$  of the rotor, normalized by  $\omega$ . Thus,

$$S = \frac{\omega - kU}{\omega} \quad \text{A.2.15}$$

Slip describes the relative speed by which the stator potential wave “slips” past the rotor structure. In other words, the slip is the phase velocity of the stator potential wave relative to the rotor,

expressed as a fraction of the stator potential phase velocity. This can be shown through a division of top and bottom by  $k$ .

Note from Equation A.2.4, however, that the potential wave induced on the rotor surface travels at exactly the same phase velocity as the wave on the stator. The induced rotor charges conduct mainly through the rotor film; i.e., along the rotor surface. If the rotor insulator has a low enough resistivity, then there is only negligible conduction through that region. The image charges on the rotor will either lead their images on the stator or lag them depending on whether the induction machine operates as a generator or a motor, respectively.

It can be shown that the magnitude of the slip time, defined here as

$$\tau_s \equiv \frac{1}{\omega S}, \quad \text{A.2.16}$$

is precisely the time it takes the induced rotor surface potential waveform to travel exactly one wavelength through the rotor, parallel to and in the same direction as, the rotor velocity. For reasons that will be made clear in Section A.3.4.1, it is convenient to define the characteristic time ratio

$$\Gamma \equiv \frac{\tau_R}{\tau_s} = \tau_R \omega S. \quad \text{A.2.17}$$

It will be seen that power from the micro-scale electric induction machine is maximized when the characteristic time ratio  $\Gamma$  is equal to unity.

The remaining term in Equation A.2.11

$$\beta = \frac{\epsilon_{eff}}{\epsilon_g} \sinh(kG) \quad \text{A.2.18}$$

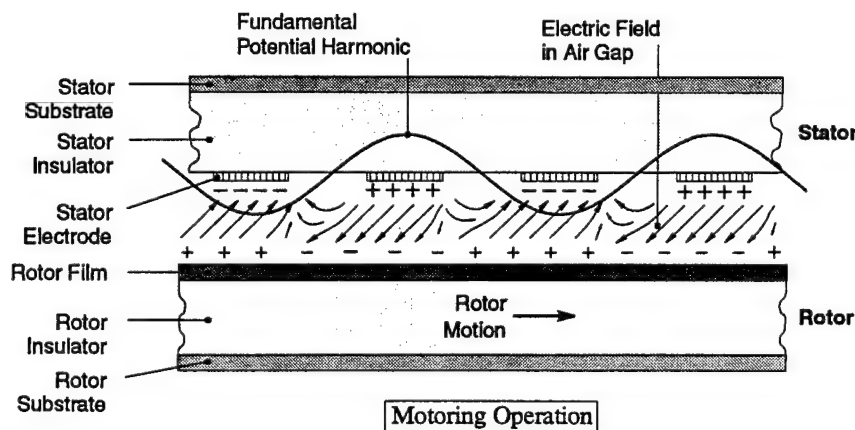


Figure A.2.2: Illustration of the electric field in the air gap of the micro-scale electric induction machine.

has a less tangible meaning but does capture the effects of two important phenomena. First, the term describes a lower induced rotor film potential due to the rotor substrate short circuit which occurs when the rotor insulator thickness  $\Delta_{ri}$  is less than ideal. Second, for a greater than ideal air gap length  $G$ , it describes a similar short circuit effect due to excessive fringing between the positive and negative half-cycles of the stator potential. Figure A.2.2 depicts fringing as the curved fields lines which extend between neighboring electrodes. If there were excessive fringing, most field lines would extend from charges on one electrode to their image charges on neighboring electrodes, rather than extending to induced image charges at the rotor film as shown by the straight field lines in Figure A.2.2. For both phenomena, ideal refers to the situation in which  $\beta$  approaches unity. This would be the case if  $G$  were made much less than the decay length  $1/k$  in the  $z$ -coordinate direction; and ideality is further approached by making  $\Delta_{ri}$  much larger than  $G$  and by making  $\epsilon_g$  much greater than  $\epsilon_{ri}$ .

The next section will use the electric fields in the air gap and rotor insulator to determine the electromagnetic forces which act on the surface of the rotor through the charges that reside there. One final result of Section A.2 will be that these forces are related to the induced rotor surface potential and therefore have strong dependencies on the characteristic time ratio  $\Gamma$  and on the shorting term  $\beta$ .

### A.2.3 Forces of Electromagnetic Origin

Using Equation A.2.7, expressions for the electric fields shown in Figure A.2.2 along with those in the rotor insulator may be obtained from the potential and used to determine the force on the rotor. The force on any body is conveniently expressed using the electromagnetic stress tensor. The electromagnetic stress tensor is defined [3] in terms of the electric fields and the permittivity of the material surrounding the body as

$$T_{mn} = \epsilon E_m E_n - \frac{\epsilon}{2} \delta_{mn} E_k E_k \quad \text{A.2.19}$$

where  $m$  and  $n$  each refer to the coordinate  $x$ ,  $y$  or  $z$ . To find the force on a body, the stress tensor must be evaluated over a closed surface surrounding only that body, according to the integral

$$\bar{F} = \oint_S \bar{T} \cdot d\bar{S} = \oint_S T_{mn} dS_n \quad \text{A.2.20}$$

where  $S$  represents the box-shaped enclosing surface. A 2D cross-section of this closed surface, surrounding a single wavelength section of the 2D rotor, is shown in Figure A.2.3. The integral of Equation A.2.20 may be divided into six pieces, one for each face of  $S$ , and the problem can be simplified. The contributions from the two faces at  $x = 0$  and  $x = W_x$  cancel because the fields

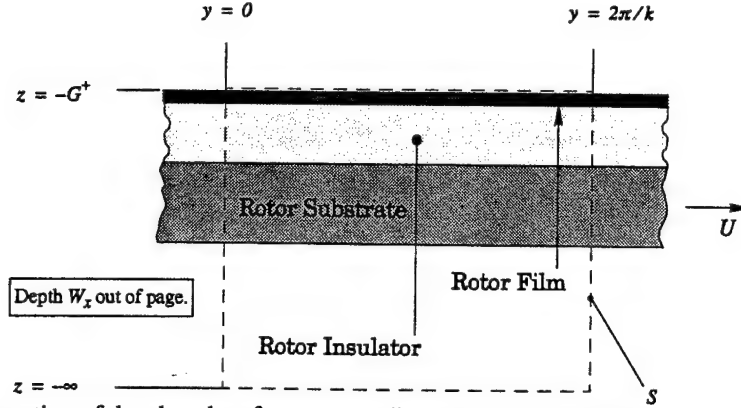


Figure A.2.3: Cross section of the closed surface surrounding the rotor of the 2D single-harmonic model over which the electromagnetic stress tensor is evaluated to find the force on a single wavelength unit cell of the rotor.

do not depend on  $x$  and the normal differential area elements  $d\vec{S}$  over each face are oppositely directed. Similarly, the contributions from  $y = 0$  and  $y = 2\pi/k$  cancel because the fields are periodic in  $2\pi/k$ . In addition, the face at  $z = -\infty$  does not contribute since in general all fields decay to zero as  $z \rightarrow -\infty$ ; in fact, fields below  $\Delta_{ri}$  vanish as described in Section A.2.2. The only remaining surface is the one at  $z = -G^+$ . When this final piece of the integral is evaluated, it is found that the total force on the single wavelength section of the rotor has only the two components

$$F_y = \int_0^{\frac{2\pi}{k} W_x} \int_0^{\frac{2\pi}{k} W_x} \epsilon_g [E_y E_z] \Big|_{z=-G^+} dy dx \quad \text{A.2.21}$$

$$F_z = \int_0^{\frac{2\pi}{k} W_x} \int_0^{\frac{2\pi}{k} W_x} \frac{\epsilon_g}{2} [E_z E_z - E_y E_y] \Big|_{z=-G^+} dy dx. \quad \text{A.2.22}$$

Now note that the stress tensor is a real quantity, therefore the electric fields in Equations A.2.21 and A.2.22 must be expressed as real quantities. Since the analysis to this point has been carried out in complex space, the fields obtained from the potential descriptions in Equations A.2.4 and A.2.6 must be converted from complex space to real space. Thus, for example,

$$E_y E_z \Rightarrow \Re \left\{ \tilde{E}_y e^{j(ky - \omega t)} \right\} \Re \left\{ \tilde{E}_z e^{j(ky - \omega t)} \right\}$$

in which the definition

$$\tilde{X}_n = \frac{\hat{X}_n}{e^{j(ky - \omega t)}}$$

has been made for notational convenience. Note that  $\tilde{X}_n$  has no  $y$ -coordinate or time dependence. Then, through purely algebraic manipulation, Equations A.2.21 and A.2.22 reduce to

$$F_y = \int_0^{\frac{2\pi}{k} W_x} \int_0^{\frac{\epsilon_g}{2}} \Re\{\tilde{E}_y^* \tilde{E}_z\} \Big|_{z=-G^+} dy dx \quad \text{A.2.23}$$

$$F_z = \int_0^{\frac{2\pi}{k} W_x} \int_0^{\frac{\epsilon_g}{4}} \Re\{\tilde{E}_z^* \tilde{E}_z - \tilde{E}_y^* \tilde{E}_y\} \Big|_{z=-G^+} dy dx. \quad \text{A.2.24}$$

Further, since  $\tilde{X}_n$  is independent of the  $y$ -coordinate and time, the space and time averaged forces per unit area may be conveniently defined as

$$f_y = \frac{F_y}{\left( \int_0^{\frac{2\pi}{k} W_x} \int_0^{\frac{\epsilon_g}{2}} dy dx \right)} = \frac{\epsilon_g}{2} \Re\{\tilde{E}_y^* \tilde{E}_z\} \Big|_{z=-G^+} \quad \text{A.2.25}$$

and similarly

$$f_z = \frac{\epsilon_g}{4} \Re\{\tilde{E}_z^* \tilde{E}_z\} \Big|_{z=-G^+} - \frac{\epsilon_g}{4} \Re\{\tilde{E}_y^* \tilde{E}_y\} \Big|_{z=-G^+}. \quad \text{A.2.26}$$

Finally, using the potential descriptions of Equations A.2.4 and A.2.6, the average force densities for the 2D single-harmonic model are summarized as a tangential force per unit area

$$f_y = \frac{\epsilon_g k^2 |\hat{V}|^2}{2\beta \sinh(kG)} \cdot \frac{\Gamma}{1 + \Gamma^2}. \quad \text{A.2.27}$$

and a normal force per unit area

$$f_z = \epsilon_g \left[ \frac{k |\hat{V}|}{2\beta \sinh(kG)} \right]^2 \cdot \frac{\beta^2 + \{[\beta - \cosh(kG)]^2 - [\sinh(kG)]^2\} \Gamma^2}{1 + \Gamma^2}. \quad \text{A.2.28}$$

#### A.2.4 Summary

This section described a 2D model of a micro-scale electric induction machine such as that shown in Figure A.1.1. The model is defined in a cartesian coordinate system as shown in Figure A.2.1. The stator electrodes in this model are excited with a single-frequency potential wave, propagating along them in the y-coordinate direction. However, because the model is 2D, it cannot capture the 3D aspects of the problem. Section A.3 will describe an approximate 3D model, based on the 2D single-harmonic model, to account for the 3D nature of proposed induction machine.

### A.3 The 3D Single-Harmonic Model

To date, all micro-scale devices which will use an electric induction machine are disk-like in geometry. Therefore, it is useful to transform the simplified 2D analysis above, which is a very good approximation, to a more realistic 3D analysis. The assumption of infinite electrodes is retained so that the 3D model is a 3D single-harmonic model. This section describes the derivation of the 3D single-harmonic model and describes device performance results based on that model. The single-harmonic solution is later expanded upon in Section A.4. That section sets forth a method for analyzing a more precise 3D model which accounts for the finite number of stator electrodes, separated by an insulating space by incorporating multiple harmonics.

#### A.3.1 Transforming to the 3D Single-Harmonic Model

Here, the 2D single-harmonic model is transformed to become a 3D model. Figure A.3.1(c) shows that such a model has the cylindrical geometry of the device in Figure A.1.1(a), but still assumes the number of electrodes to be infinite. Therefore the traveling wave on the electrodes is still perfectly sinusoidal in space, as shown in Figure A.3.1(b). A 3D model is useful because it very accurately describes rotating machinery instead of planes sliding by one another as in Figure A.2.1, summarized in Figure A.3.1(a).

The 3D single-harmonic model is obtained from the 2D single-harmonic model using the cartesian to cylindrical coordinate map delineated in the left column of Figure A.3.1(d). The right column shows a few key results of the coordinate map. The map is an analogy between the two coordinate systems which, in effect, bends rectangular strips from the 2D model around the curvature of the rotor disk; the process is represented in Figure A.3.1(c). The accuracy of the 3D model obtained by this process depends upon the effective local curvature of the mapped fields everywhere in the active region of the induction machine.

##### A.3.1.1 Transformation Analysis

Quantitative bounds on the cylindrical coordinate space follow from a mathematical

treatment of the mapping process. To begin, recall that the 2D cartesian solution to Laplace's equation is of the form

$$\hat{\phi} \propto e^{jky} e^{kz}.$$

To apply the cartesian results to a cylindrical geometry in an approximate manner, it is necessary only to apply the coordinate map shown in the first column of Figure A.3.1(d). Then the solution in cylindrical coordinates is approximated by

$$\hat{\phi}^* \propto e^{jm\theta} e^{\frac{m}{r}z} \quad \text{A.3.1}$$

where the superscript  $*$  denotes an approximation resulting from the mapping. Here  $m$  is the angular wavenumber, or the number of wavelengths within the voltage waveform enforced around the stator, such as the one in Figure A.3.1(b). To be consistent with previous work on electric induction machines,  $m$  will henceforth be referred to as the *periodicity* of the machine. The same periodicity is characteristic of all fields in the electric induction machine.

Equation A.3.1 will be a good approximation only within a certain range of the cylindrical coordinates  $(r, \theta, z)$ . To define this range,  $\hat{\phi}^*$  is inserted into the cylindrical coordinate form of Laplace's equation

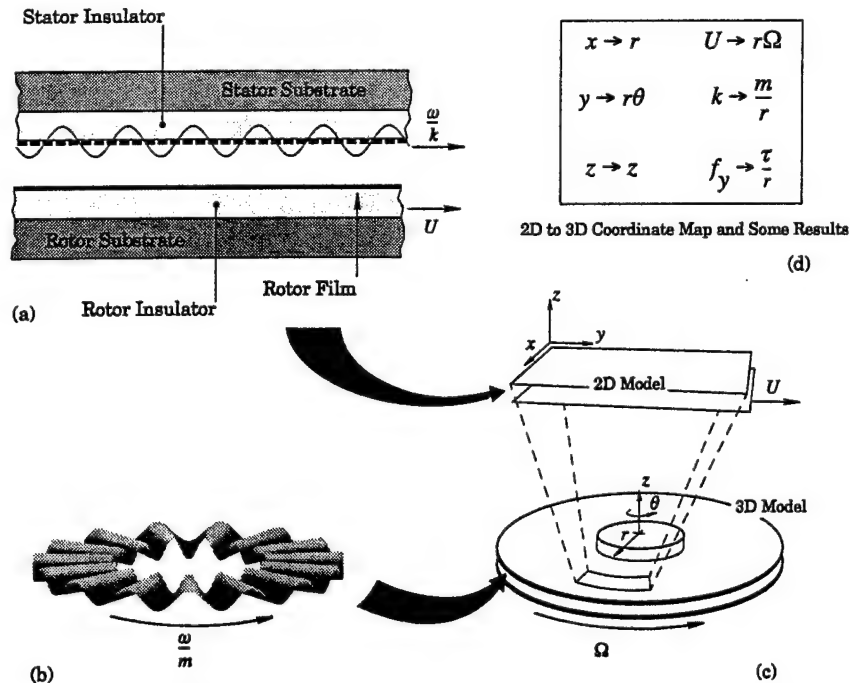


Figure A.3.1: The process of mapping the 2D single-harmonic model to a 3D single-harmonic model: (a) a summary of the 2D model, (b) the 3D single-harmonic stator potential wave, (c) depiction of the mapping process, (d) the coordinate map and some results.

$$\frac{1}{r} \frac{\partial}{\partial r} \left( r \frac{\partial \phi}{\partial r} \right) + \frac{1}{r^2} \frac{\partial^2 \phi}{\partial \theta^2} + \frac{\partial^2 \phi}{\partial z^2} = 0, \quad \text{A.3.2}$$

leading to

$$\frac{1}{r} \frac{\partial}{\partial r} \left( r \frac{\partial \hat{\phi}^*}{\partial r} \right) - \frac{m^2}{r^2} \hat{\phi}^* + \frac{m^2}{r^2} \hat{\phi}^* = 0. \quad \text{A.3.3}$$

Equation A.3.3 shows that the second and third terms of Laplace's equation cancel. However, expansion of the first term reveals that

$$\frac{1}{r} \frac{\partial}{\partial r} \left( r \frac{\partial \hat{\phi}^*}{\partial r} \right) = \frac{mz}{r^3} \hat{\phi}^* + \frac{m^2 z^2}{r^4} \hat{\phi}^*. \quad \text{A.3.4}$$

This term cannot always be zero for useful values of  $m$ ,  $z$  and  $r$ , which would be true if Equation A.3.1 were not an approximation. To preserve the dominant balance of the last two terms in Equation A.3.3 the model description must satisfy

$$\frac{mz}{r^3}, \frac{m^2 z^2}{r^4} \ll \frac{m^2}{r^2}. \quad \text{A.3.5}$$

This leads to the following two conditions

$$\begin{bmatrix} z \ll mr \\ z \ll r \end{bmatrix}. \quad \text{A.3.6}$$

However, it so happens that  $m \gg 1$  for all viable designs; so the second condition is most demanding. This is easily satisfied by current designs whose minimum radii are on the order of millimeters, but whose fields vanish within 100  $\mu\text{m}$  in the  $z$ -coordinate, even when not limited by the substrate layers. Thus, from here on  $\hat{\phi}$  will be taken to mean  $\hat{\phi}^*$ , dropping the superscript  $*$  for notational simplicity.

#### A.3.1.2 Transformation Results: Potentials, Fields and Forces

All equations for the electric potential, fields, and forces will now be summarized for the 3D single-harmonic model derived from the 2D to 3D transformation. In all of the following equations,

$$\hat{\Phi}_{ri} = \frac{1}{\beta(r)} \cdot \frac{j\Gamma(r)}{1 + j\Gamma(r)} \cdot \hat{V}, \quad \text{A.3.7}$$



$$\Gamma(r) \equiv \tau_R(r) \omega S \quad \text{A.3.8}$$

and

$$\beta(r) = \frac{\varepsilon_{eff}(r)}{\varepsilon_g} \sinh\left(\frac{m}{r} G\right) \quad \text{A.3.9}$$

where the slip  $S$  is now given by

$$S = \frac{\omega - m\Omega}{\omega} \quad \text{A.3.10}$$

and  $\Omega$  is the rotor speed in radians per second. The relaxation time is now dependent on the radius as

$$\tau_R(r) \equiv \frac{\varepsilon_{eff}(r)}{\sigma_{eff}(r)} \quad \text{A.3.11}$$

in which

$$\sigma_{eff}(r) = \frac{m}{r} \sigma_{rfs} + \sigma_{ri} \frac{\cosh\left(\frac{m}{r} \Delta_{ri}\right)}{\sinh\left(\frac{m}{r} \Delta_{ri}\right)} \quad \text{A.3.12}$$

and

$$\varepsilon_{eff}(r) = \varepsilon_g \frac{\cosh\left(\frac{m}{r} G\right)}{\sinh\left(\frac{m}{r} G\right)} + \varepsilon_{ri} \frac{\cosh\left(\frac{m}{r} \Delta_{ri}\right)}{\sinh\left(\frac{m}{r} \Delta_{ri}\right)}. \quad \text{A.3.13}$$

Thus the electric potential, fields and force densities become, respectively,

$$\hat{\phi}_g(r, \theta, z, t) = \frac{\hat{V} \sinh\left[\frac{m}{r}(z + G)\right] - \hat{\Phi}_{ri} \sinh\left(\frac{m}{r} z\right)}{\sinh\left(\frac{m}{r} G\right)} e^{j(m\theta - \omega t)} \quad \text{A.3.14}$$

$$\hat{\phi}_{ri}(r, \theta, z, t) = \frac{\hat{\Phi}_{ri} \sinh\left[\frac{m}{r}(z + G + \Delta_{ri})\right]}{\sinh\left(\frac{m}{r}\Delta_{ri}\right)} e^{j(m\theta - \omega t)} \quad \text{A.3.15}$$

$$\hat{\hat{E}}_g(r, \theta, z, t) = \begin{bmatrix} 0 \cdot \hat{i}_r \\ \left(-j\frac{m}{r}\right) \frac{\hat{V} \sinh\left[\frac{m}{r}(z + G)\right] - \hat{\Phi}_{ri} \sinh\left(\frac{m}{r}z\right)}{\sinh\left(\frac{m}{r}G\right)} e^{j(m\theta - \omega t)} \cdot \hat{i}_\theta \\ \left(\frac{m}{r}\right) \frac{-\hat{V} \cosh\left[\frac{m}{r}(z + G)\right] + \hat{\Phi}_{ri} \cosh\left(\frac{m}{r}z\right)}{\sinh\left(\frac{m}{r}G\right)} e^{j(m\theta - \omega t)} \cdot \hat{i}_z \end{bmatrix} \quad \text{A.3.16}$$

$$\hat{\hat{E}}_{ri}(r, \theta, z, t) = \begin{bmatrix} 0 \cdot \hat{i}_r \\ \left(-j\frac{m}{r}\right) \frac{\hat{\Phi}_{ri} \frac{m}{r} \cosh\left[\frac{m}{r}(z + G + \Delta_{ri})\right]}{\sinh\left(\frac{m}{r}\Delta_{ri}\right)} e^{j(m\theta - \omega t)} \cdot \hat{i}_\theta \\ \left(\frac{m}{r}\right) \frac{-\hat{\Phi}_{ri} \cosh\left[\frac{m}{r}(z + G + \Delta_{ri})\right]}{\sinh\left(\frac{m}{r}\Delta_{ri}\right)} e^{j(m\theta - \omega t)} \cdot \hat{i}_z \end{bmatrix} \quad \text{A.3.17}$$

$$f_\theta = \frac{\varepsilon_g \left(\frac{m}{r}\right)^2 |\hat{V}|^2}{2\beta(r) \sinh\left(\frac{m}{r}G\right)} \cdot \frac{\Gamma(r)}{1 + \Gamma(r)^2} \quad \text{A.3.18}$$

and

$$f_z = \varepsilon_g \left[ \frac{\frac{m}{r} |\hat{V}|}{2\beta(r) \sinh\left(\frac{m}{r}G\right)} \right]^2 \cdot \frac{\beta(r)^2 + \left\{ \left[ \beta(r) - \cosh\left(\frac{m}{r}G\right) \right]^2 - \left[ \sinh\left(\frac{m}{r}G\right) \right]^2 \right\} \Gamma(r)^2}{1 + \Gamma(r)^2} \quad \text{A.3.19}$$

The torque and motoring power may be found from Equation A.3.18. Torque is obtained by integrating the tangential force on the rotor film multiplied by the lever arm to the point of application on the rotor surface, over only the extent of the rotor film. This results in

$$\tau = \varepsilon_g \pi |\hat{V}|^2 \int_{R_i}^{R_o} \left\{ \frac{\Gamma(r)}{1 + \Gamma^2(r)} \cdot \frac{1}{\beta(r)} \cdot \frac{m^2}{\sinh\left(\frac{mG}{r}\right)} \right\} dr. \quad \text{A.3.20}$$

Then if positive power is defined as mechanical energy flowing out of the machine and electrical energy flowing in, the mechanical shaft power supplied by the machine to a load, such as a compressor, is simply

$$P_m = \Omega \tau = \varepsilon_g \pi |\hat{V}|^2 \Omega \int_{R_i}^{R_o} \left\{ \frac{\Gamma(r)}{1 + \Gamma^2(r)} \cdot \frac{1}{\beta(r)} \cdot \frac{m^2}{\sinh\left(\frac{mG}{r}\right)} \right\} dr. \quad \text{A.3.21}$$

Further, the motoring efficiency of the electric induction machine is

$$\eta_m = \frac{m\Omega}{\omega} \quad \text{A.3.22}$$

so that the electrical power supplied to the induction machine by external power electronics is

$$P_e = \frac{P_m}{\eta_m} = \frac{\omega P_m}{m\Omega} \quad \text{A.3.23}$$

when losses in the stator and interconnect conductors are negligible.

Generating operation will not be discussed here. There are specific issues when the machine behaves as a generator and many of these have been summarized with annual review presentations in the past. Since most issues which are specific to generating are not relevant to the near-term goal of the motor-compressor, they will be documented at a later time.

### **A.3.2 A Baseline Electric Induction Motor Design**

A set of values for the model parameters has been chosen to coincide with the current design for the motor-compressor, and is listed as the baseline design in Table A.3.1. Trends and insights discussed in Section A.3.3 and Section A.3.4 will also be useful in understanding the design of micro-scale electric induction motors within other host devices.

The following is a discussion of several assumptions that helped to define the baseline values for the model parameters. In most cases, there are well-defined constraints on their variability.

Those without extreme constraints are later analyzed to determine their effects on the performance of the electric induction motor.

Mechanical shaft power, from Equation A.3.21, is one of the most important measures of performance that can be explored so changes in model parameters are discussed mainly in terms of mechanical power. All parameters in the power expression are assigned values, or ranges of values, that come from fabrication constraints and physical limitations, as well as trade-offs with

**Table A.3.1 Parameters and assigned values used in the 3D single-harmonic model for results in this appendix.**  
This is the baseline design for the micro-scale electric induction motor hosted by both the tethered motor and the motor-compressor.

Parameter	Value in Baseline Design	Comments.
$\epsilon_g$	$\epsilon_o$	Stator-rotor gap or "air gap" permittivity.
$\epsilon_{ri}$	$3.9\epsilon_o$	Rotor insulator ( $\text{SiO}_2$ ) permittivity.
$\hat{V}$	300 V	Stator potential waveform amplitude. Limited by the breakdown strength of the gas or fluid in the air gap and between the electrodes, and the breakdown strength of external power electronic circuit components.
$G$	3 $\mu\text{m}$	Air gap width.
$m$	131	Waveform periodicity.
$\Delta_{ri}$	10 $\mu\text{m}$	Rotor insulator thickness.
$\sigma_{rfs}$	5.0 nS	Rotor thin film sheet conductivity.
$\sigma_{ri}$	$1.0 \times 10^{-14}$ S/cm	Rotor insulator ( $\text{SiO}_2$ ) conductivity.
$R_i$	1.0 mm	Rotor film inner radius.
$R_o$	1.9 mm	Rotor film outer radius.
$R_d$	2.0 mm	Rotor disk outer radius.
$v_{tip}$	0-250 m/s	Compressor blade tip speed. Speed of rotor disk at its outer radius.
$\Omega$	$\frac{v_{tip}}{R_d}$	Rotor speed in radians per second.
$f = \omega/2\pi$	2.6 MHz	Stator electrode temporal excitation frequency.

other sub-systems in the host device. Table A.3.1 lists the model parameter values used for the baseline design. Only some of the model parameters can be altered substantially; most, which are discussed next, are determined largely by physical limitations beyond the control of the designer. Others are determined iteratively through their interaction with other sub-systems.

1. To begin, the permittivity of the gap cannot easily differ from the permittivity of free space. The gap must be filled with a low viscosity fluid to avoid excess viscous friction losses; but this fluid must also have a very low conductivity to avoid conduction losses from the electrodes. At this point the fluid of choice is simply air which has a permittivity close to free space and a conductivity of near zero. A more preferred fluid would have the above characteristics with a high permittivity to increase torque by Equation A.3.21; but such fluids may not exist.
2. The rotor insulator must be an insulating material with a low conductivity that can be deposited as a thick film and is compatible with a CMOS process. Thus a good choice is silicon dioxide, which has an extremely low conductivity as shown in Table A.3.1. This choice also determines the rotor insulator permittivity. A low relative permittivity is better and that of  $\text{SiO}_2$  is one of the lowest available at 3.9. For comparison, the second most widely used CMOS-compatible dielectric, silicon nitride, has a relative permittivity of 7.5 and its film thickness is severely limited due to residual stresses. Therefore,  $\text{SiO}_2$  is the best available choice.
3. Experimental evidence suggests that the stator potential is constrained to 300 V by the breakdown voltage in an air-filled gap [5]. Additional constraints on this potential come from the breakdown strength of circuit elements in the external power electronics. Experiments are underway to explore each constraint in more detail.
4. The minimum value of the air gap length is constrained by the breakdown strength of air. At synchronous operation, the rotor potential will be zero by Equation A.2.11 so that a potential gradient from  $|\hat{V}|$  to zero will exist across the air gap. Experimental evidence shows that an electric field of  $3 \times 10^8$  V/m is possible in micron-sized gaps, but this value may be near the limit. Thus, the design point is below the current experimental maximum. As in Number 3 above, additional experiments are underway to explore the limit further.
5. The radial extent of the machine has been determined to coincide with the micro-scale bearing rig already under construction so that information from that experiment may be used to better understand the identical bearings in the motor-compressor.
6. The range of rotor tip speed is chosen according to the compressor power requirements for the first motor-compressor.
7. The electrical frequency is set near its expected maximum. This is determined by circuit components in the external power electronic drive.
8. The periodicity is determined from current fabrication constraints at the inner radius of the stator electrodes and will be discussed further in Section A.4.
9. Finally, rotor film sheet conductivity is determined to place peak mechanical power near the motor-compressor baseline tip speed of 200 m/s. This determination will be discussed in Section A.3.4.1.

Rotor film sheet conductivity  $\sigma_{rfs}$  is not strictly constrained; and its optimum value is largely determined in relation to the periodicity  $m$ , the preferred tip speed, and the frequency limits of the power and control electronics. Changes in the parameters  $v_{tip}$ ,  $\Delta_{ri}$ , and  $m$  are more constrained; but deviation from the baseline values of any of these four parameters can have a substantial effect on machine performance. The effects are directly observed in results from the 3D single-harmonic model. Accordingly, the next section will illustrate trends in mechanical power due to changes in all four parameters  $\sigma_{rfs}$ ,  $v_{tip}$ ,  $\Delta_{ri}$ , and  $m$ . To show how these trends arise, Section A.3.4

will analyze the three separate terms in the power integral of Equation A.3.21.

### A.3.3 Torque and Mechanical Power from the 3D Single-Harmonic Model

This section presents results from the 3D single-harmonic model. The results illuminate several important issues governing micro-scale electric induction motor operation. An understanding of these issues guides not only the design of the induction machine, but also the rest of its host device. The primary measure of performance that will be discussed is the mechanical power output by the induction motor, but mechanical torque is also of concern.

#### A.3.3.1 Trends in Rotor Tip Speed and Rotor Film Sheet Conductivity

Two defining characteristics of all induction motors, magnetic or electric, are immediately evident in the expression for power, Equation A.3.21, repeated here for convenience as

$$P_m = \Omega\tau = \varepsilon_g \pi |\hat{V}|^2 \frac{v_{tip}}{R_d} \int_{R_i}^{R_o} \left\{ \overset{\textcircled{1}}{\frac{\Gamma(r)}{1 + \Gamma^2(r)}} \cdot \overset{\textcircled{2}}{\frac{1}{\beta(r)}} \cdot \overset{\textcircled{3}}{\frac{m^2}{\sinh\left(\frac{mG}{r}\right)}} \right\} dr \quad A.3.24$$

The three terms in the integral are labeled for later reference and it is helpful to note that

$$v_{tip} = R_d \Omega \quad A.3.25$$

The first characteristic is that the mechanical power supplied to a load will be zero at synchronous speed. At synchronous speed, the speed of the rotor equals the speed of the stator potential wave so the slip  $S$  is zero. It is clear from Equation A.3.8 and Equation A.3.10 that Term 1 will be zero at this speed. For the electric motor, zero slip means that the induced rotor charges lie directly below the applied stator charges. Thus, the electric field lines are not tilted as shown in Figure A.2.2 and the tangential force from Equation A.3.18 is zero, providing no torque to the rotor. The second characteristic of induction motors is that Term 1 can be maximized at 1/2 for a particular rotor speed<sup>1</sup> by making  $\Gamma$  equal unity; so power is maximized as well. This power is referred to as the *peak power*. The tip speed where this peak occurs is primarily dependent on the effective rotor conductivity and will henceforth be referred to as the *peak speed*. Peak speed is *not* the speed of maximum torque. The physical mechanisms behind these characteristics will be discussed in Section A.3.4.1.

Suppose now that the proper rotor conductivity and the proper electrical frequency are known. These values are listed in Table A.3.1. Then, the torque and power as functions of tip speed  $v_{tip}$  can be plotted as shown in Figure A.3.2. The shape of the torque curve is entirely

1. Note that unless the rotor film sheet conductivity is a function of  $r$  this is possible only at one radius.

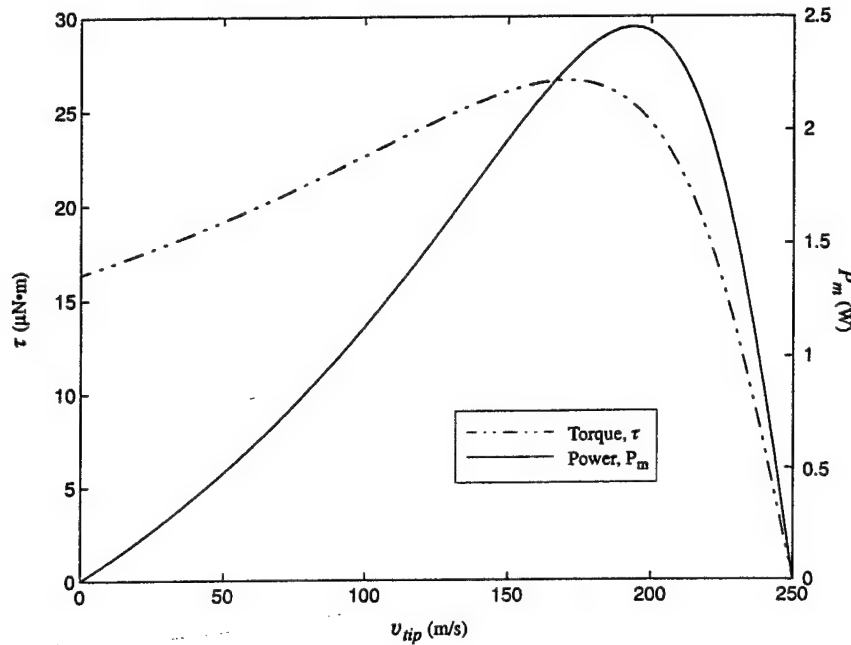


Figure A.3.2: Torque and mechanical power out of the baseline electric induction machine, plotted as a function of the rotor tip speed. Other model parameters are found in Table A.3.1.

determined by the function  $\Gamma(r)$ , while the power  $P_m$  is multiplied by the tip speed as well. The torque from Equation A.3.20 is nonzero at zero speed since  $\Gamma(r)$  there is nonzero for all  $r$ ;  $\Gamma(r)$  has an average value of 3.26 across the rotor film. However, power is zero at zero speed since the tip speed is zero. As tip speed increases, the power begins to increase as torque times the tip speed. Next, as the average  $\Gamma$  decreases through unity with increasing tip speed, the power runs through the peak power at the peak speed. Then, as  $\Gamma$  continues toward zero, the power curve heads downward approximately linearly with slip until it reaches zero at the synchronous speed. Because maximum power is not produced at the synchronous speed, induction machines are referred to as asynchronous machines.

Suppose next that every variable except rotor film conductivity is fixed, and that the film conductivity is varied. As the conductivity is increased, the peak speed shifts away from the synchronous speed. Conversely, as the conductivity is decreased, the peak speed shifts toward the synchronous speed. In both cases, the maximum torque remains constant as its curve shifts. This effect is illustrated in Figure A.3.3 and it is indicative of the similarities between an electric induction machine and a magnetic induction machine. The two machines are electromagnetic duals of one another and the rotor film in the electric machine is analogous to the rotor windings in the magnetic machine. In the magnetic induction machine, the speed at maximum torque shifts with changing rotor winding resistance, just as it does with rotor film sheet conductivity in the electric induction machine. The maximum torque does not change. Unfortunately, the peak

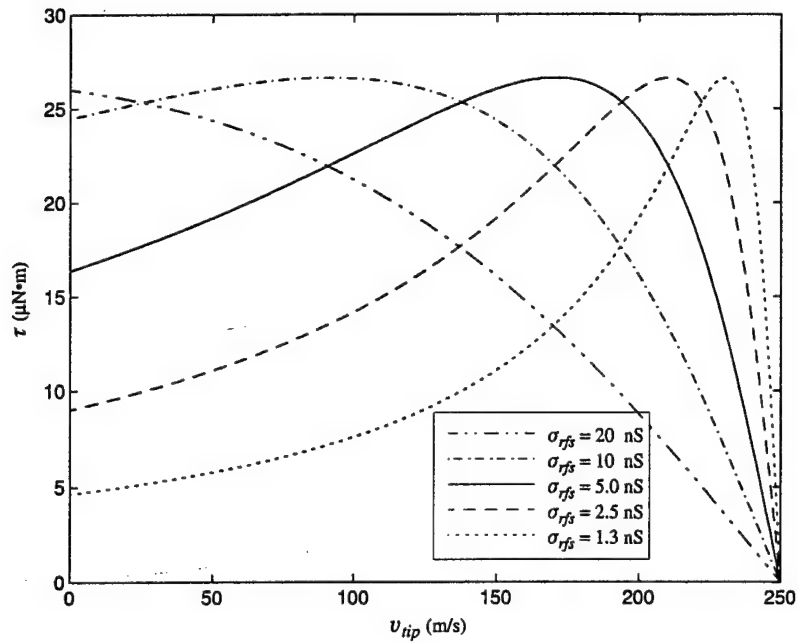


Figure A.3.3: Torque of electromagnetic origin vs. rotor tip speed plotted for several values of rotor film sheet conductivity. For each successive torque curve, the rotor film sheet-conductivity is decreased as shown in the legend. Other model parameters are found in Table A.3.1.

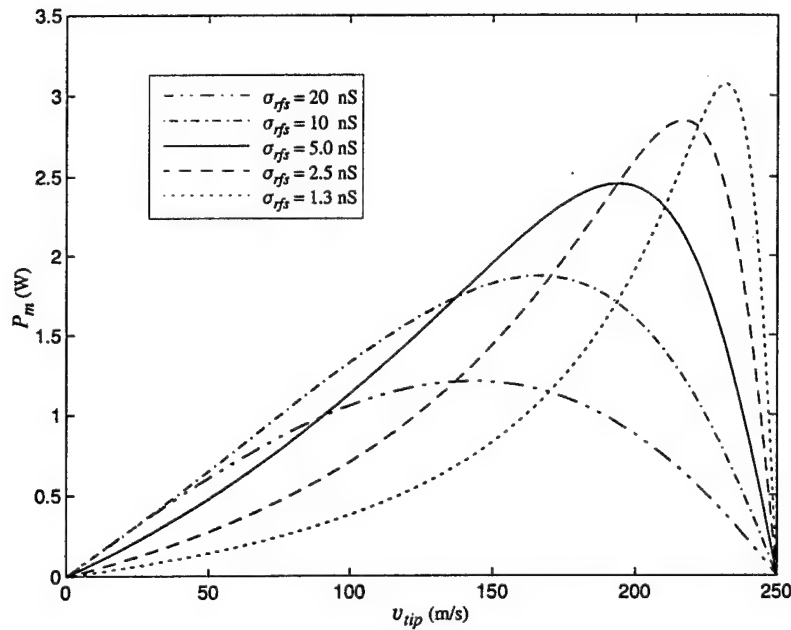


Figure A.3.4: Mechanical power out of the electric induction machine, plotted as a function of the rotor tip speed for various values of rotor film sheet conductivity. Other model parameters are found in Table A.3.1.



power does. The motor-compressor is designed with a particular power in mind; and *peak power* can change significantly as shown in Figure A.3.4. This is because of the linear dependence of power on tip speed in Equation A.3.24 as the speed of unity  $\Gamma$  changes. A change in any variable involved in the expression for  $\Gamma$  will cause a shift in peak speed, but it is primarily dependent on the rotor film conductivity.

In operation, it is possible to compensate for an increase in rotor film sheet conductivity by increasing the electrical excitation frequency to maintain a constant peak speed. For a constant periodicity, this will lower efficiency while increasing the synchronous tip speed and increasing slip toward unity. It must be remembered, however, that accurately changing the electrical frequency during operation requires both a knowledge of the as-fabricated rotor film sheet conductivity and its variance in the operation environment, as well as power electronics with frequency control. It should be noted that the actual operating tip speed would be set by the point at which the mechanical load line of the host turbomachinery crosses the power curve in Figure A.3.2. In the baseline design of the motor-compressor, this point is just above the peak speed in that figure. Note that the results show a performance increase for slightly higher rotor film sheet conductivities. However, the precise rotor tip speed during motor-compressor operation cannot be found from the results presented here, so the conductivity was chosen here to give a wide range of high power while sacrificing the peak value only slightly.

#### A.3.3.2 Trends in Periodicity and Rotor Insulator Thickness

For changes in periodicity or rotor insulator thickness, the peak speed need not change drastically but both maximum torque and peak power will. This change cannot always be remedied by a shift in electrical excitation frequency. Such changes are not a problem during operation since periodicity and rotor insulator thickness are set during fabrication. Rather, the trends help in the design of the device. The peak power is of primary interest, and it is especially sensitive to changes in the rotor insulator thickness  $\Delta_{ri}$  and the periodicity  $m$ . Parenthetically, the peak speed is especially sensitive to changes in the rotor film sheet conductivity  $\sigma_{fs}$ , as mentioned above, as well as changes in the periodicity  $m$ . The peak speed will shift approximately linearly with  $\sigma_{fs}$  and approximately inversely with  $m$  according to Equation A.3.8 and a different periodicity will suggest a different excitation frequency as will be shown below. Further, a simple inspection of Term 3 suggests that peak power will increase linearly with  $m$ .

Still, the most notable trend comes from changes in the rotor film thickness  $\Delta_{ri}$ . As the thickness  $\Delta_{ri}$  is increased, the fields have more room to decay in the negative  $z$ -coordinate direction before reaching the rotor substrate. Thus, charge relaxation will be dominated by the low sheet conductivity of the rotor film, instead of the very high conductivity of the rotor substrate. Conversely, if a thick rotor insulator is not possible, then some loss of performance will

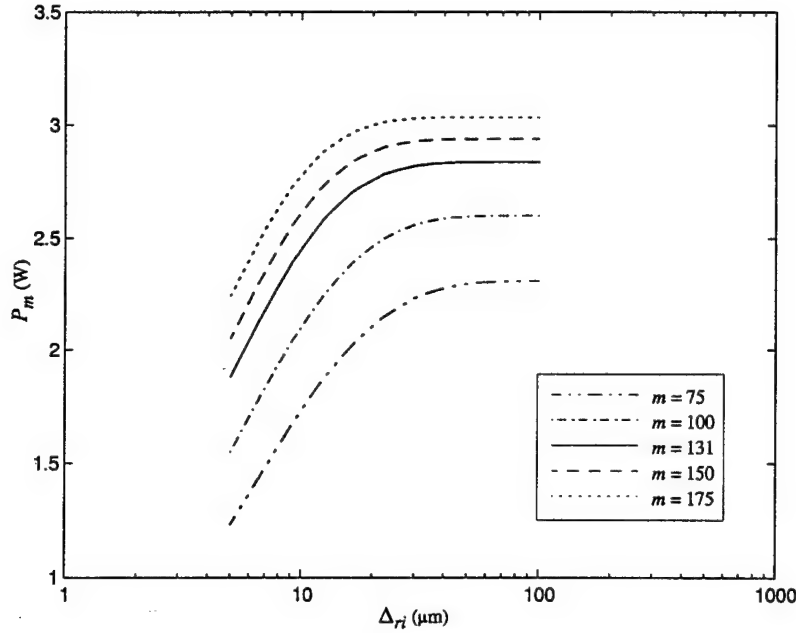


Figure A.3.5: Peak mechanical power plotted as a function of rotor insulator thickness, for several  $m$ . Other model parameters are found in Table A.3.1.

be suffered. Figure A.3.5 shows the trend in peak power as  $\Delta_{ri}$  is altered. Each line corresponds to a different value of the periodicity. The dependence of peak mechanical power on the rotor insulator thickness is entirely accounted for by Term 2 in Equation A.3.24.

On the other hand, a change in periodicity affects all three terms pointed out in Equation A.3.24. The effect from Term 1 is a shift of peak speed as mentioned above. The curves are plotted at peak speed, so the average of Term 1 across the radius will again be near 1/2 for each point on the plot. As the periodicity is varied for each curve, the electrical frequency is adjusted to maintain the same synchronous speed. As a result, the peak speed shift is slight and the tip speed outside the power integral in Equation A.3.24 remains relatively constant for every point on the curves in Figure A.3.5. Next, the effect from Term 3 is a linear shift in peak power because even for  $m = 175$ , with the remaining model parameters from Table A.3.1, the difference between the hyperbolic sine and its argument is less than 2%. Yet Figure A.3.5 shows that for any  $\Delta_{ri}$  that is in the plateau region of every curve, the peak power does not increase linearly with  $m$ . In addition, the starting thickness of consecutive plateaus decreases with increasing  $m$ . Thus, the periodicity must also have a slight effect on Term 2 so that in general the plot describes substantial, but diminishing, returns as either  $\Delta_{ri}$  or  $m$  is increased. The physical mechanisms behind these behaviors will be discussed further in Section A.3.4.2.

The increase in machine power is not without a cost when the overall electrical sub-system is considered. As the periodicity is increased, the electrical frequency must also be increased to

maintain the same synchronous tip speed  $v_{tip}^*$  since

$$\frac{f}{m} = \frac{v_{tip}^*}{2\pi R_d} \quad \text{A.3.26}$$

Synchronous tip speed largely determines the power consumption of the compressor and is held constant at its baseline value in this analysis. An increase in the electrical frequency could lead to additional losses in the external circuitry, which is made up of inductors, capacitors and transistors. A quantitative frequency limit would be based on the recovery time of the transistors and the magnitude of losses in the inductor cores.

The trade-off could go the other way as well. In the design process, the periodicity was actually pushed to near its physical limit while the synchronous tip speed was decreased to maintain a reasonable electrical frequency and limit the power draw from the compressor. Section A.4 will discuss limitations on the value of  $m$  and the reason for its baseline value.

There are also several issues which lead to an upper bound on  $\Delta_{ri}$ . The most important of these issues is the residual stress of a deposited thick film. Silicon dioxide has been chosen as the rotor film insulator simply because it is the only insulator that can be deposited as a very thick film; to date, oxide films have been deposited in thicknesses of up to 40  $\mu\text{m}$  at MIT using the Novellus Concept-One™ Plasma-Enhanced Chemical Vapor Deposition system. However, after these films were annealed, most were found to have cracked. The thickest surviving film was 10  $\mu\text{m}$  and is the basis for the baseline number presented here. Recent results suggest a possible thickness of 15  $\mu\text{m}$ , which would increase the calculated baseline peak power by 9%. Nevertheless, an even larger thickness may not be practical because the films are expected to possess a very large in-plane compressive stress, proportional to the film thickness. This stress could be large enough to prohibit wafer bonding or it could cause wafer bowing, possibly resulting in a non-uniform air gap. Therefore Figure A.3.5 is quite useful for quick estimates on how far the limits of thick film deposition should be expanded. More accurate results are given by a 3D multiple-harmonic model in Section A.4.

#### **A.3.4 Physical Mechanisms**

Behind each trend in the previous section is a specific physical mechanism. In each case, the trend can be related to a specific term or combination of terms in the power integral of Equation A.3.24. In some cases, the trend is the result of a single term. What follows is brief discussion of the way in which electromagnetic fundamentals lead to the observed trends, explained with reference to the highlighted terms in Equation A.3.24.

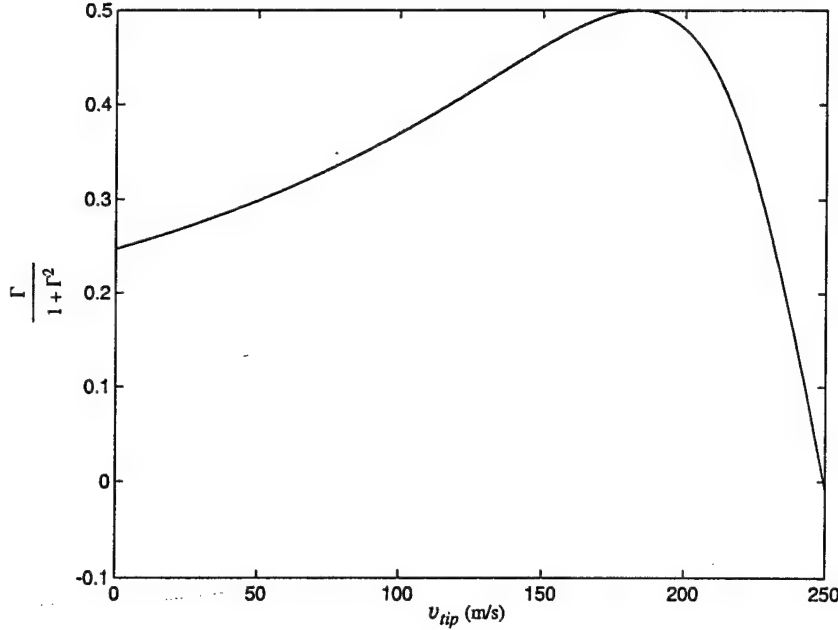


Figure A.3.6: Term 1 from Equation A.3.24 plotted as function of the rotor tip speed for a differential ring section of the rotor film, located at  $r = 5R_o/6$ . Other model parameters are found in Table A.3.1.

#### A.3.4.1 Relaxation Time

In Section A.2.2, the effective rotor relaxation time was defined within the charge conservation expression for the rotor film. It is reasonable to expect that machine performance will be maximized when this characteristic electrical time is equal to a characteristic mechanical time. The realization of this expectation is shown in Figure A.3.6 which plots Term 1 from Equation A.3.24 as a function of the rotor tip speed for the baseline value of the rotor film sheet conductivity. The peak occurs when the charge relaxation time is matched by the characteristic mechanical time, the slip time from Equation A.2.16. To remove the dependence on radius, Term 1 is considered only at  $r = R_c = 5R_o/6$ , the centroidal location of the torque density. This is done because only at a particular radius can  $\Gamma$  be made equal to unity with a uniform  $\sigma_{rfs}$ . All other things being equal, setting  $\sigma_{rfs}$  sets the characteristic electrical time.

The shape of the curve in Figure A.3.6 can be explained in terms of the two characteristic times. At synchronous tip speed, the stator potential wave travels at exactly the same speed as the rotor. Thus, image charges which are induced on the rotor film have time to relax to a distribution directly under that of their image charges on the stator. Therefore no tangential electric field develops and there is no torque. As one moves away from synchronous speed towards zero speed and the rotor slows, the charges on the rotor film do not have time to relax directly underneath the stator image charges. Instead, the charges still conduct through the rotor film at exactly the same

speed as the stator potential wave, but they now lag their image charges slightly and a tangential electric field develops to produce torque. As the rotor slows more and the charges lag further behind, the torque increases to its maximum when  $\Gamma = 1$  and the characteristic times are equal. However, the charge distribution needs time to develop on the rotor film while conducting through it. Thus, as the difference in speed between the stator potential wave and the rotor grows, the charge distribution on the rotor film becomes less developed and the torque falls off towards the zero-speed value, the starting torque.

A similar argument with respect to the rotor film sheet conductivity explains the shift in peak speed seen in Figure A.3.4. This time, consider a constant tip speed of 200m/s on the power plot of Figure A.3.3. This is the peak speed for the baseline motor-compressor design. Now, as the rotor film sheet conductivity is increased, charges on the rotor film can more easily conduct through the film. Therefore, they do not lag as far behind their stator image charges and the machine produces less power. To correct for this, either the machine would need to slow down, or the electrical frequency would need to increase. On the other hand, if the conductivity decreases, the relaxation time increases. Therefore the charge distribution cannot properly develop, and again, the machine produces less power. To correct for this, the rotor would have to speed up or the electrical frequency would be increased.

Furthermore, it should be made clear that the relaxation time depends on the effective permittivity as well. From Equation A.3.11, the dependence is the exact inverse of that for conductivity. A peak speed shift due to a percentage change in permittivity is similar to that due to a percentage change in conductivity. Specifically, the peak speed will shift by the same amount in the opposite direction. However, materials of choice permittivity are not as available as those of choice conductivity, so conductivity is the variable of choice.

Finally, for a uniform rotor film sheet conductivity,  $\Gamma$  can be made equal to unity only at a single radius. To maintain a unity  $\Gamma$  across the entire annulus of the micro-scale electric induction machine, the rotor film sheet conductivity would have to vary radially. This could be done for only one electrical frequency and tip speed. A graded conductivity is not outside the realm of fabrication possibilities, but the benefits may not out-weigh the costs. Simulations show that for the baseline design of Table A.3.1 the difference between a uniform and graded rotor conductivity is a 16% increase in power. However, a graded rotor film sheet conductivity is estimated to increase fabrication complexity by much more than 16%. So for now the rotor film sheet conductivity will be uniform and the performance of the machine will be increased by other more attainable means, perhaps by increasing the rotor insulator thickness.

#### A.3.4.2 Electric Field Penetration

The thickness of the rotor insulator is important for one reason: an electrical short through

the rotor substrate leads to drastically decreased performance. When the substrate is perfectly conducting it acts as a perfect short in the charge relaxation loop around the rotor. This causes the rotor to appear more conductive since its conductivity becomes dominated by the rotor substrate. A decrease in rotor film sheet conductivity cannot compensate for the short. If, on the other hand, the substrate is perfectly insulating, then the rotor conductivity is dominated by the rotor film. This is the preferred situation. It is possible for the substrate to be slightly conducting, like the rotor film. In this case, the effective rotor conductivity in Equation A.3.12 would include some fraction of the rotor substrate conductivity. Because of the constraints on available materials discussed in Section A.2, this is not specifically relevant.

Recall that a potential is enforced on the stator electrodes of the induction machine as shown in Figure A.3.1 or Figure A.2.1. The electric field associated with this potential penetrates into the rotor insulator and essentially dies off exponentially through its thickness. Referring to the circumferential slice of the last section, the decay length of the electric field is

$$\frac{1}{k} \rightarrow \frac{r}{m} = \frac{R_c}{m}.$$

Within three decay lengths, the field will have died off to very near zero. If it does not die off before reaching the rotor substrate, then the field “sees” the substrate and is shorted out to some degree. Additional charges will be induced at the interface of the rotor insulator and the rotor substrate, the relaxation time in the rotor substrate will be zero, and the charges will have no resistance to conduction. In addition, less charge will be induced at the rotor film because the field has been shorted. Therefore machine torque will be compromised overall.

To give the fields enough room to die off, the rotor insulator should be made thick enough such that peak power lies on one of the plateaus in Figure A.3.5. The trend is explored further in Figure A.3.7 where Term 2 has been plotted against the rotor insulator thickness  $\Delta_{ri}$  for several values of the periodicity  $m$ , at the centroidal radius. As the periodicity is decreased, and the decay length is increased, the term begins to plateau only at increasingly larger rotor insulator thicknesses. This follows from the discussion of the last paragraph. As an aside, note that Term 1 will also change as a function of  $\Delta_{ri}$ , but this causes only a slight shift in the peak speed. Thus, if Term 1 is maximized the peak power is a function of  $\Delta_{ri}$  only through Term 2.

#### A.3.4.3 Periodicity and Air Gap Length

Term 2 can also be viewed in another way. This view will explain why the plateaus become lower for higher periodicity. Term 2 combines the effects of penetration to the rotor substrate, which has been explained, with the effects of field decay across the air gap and the resultant fringing between neighboring charge poles at the stator. In general, the machine will have better

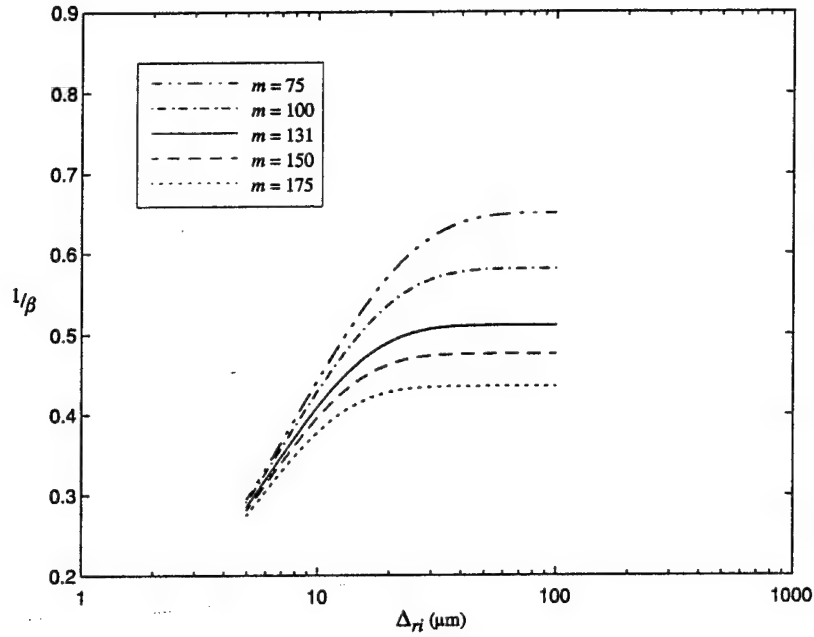


Figure A.3.7: Term 2 of Equation A.3.24 plotted as a function of the rotor insulator thickness  $\Delta_{ri}$  for several values of the periodicity  $m$ . This plot shows the effect of field penetration to the rotor substrate. Other model parameters are found in Table A.3.1.

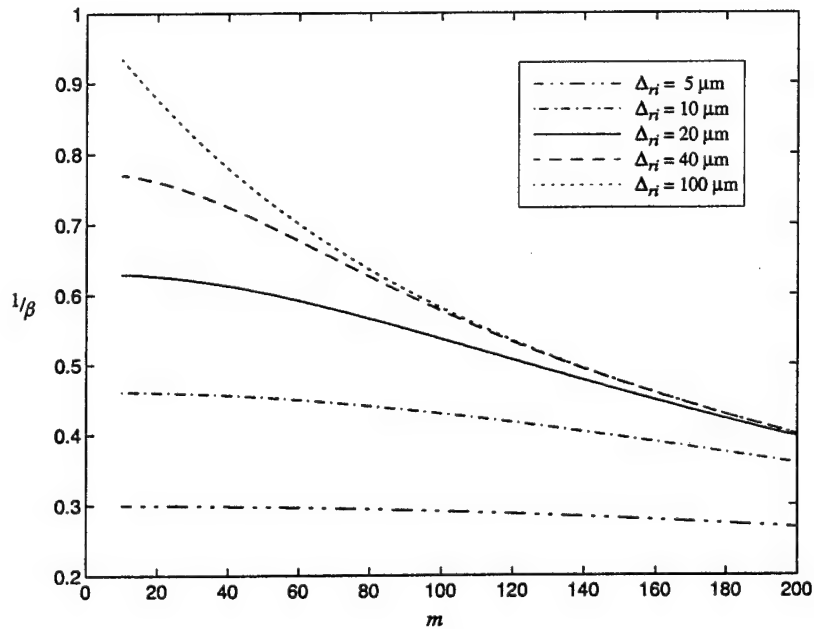


Figure A.3.8: Term 2 of Equation A.3.24 plotted as a function of the periodicity  $m$  for several values of the rotor insulator thickness  $\Delta_{ri}$ . This plot shows the effect of field fringing at the stator. Other model parameters are found in Table A.3.1.



performance when the field in the air gap is greatest. Therefore, when the insulator thickness is large enough so that Term 2 is on a plateau, performance suffers because fringing increases at the stator. The effects of fringing are illustrated by a graph of Term 2 versus the periodicity  $m$  in Figure A.3.8.

-Fortunately, the linear dependence of Term 3 on  $m$  more than counteracts the effect of Term 2. The combined effects of all three terms, as functions of both  $\Delta_{ri}$  and  $m$ , are summed up in Figure A.3.5. Thus, as periodicity is increased, the peak power increases linearly until excessive fringing occurs. Then the linear increase becomes noticeably offset because of the division by  $\beta$ , shown in Figure A.3.8.

The trend in periodicity does not suggest a decrease in the periodicity; rather, it suggests a decrease in the gap  $G$ . The trend of Term 2 for a percentage change in the gap length  $G$  is precisely the same as the trend for a percentage change in  $m$ . However, changes in the air gap have their own advantages and disadvantages. It is readily apparent from Equation A.3.24 that decreasing the air gap length will increase the mechanical power supplied by the induction motor with the inverse of the gap. At the same time, decreasing  $G$  helps to reduce fringing. Unfortunately, a decrease in the air gap results in an increase in power dissipation from viscous drag of the air within the gap. This power dissipation actually scales with the inverse *square* of the air gap length. As this fact suggests, the baseline design presented here is the result of many compromises between the electrical and mechanical designs of the complete motor-compressor system. Additional outcomes from changes in the air gap length are discussed in Section A.4.3.1. The most significant of those is a limit on the maximum electric field in the gap as  $G$  is decreased.

### **A.3.5 Summary**

Within the constraints outlined in Section A.3.1, the 2D single-harmonic model developed in Section A.2 is transformed to provide a more accurate 3D single-harmonic model. This section has striven to explain this model and its assumptions in detail. The 3D single-harmonic model provides the foundation for a more detailed model to be discussed in the following section. It has been shown that in general, one would like a micro-scale electric induction machine to have a very thick rotor insulator and a very high periodicity, within the bounds of electrical excitation frequency. The same conclusions are derived in the following section and much more accurate results are obtained.

## **A.4 The 3D Multiple-Harmonic Model**

If it were possible to construct an electric induction machine with an infinite number of electrodes, then further work would only refine the 3D single-harmonic model. Unfortunately, an infinite number cannot be implemented, so this section develops the 3D multiple-harmonic



model. It's main contribution over the 3D single-harmonic model is that it accounts for the finite number of electrodes. Therefore, the multiple-harmonic model accounts for all four major characteristics outlined in the Introduction.

#### **A.4.1 Stator Electrodes: Fabrication and Breakdown Strength**

The stator potential waveform is applied by a finite number of electrodes with insulating space between them. The voltage will be constant across the surface of each electrode and follow a smoothly varying function along the insulating space between one electrode and the next where point it will be constant over the surface of that electrode. The cycle continues while overall describing a discretely sampled sine function. Thus, no matter how each electrode is excited in time, a perfect sine wave cannot actually be enforced around the circumference of the stator electrodes as assumed in the 3D single-harmonic model. Instead, the traveling sine wave will be sampled several times over each spatial wavelength as shown in Figure A.4.1. As the figure shows, there are six electrodes per spatial wavelength in the baseline design.

The number of electrodes per wavelength is referred to here as the number of phases. Since the periodicity  $m$  is the number of wavelengths enforced around the entire circumference of the stator, the total number of electrodes is given by

$$N_e = N_p m \quad \text{A.4.1}$$

where  $N_p$  is the number of phases.

The number of phases is decided through a combination of two issues: concerns over electrical breakdown between the electrodes and goals for the stator waveform potential amplitude. The first issue arises because neighboring electrodes are usually at two different potentials as in Figure A.4.1. The breakdown voltage is defined as the difference in potentials that will cause electron avalanche breakdown to occur between the electrodes. For DC voltages, this phenomenon has been studied in detail. One seminal experimental result is a curve from Paschen

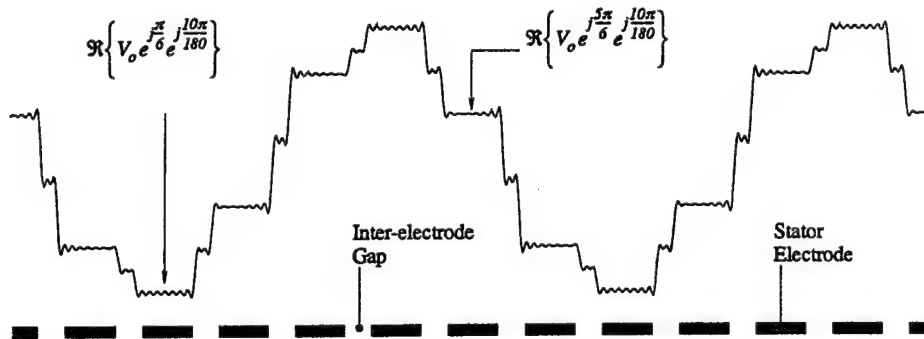


Figure A.4.1: Two spatial wavelengths of the stator potential at an instant in time and at the outer radius of the machine. The potential across each inter-electrode gap is conservatively assumed to be the average of the electrode voltages on either side of the gap.

[5] which gives the breakdown voltage as a function of the separation between two spherical electrodes. This voltage is shown to be greater than 300 V for any separation between smooth electrodes until the fields become so high that field emission occurs. Since the electric induction machine is an AC machine and breakdown voltage is very sensitive to geometry, experiments are underway to extend the results of Paschen and others to the case of rectangular electrodes excited with AC voltages. Nevertheless, the existing results have been used to define the maximum safe voltage differential between the electrodes of the baseline motor-compressor as 300 V.

The second issue is related to the first because the goal for the excitation voltage is also based on Paschen's curve but its implementation requires a certain number of phases. The excitation voltage, or the stator potential waveform amplitude, is also the maximum potential difference across the air gap and it is set to the safe limit of 300 V as well. This means that the potential of each electrode, independent of the number of phases, will vary from +300 V to -300 V over one cycle *in time*. However, since the excitation of spatially consecutive electrodes is phase-shifted in time, the potential difference between any electrode and the next could actually be greater than 300 V. This difference depends on the number of phases and it can be shown that a phase-shift of  $60^\circ$  or less will ensure that the potential difference will never exceed 300 V. A  $60^\circ$  phase-shift requires six electrodes per wavelength; i.e., the number of phases  $N_p = 6$ . A greater number of phases would reduce the potential difference between electrodes even more and better approximate a perfect sine wave; but for more than six phases, independent excitation of each phase and connection of the electrodes within each phase might be more trouble than it is worth. This opinion is explained at the end of Section A.4.2.2 below. The electric induction machine modeled in this section is therefore a 300-V, six-phase machine with a correspondingly limited number of electrodes.

This number is limited by available space at the inner radius of the stator. The electrodes are constrained to a minimum width and there is a minimum inter-electrode gap which must exist between them. Micro fabrication techniques impose a lower limit on the electrode width and the breakdown strength of air imposes a lower limit on the minimum inter-electrode insulator width. The number of electrodes is then limited by the number of electrode-insulator pairs that fit on the inner circumference of the stator. This circumference is the same as that of the inner radius of the rotor film. These limitations dictate an electrode topology much like that shown in Figure A.1.1. In the interest of clarity, the picture shows only 20 electrodes while there are actually 786 in the baseline design.

Each width constraint can be considered separately. First, the minimum electrode width, more generally referred to as the minimum line width, is limited by fabrication constraints. The fabrication constraints are very dependent on the available equipment, repeatability and required process development time. The large overall size of the motor-compressor and a team decision on

the desired level of complexity for the baseline fabrication process were used to set the minimum line width at 4  $\mu\text{m}$ .

The second constraint again concerns the potential difference between phases. Having decided upon the number of phases, the maximum potential difference between neighboring electrodes is known for a given excitation. Therefore, the width of the inter-electrode insulator determines the maximum electric field in that insulating space. The electric field is the real motivator of the limit on breakdown voltage discussed above and when discussed in terms of the field in a gap, the measure is called the breakdown strength. Relevant experimental results for micro-scale devices [4] have shown that fields on the order of  $1\text{--}3 \times 10^8$  V/m can be withstood in an air-filled gap, with either DC or AC applied voltages. For macro-scale devices, the breakdown strength of air is around  $1 \times 10^6$  V/m. This is why there are no macro-scale electrostatic motors in wide use. To be safe, the baseline motor-compressor is designed for a maximum electric field of  $1 \times 10^8$  V/m. The inter-electrode gap is then set to 4  $\mu\text{m}$  to account for unforeseen geometrical non-uniformities.

**Table A.4.1** Baseline values for the extra model parameters used in the 3D multiple-harmonic model.

Parameters	Value in Baseline Design	Comments.
$G_{ee}$	4 $\mu\text{m}$	Inter-electrode insulating gap width.
$N_e$	786	Number of electrodes.
$N_p$	6	Number of phases (electrodes per spatial wavelength).
$m$	131	Baseline stator waveform periodicity.
$N$	41	Number of Fourier harmonics considered in sum. The number used is less since the trivial harmonics are discarded.

The stator electrode design is the result of many related concerns and has two main consequences. In summary, the electrode width is limited by fabrication constraints and the inter-electrode gap is limited by the breakdown strength of air. Then the number of phases is similarly limited by the breakdown strength of air so that the maximum number of electrodes is limited by available space at the inner radius of the stator. Now, by Equation A.4.1 the maximum periodicity listed in Table A.3.1 is determined from the electrode design. This is the first consequence of the electrode design. The second is that the step-wise discontinuous stator voltage waveform must be accounted for in the model. This is done by combining several harmonics from the 3D single-harmonic model to produce the 3D multiple-harmonic model. Table A.4.1 provides a summary of the extra parameters required by the 3D multiple-harmonic model in addition to those in Table A.3.1.

## A.4.2 Fourier Decomposition and Recombination

### A.4.2.1 Spatial Fourier Decomposition of the Stator Electrode Voltage

The purpose of the 3D multiple-harmonic model is to account for the discretely varying nature of the waveform that is enforced on the stator by a realistic stator electrode model as shown in Figure A.4.1. The assumed step-wise discontinuous stator potential function is decomposed into a number of potential harmonics. Each harmonic is characterized by a single spatial period while its amplitude is obtained by scaling the stator potential amplitude according to a complex Fourier weight. A certain number  $N$  of the spatial potential harmonics are summed at each point in space to yield the approximate stator waveform shown in Figure A.4.1. The Fourier weights are complex numbers so as to represent the temporal phase difference between neighboring electrodes; therefore the result of the sum is also a complex number. The figure plots the real part of the waveform at an instant in time and at the outer radius of the stator electrodes.

The modeled stator potential waveform is only as accurate as the assumed potential on which it is based. For a time-varying solution, even one for steady state, it is a complex and time-consuming operation to fully describe the spatial variation of the potential across the inter-electrode insulator. The difficulty arises because of the spatially discrete nature of the electrodes. A specific potential can only be enforced on the electrode surfaces. The potential across the inter-electrode insulator will assume a function which depends greatly on the thickness of the electrodes and the condition of the insulator surface. For electrodes which are thicker than the width of the inter-electrode insulator when the insulator is clean and smooth, this function will be very nearly linear. The function will be similar for very thin electrodes with a dirty and thus slightly conducting insulator in between them. This could be the case if the stator insulator became contaminated with adsorbed combustion products or dust particles. However, if the surface is clean and the electrodes are thin, the potential function across the inter-electrode insulator could be more complex. Specifically, if the neighboring electrodes are further apart than they are thick, the function will begin at the potential of one electrode and then follow a hyperbolic sine to the average potential of the two neighboring electrodes at the middle of the inter-electrode insulator. Nearing the next electrode, the function will then follow another hyperbolic sine shape to the potential of that electrode. The extent of the hyperbolic sine shape depends upon the thickness of the electrode to first order. If the inter-electrode insulator is several times wider than the electrodes are thick, the extent of the hyperbolic function will be negligible and the potential across the insulator can be approximated as the average of the two neighboring electrodes. As a further complication, if there is a ground plane in the vicinity of the electrodes, the potential function across the inter-electrode insulator could dip (or rise) smoothly towards the ground potential near the middle of the insulator before resuming its approach toward the potential of the next electrode. The effects on peak power of three different potential functions

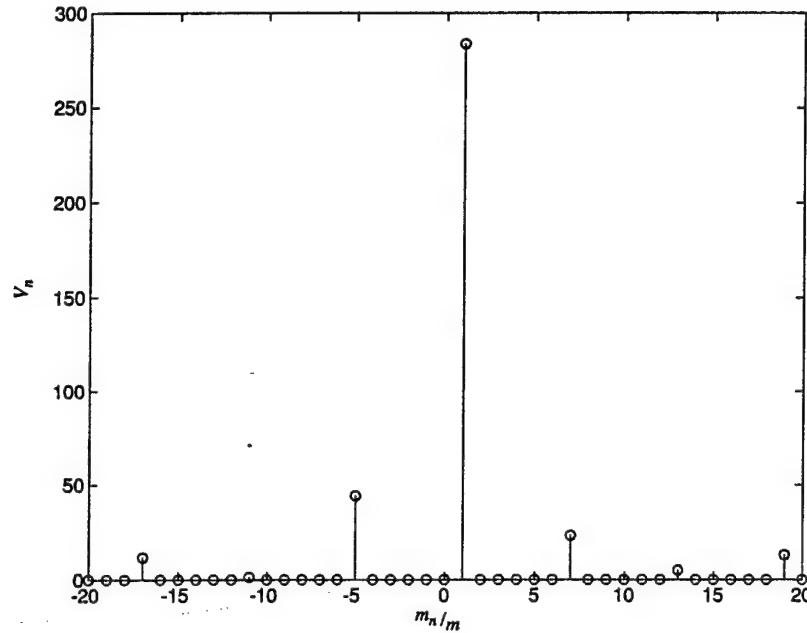


Figure A.4.2: The magnitude of the complex-valued potential harmonics which make up the waveform in Figure A.4.1 given a 300 V amplitude. The ordinate shows the index of each harmonic as the harmonic periodicity  $m_n$  divided by the fundamental periodicity  $m$ . A positive index denotes a forward traveling wave, while a negative index denotes a backward traveling wave. The index of the DC component is zero, thus the DC harmonic has no periodicity and is constant in space. These represent the total number of harmonics used for the results of the 3D multiple-harmonic model presented in this appendix.

across the inter-electrode insulator—a linear potential, an average potential, and a zero potential—are described in Section A.4.3.2.

In the real micro-scale electric induction machine, the potential function across the inter-electrode gap will lie somewhere between the linear and average cases above since the nearest ground plane is several inter-electrode insulator widths away. Furthermore, the ratio of inter-electrode insulator width to electrode height is 4:1 in the baseline design, so the function is closer to the average case. Thus, as a somewhat conservative approximation, the results presented throughout this section will all assume a time-harmonic and spatially constant average potential across the inter-electrode insulator. Therefore, the modeled stator potential function is just as shown in Figure A.4.1.

The pictured waveform shows the real part of the potential at the normalized time of  $\omega t = 10\pi/180$  while the potential is mathematically described as a complex number to account for the constant  $60^\circ$  temporal phase shift between neighboring electrodes. Complex Fourier weights computed from this complex potential then contain both spatial and temporal information for the waveform. The 2D and 3D single-harmonic models both give steady-state solutions in time, thus the 3D multiple-harmonic model also gives a steady state solution. Each electrode potential oscillates at the same frequency in time, but the temporal phase difference between neighboring

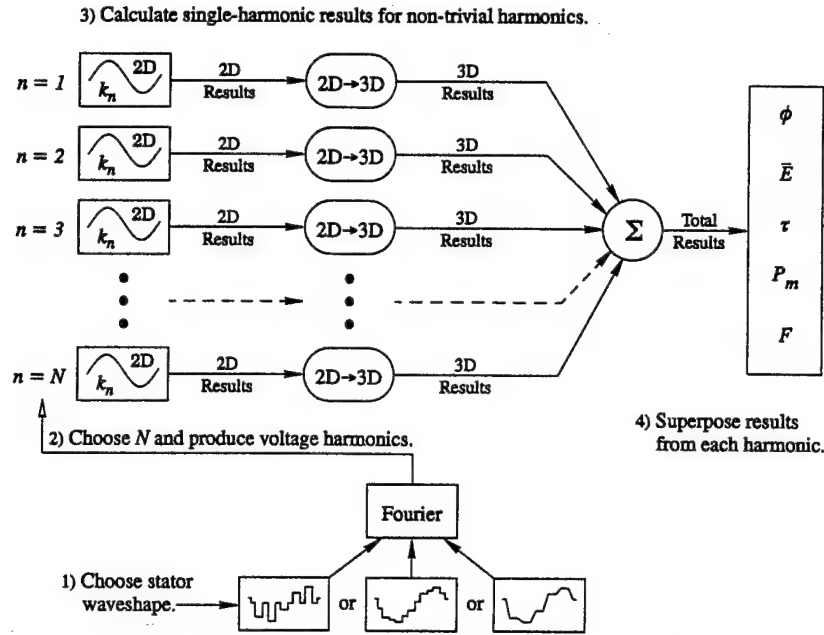


Figure A.4.3: This picture shows the manner by which the 3D multiple-harmonic model uses the harmonic content of the discretely sampled stator waveform to find the total electric potential, fields, torque, mechanical power and pull-in force as sums of 3D single-harmonic models that were transformed from 2D single-harmonic models.

electrodes causes the step-wise sinusoidal waveform to appear to advance around the stator.

The wave consists of both forward and backward traveling components which may be distinguished by their individual periodicities. If the assumed potential wave is decomposed into 41 components, for example, there will be 20 forward traveling waves, 20 backward traveling waves, and one component which is constant in time, a so-called DC component. Each of the forward components will have a periodicity which is a multiple of the baseline periodicity  $m = 131$ . The backward traveling components will have the same periodicities with the opposite sign. The magnitudes of the complex potential amplitudes of each spatial harmonic of stator potential, using the baseline design, are plotted in Figure A.4.2 versus the corresponding multiple of the baseline periodicity. Notice the dominance of the first forward component.

#### A.4.2.2 Fourier Recombination of Single-harmonic Solutions

Since Laplace's equation is a linear partial differential equation, each component of the stator potential waveform produces a linearly independent electrical response. These responses may be superposed to find the total electric potential, field and charge within the machine due to the total stator potential waveform. Further, since the torque produced by the machine is an integrated product of electric field and charge, both of which are assembled from orthogonal Fourier components, the torque from the individual Fourier components may be superposed to find the total torque. The process is described schematically in Figure A.4.3. First the stator voltage is defined and decomposed into an appropriate number of Fourier harmonics as described

above. Then, the 2D single-harmonic model analysis for each non-zero harmonic is transformed to a 3D single-harmonic model analysis as described in Section A.3.1 to determine the electric potential, fields, torque, pull-in force and power for each harmonic. Finally, the contributions from each harmonic are summed to yield the total potential, field, torque, pull-in force, and power for the total stator potential excitation waveform as the one shown in Figure A.4.1.

As a very good approximation, only the fundamental harmonic contributes to the sum when power is the desired result. Since the higher harmonics have higher periodicities, these harmonics have lower synchronous speeds for a fixed temporal frequency. For example, the first non-trivial forward harmonic above the fundamental has a periodicity of  $7m$  and a corresponding synchronous speed of 35.7 m/s. Similarly, the synchronous speed of the first non-trivial backward traveling harmonic is negative 50 m/s. In addition, Figure A.4.2 shows that the potential magnitude of these harmonics is a small fraction of the fundamental amplitude. Thus, according to Equation A.3.24, the power from these harmonics is an even smaller fraction of the power from the fundamental. The results presented below include all non-trivial harmonics, but noting the dominance of the fundamental is often useful for quick answers from the results of Section A.3. Note that the fundamental potential magnitude is very near 300 V. Although power scales with the square of this potential, an increase in its value is not necessarily warranted. The increase could come from the incorporation of a higher number of phases. This would decrease the periodicity and increase the complexity of the inter-phase connections in the device, leading to performance decreases.

#### **A.4.3 Torque, Power and Pull-in Force from the 3D Multiple-Harmonic Model**

This section presents results from the 3D multiple-harmonic model. The results describe trends that are similar to those found using the 3D single-harmonic model. This is to be expected because the fundamental harmonic dominates the torque and power as described in the last section. The model parameters are still as listed in Table A.3.1 with additional parameters used in the multiple-harmonic model as listed in Table A.4.1.

To produce the total mechanical power curve in Figure A.4.5, the power harmonics of Figure A.4.4 are summed, giving the total mechanical power. The total torque curve is also shown. They both closely resemble those of Figure A.3.2 since the contribution of the fundamental harmonic dominates. The same definitions for these totals are adopted here: peak power is the maximum power from the power curve and peak speed is the rotor tip speed at which peak power is obtained. In addition to trends for mechanical power, this section presents trends for the pull-in force, which is also plotted in Figure A.4.5. This is an unavoidable force which tends to pull the rotor in the axial direction towards the stator at all rotor tip speeds. It is counteracted by the aft thrust bearing, which is designed to provide the stiffness necessary to maintain the air gap length



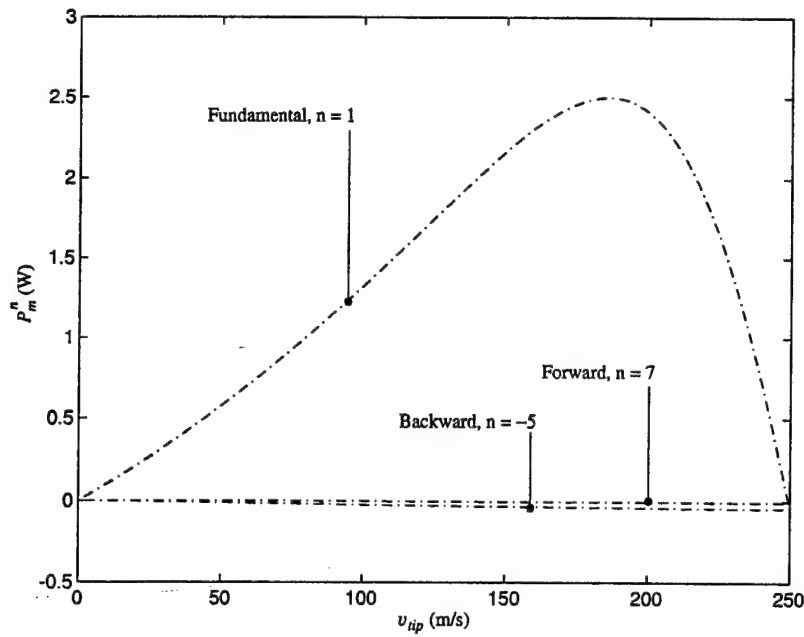


Figure A.4.4: Power harmonics vs. rotor tip speed for the baseline design. Several harmonics are labeled with their index  $n$  in the Fourier sum. Other model parameters are found in Table A.3.1 and Table A.4.1.

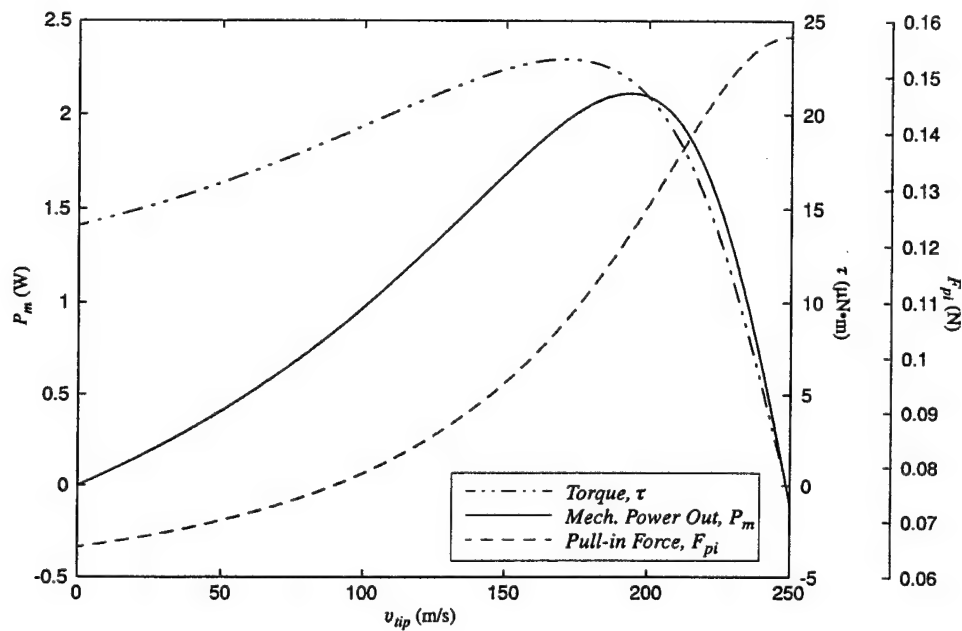


Figure A.4.5: Total mechanical power out, torque, and pull-in force vs. rotor tip speed. Other model parameters are found in Table A.3.1 and Table A.4.1.



to within less than 10% of its baseline value. The term *peak force* will refer to the pull-in force at peak speed, while *maximum force* will refer to the force at synchronous speed.

#### A.4.3.1 Trends from the 3D Multiple-harmonic Model

Several power curves like those in Figure A.4.5 are plotted in Figure A.4.6 for different values of the rotor insulator thickness. The peak power from each curve is found and plotted in Figure A.4.7 as a function of the rotor insulator thickness, showing that this trend for the 3D multiple-harmonic model is exactly the same as that from the 3D single-harmonic model. To highlight this fact, Figure A.4.7 also shows the result from the single-harmonic model based on the fundamental harmonic. In addition, the figure shows the result when the rotor film conductivity is graded to maintain unity  $\Gamma$  across its radius. As mentioned in Section A.3.4.1, there is a 16% increase in power when this is done. This issue will become more relevant if the increase becomes more feasible. At the moment, for the baseline device, the fabrication complexity is unwarranted.

The pull-in force is plotted versus rotor tip speed for the same range of  $\Delta_{ri}$  in Figure A.4.8. Notice that the maximum force remains constant as  $\Delta_{ri}$  increases, whereas Figure A.4.9 shows that the *peak force* decreases. This means that if the rotor spins at or near the peak speed, the operating point pull-in force will be smaller for machines with thicker rotor insulators. Furthermore, the low speed pull-in force is decreased as the thickness is increased. Thus a thicker insulator will help during start-up since there is a possibility of rubbing friction at low speeds. The rubbing friction would be between the rotor insulator and the thrust pads and outer seal of the motor-compressor. For example, if the aft thrust bearing happens to lose its stiffness, the pull-in force will clamp the rotor against the thrust bearing pads. The height of the pads is sized mainly to control the amount of pressure over the thrust bearings, but the pads also provide a physical stop to the vertical travel of the rotor and prohibit it from touching down on the stator electrodes. Without the physical stops provided by the thrust bearings, the rotor would touch down on the electrodes and if they are charged, some electrodes could be shorted and cause a damaging electrical discharge.

Similar breakdown problems could occur across the air gap when it becomes smaller than that for which the operating voltage was designed. There are at least two factors which could give rise to a decreased air gap: an improper balance of pressure on the forward and aft thrust bearings, and micro-fabrication etch non-uniformity. These factors lead mostly to problems, but there is also one benefit. More specifically, when the air gap length is decreased the electric field in the gap increases. Unless the voltage is decreased with the gap, the first problem could be a damaging electrical discharge across the gap and failure of the device. Also, when the gap decreases the pull-in force increases with the inverse of the gap, so this is a non-linear and

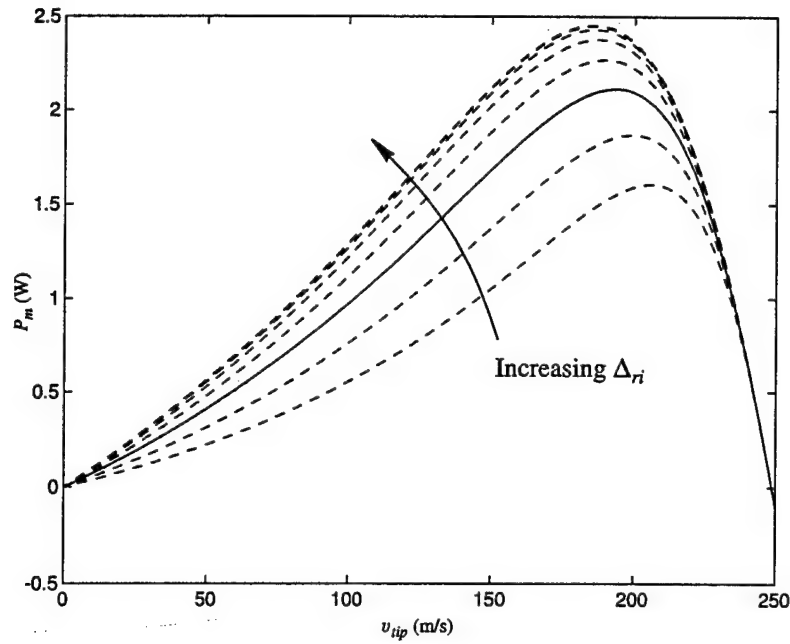


Figure A.4.6: Mechanical power out vs. rotor tip speed for several values of the rotor insulator thickness. The solid line is the case  $\Delta_{ri} = 10 \mu\text{m}$ . Other model parameters are found in Table A.3.1 and Table A.4.1.

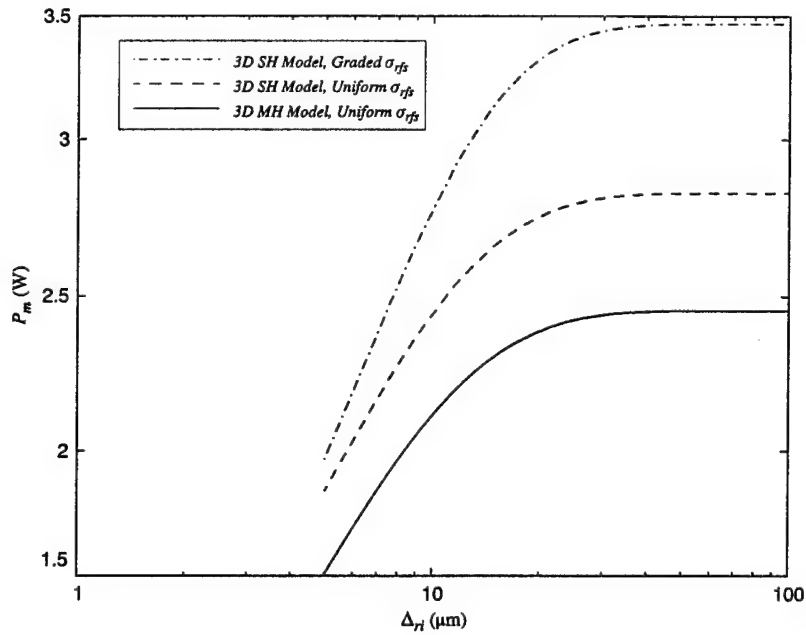


Figure A.4.7: Peak mechanical power vs. the rotor insulator thickness. The solid line is from the 3D multiple-harmonic model. The plot also shows two curves from the 3D single-harmonic model: one for a uniform conductivity across the rotor film and one for the case when the conductivity is graded to maintain unity  $\Gamma$  across the radius of the rotor film. For  $\Delta_{ri} = 10 \mu\text{m}$ , the difference is about 16% more power. See the end of Section A.3.4.1. Other model parameters are found in Table A.3.1 and Table A.4.1.

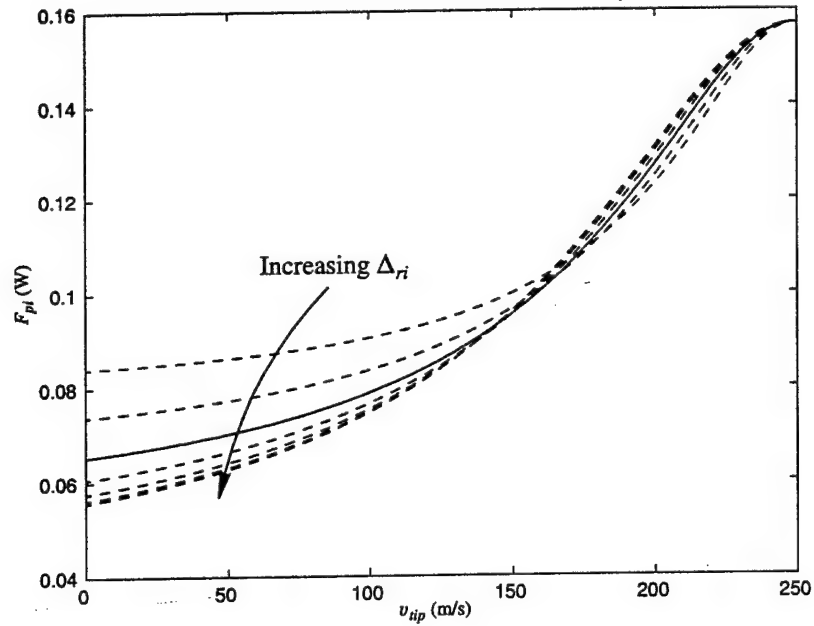


Figure A.4.8: Pull-in force vs. rotor tip speed for several values of the rotor insulator thickness. The solid line is the case  $\Delta_{ri} = 10 \mu\text{m}$ . Other model parameters are found in Table A.3.1 and Table A.4.1.

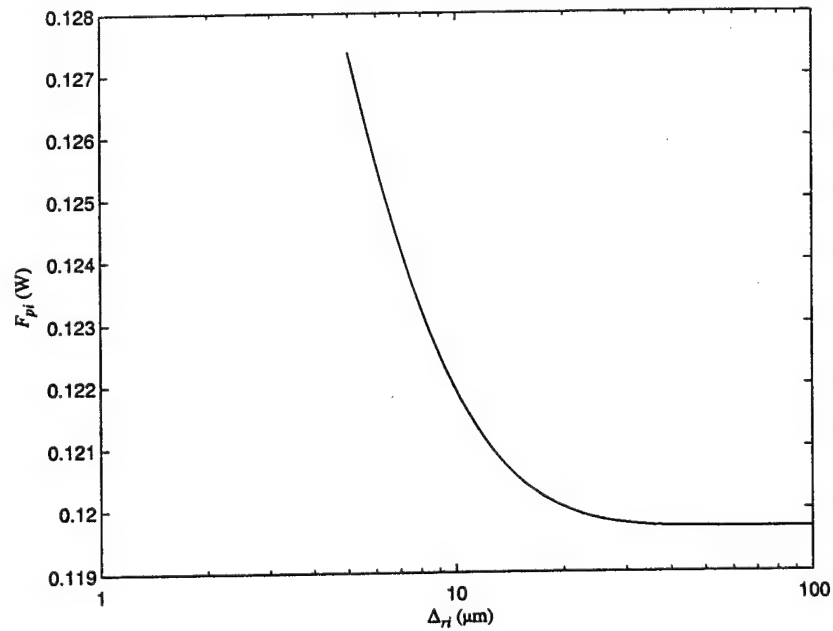


Figure A.4.9: Peak pull-in force vs. the rotor insulator thickness. Peak force is defined as the force at the point of peak power. It is not the maximum force that occurs at synchronous speed. Other model parameters are found in Table A.3.1 and Table A.4.1.

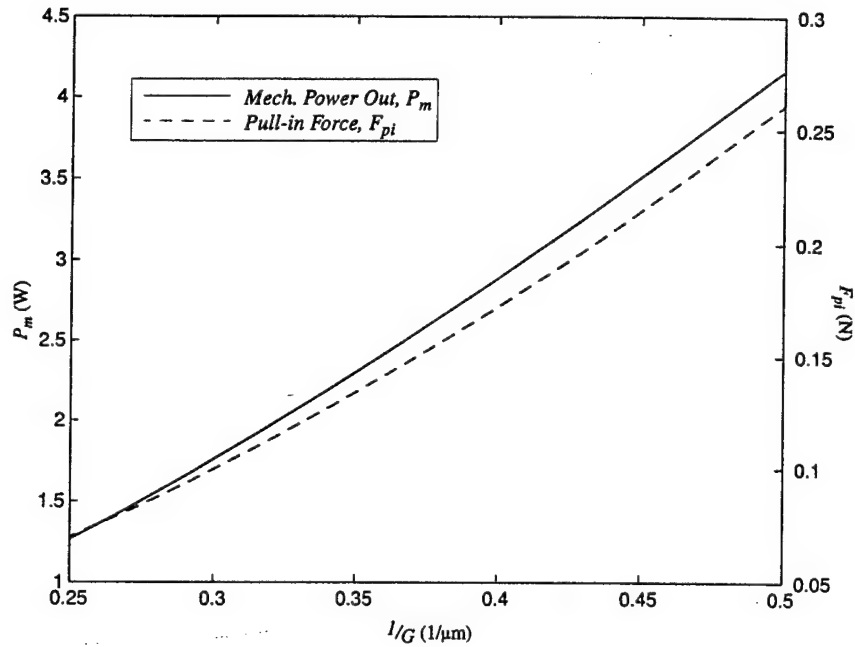


Figure A.4.10: Peak mechanical power and peak pull-in force vs. the inverse of the air gap length. Peak force is defined as the force at the point of peak power. It is not the maximum force that occurs at synchronous speed, although that force scales similarly. Other model parameters are found in Table A.3.1 and Table A.4.1.

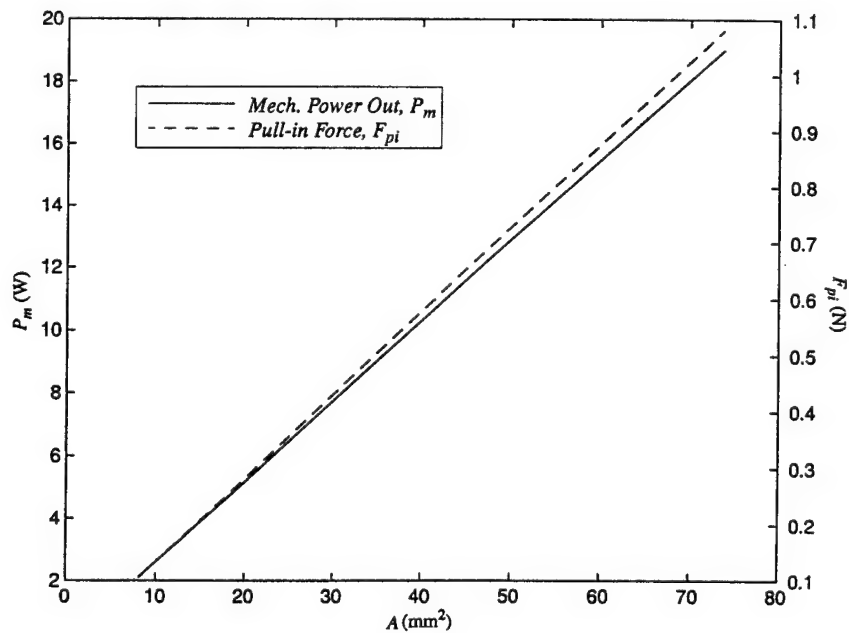


Figure A.4.11: Peak mechanical power and peak pull-in force and vs. the active area  $A$  of the electric induction motor. Machine active area is defined as the intersection of the area of the rotor film with the area of the stator electrodes. Peak force is defined as the force at the point of peak power. It is not the maximum force that occurs at synchronous speed, although that force scales similarly. Other model parameters are found in Table A.3.1 and Table A.4.1.

unstable process. Any small perturbation which closes the air gap would only increase the force and close the gap further. Thus, an adequate thrust bearing design is crucial to the success of the motor-compressor. The changes in the pull-in force when the gap is both decreased and increased are shown in Figure A.4.10, and results such as these are used to when designing the aft thrust bearing.

On the positive side, Figure A.4.10 shows that peak power also scales approximately linearly with the inverse of the gap length. Thus, if the gap is decreased and the fields and forces can be withstood, there will be an increase in mechanical power output from the electric induction motor. Note that the maximum force also increases approximately linearly with the air gap inverse.

Finally, consider the dependence of power and force on the machine's active area  $A$ . The machine active area is defined as the intersection of the area of the rotor film with the area of the stator electrodes. The method by which power and force are calculated suggests that these will simply scale linearly with the area. However, recall that the average force densities contain several terms which depend on radius and so may lead to a non-linear dependence of the power and pull-in force on area. Figure A.4.11 shows that this is not generally the case by plotting the peak power and peak force for several machines whose inner and outer radii are scaled by a multiple of the baseline size. The inner and outer rotor film and disk radii are scaled together so that the synchronous rotor tip speeds and synchronous excitation frequencies of each machine are the same. An inspection of Equation A.3.24 shows why this is so. First, Figure A.4.11 plots peak power so that Term 1 is always equal to one half. Second, Term 2 has no dependence on machine active area to first order. Third, since a larger motor allows for more electrodes at the inner radius of the stator, the periodicity is increased by the same multiple as the inner and outer radii. In Equation A.3.24 this increase is offset by the corresponding increase in  $R_d$ . Finally, the radial dependence of Term 3 becomes a linear function of area because of the integration from the inner radius to the outer radius. The same can be said of the terms in the integral for pull-in force although it is not shown in this appendix. Thus, the radial dependencies become washed out and the peak power and peak force both scale linearly with the active area of the micro-scale electric induction machine.

#### A.4.3.2 Consequences of the Inter-electrode Gap

It may be possible to reduce the viscous drag in the air gap by etching deep trenches in the inter-electrode gap. Appendix B discusses this question in detail. That appendix shows that the effectiveness of the trenches is increased if they are made as wide as possible. The trenches serve to increase the effective air gap length where fluid drag is concerned. However, an increase in the inter-electrode gap has a detrimental effect on the mechanical power output from the electric induction machine in a manner similar to the dependence on active area shown in Figure A.4.11.

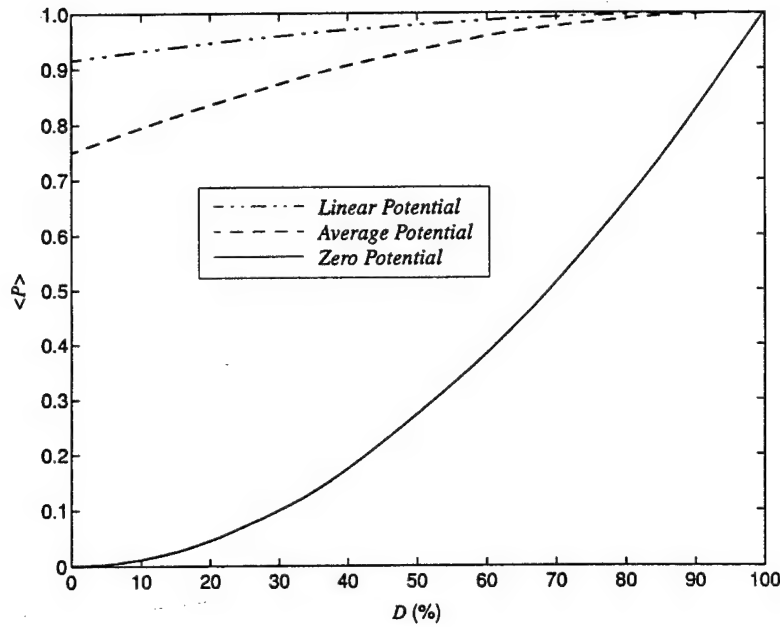


Figure A.4.12: Normalized peak mechanical power plotted as a function of the stator electrode duty ratio  $D$ . The duty ratio is the ratio between the area of the electrodes and the area of the inter-electrode insulating gaps. Each curve is for a different assumed potential function across the inter-electrode insulating gap.

The decrease in power is related to the dependence of power on active machine area but is tempered by the nature of the electric fields across the insulating inter-electrode gap.

In the baseline design, the inter-electrode insulating gap is a constant width from the inner radius of the stator electrodes to the outer radius. This gap could be opened only as far as the inner radius allows. Yet wider gaps could be obtained at the outer radius where viscous drag is most severe. Therefore to obtain the results shown in Figure A.4.12, the gap is allowed to grow linearly with radius, and the fraction of the stator covered by electrodes is referred to as the duty ratio.

To simplify the analysis, the development of the 3D multiple-harmonic model begins by assuming a potential distribution between the stator electrodes. As the inter-electrode gap widens, the assumed potential takes on greater significance. To illustrate this, Figure A.4.12 shows results given three different assumptions: a time-harmonic spatially linear function, a time-harmonic spatially constant average, and a time-invariant spatially constant zero potential. Which case is applicable in the baseline design is not known exactly because it depends in part upon the cleanliness of the exposed insulator surface between the electrodes. However, it is clear that this issue requires further study since the baseline design effectively has a duty ratio of 50–75%.

#### A.4.4 Summary

This section described the 3D multiple-harmonic model. This model accounts for the finite

number and discrete widths of the stator electrodes, and gives more accurate results for expected electric induction motor performance. In general, this model predicts slightly decreased performance over that of the 3D single-harmonic model which is based on the fundamental spatial harmonic of stator potential. Nonetheless, it is observed that the single-harmonic model is quite accurate, and so it may be considered a very useful design tool. The most significant issue for which this is not the case, and thus requires the 3D multiple-harmonic model for study, is when accounting for the potential distribution between widely spaced stator electrodes.

### **A.5 Conclusion**

This appendix described the present suite of temporal steady-state electromechanical models which are used to understand the micro-scale electric induction motor hosted by the Tethered Motor and the Motor-Compressor. The results described in Section A.3 and Section A.4 were used to arrive at the baseline design presented in Table A.3.1 and Table A.4.1. In each section, the discussion sought to explain some of the many issues which gave rise to the most important aspects of the baseline design. In summary, micro-scale electric induction machine performance based on these results is improved by a thicker rotor insulator, a higher periodicity, and a smaller air gap length. Also, slightly lower rotor film sheet conductivities were shown to improve machine performance based on the steady-state models but its current value provides a wider rotor tip speed operating regime. Finally, this analysis has shown that the form of the potential across the inter-electrode insulating gap requires deeper study.

### **A.6 References**

- 1) M. Zahn; Electromagnetic Field Theory: A Problem Solving Approach; John Wiley & Sons, New York, 1979.
- 2) C. T. A. Johnk; Engineering Electromagnetic Fields and Waves; John Wiley & Sons, New York, 1988.
- 3) H. Woodson and J. Melcher; Electromechanical Dynamics; Vols. 1 and 2, John Wiley & Sons, New York, 1968.
- 4) S. F. Bart; "Modeling and Design of Electroquasistatic Microactuators;" Ph.D. Thesis, Massachusetts Institute of Technology, Cambridge, MA, September 1990.
- 5) F. Paschen; "Ueber die zum Funkenübergang in Luft, Wasserstoff und Kohlensäure bei verschiedenen Drucken erforderliche Potentialdifferenz;" *Annalen der Physik*, **37**, 69-96, 1889.

## APPENDIX B - ANALYSIS OF THE MOTOR GAP VISCOUS FLOW

This appendix describes the analysis of viscous flows typical to micro motors developed for Power MEMS, such as the micro motor-compressor. The aim of this analysis was to improve our prediction of the drag in the motor gap and determine the possible drag reduction due to a grooved stator. The first section describes the problem which is analysed. The next sections detail the analysis of smooth and grooved motor gap flows, followed by the main conclusions.

### B.1 Problem Statement

As described in section 9 of this report, we are developing a radial compressor of 4 millimeters in diameter, spinning at a desired wheel speed of 400 m/s, which is driven by an electric induction motor. The rotating structure is simply a disk which supports the impeller blades on the front side and the electric motor on the back side, as shown in Figure B.1.

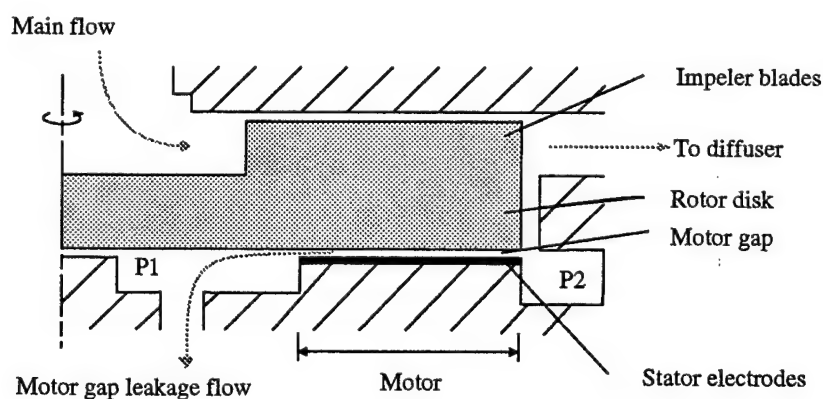


Figure B.1: Cross-section of the motor-compressor. The main flow comes in axially, flows through the impeller and then through the diffuser (not shown). A secondary flow leaks through the motor gap, from the outer radius of the motor gap (P2) to the inner radius (P1).

The electric motor applies torque to the disk by “dragging” induced charges in the material on the back side of the disk. These charges are induced and dragged by a potential field created on the surface underneath the disk. This electric stator is formed of discrete radial electrodes on which an alternating voltage is applied.

Induction motor modeling states that the applied torque is inversely proportional to the motor gap, such that system design pushes the motor gap to very small values (nominally 3 microns) in order for the motor to produce the required amount of power. Unfortunately,



this combination of a high speed rotating disk over a very small air gap results in large viscous losses. The power viscously dissipated in the motor gap has two main impacts on the system:

1. Reduces the net power output from the motor (limiting the available power for compression work);
2. Increases the temperature of the device, since the viscous dissipation acts as a heat source.

This document focuses on the first item by presenting the approach used to calculate the motor gap viscous dissipation and strategies to reduce it. First, the analysis of the motor gap flow with a smooth stator is summarized, followed by the flow between a spinning disk and a grooved stator (radial grooves). Other strategies for drag reduction are then presented and discussed. The focus is on understanding the origin of the drag on the disk in order to, as accurately as possible, predict and eventually reduce the dissipated power. The methods used to for calculating the flow field are both analytical and numerical, which details will not be presented herein. The numerical results presented were obtained using a commercial CFD package (Fluent) which solves the Navier-Stokes equations using a Pressure-based segregated solution scheme with a second order accurate, cell centered, finite-volume discretization<sup>1</sup>. For the calculations presented in this document, the flow in the motor gap is assumed to be steady and laminar<sup>2</sup>. Since viscous heating will affect the drag through changes in viscosity (and in some cases density), the predicted drag will be a function the thermal balance of the device. To concentrate on the flow field, this aspect will be factored out here by assuming a constant viscosity.

---

<sup>1</sup>This solution approach has been widely used and approved by the CFD community over the past decade.

<sup>2</sup>No turbulence is therefore used, such that the Navier-Stokes equations are solved directly

## **B.2 Smooth stator motor gap flow**

The motor gap can be modeled as an annular disk extending from  $r_{mi}$  to  $r_{mo}$  and rotating over a flat surface. Static pressures are applied at the outer radius ( $P2$ ) and inner radius ( $P1$ ), where  $P2 > P1$  for the nominal motor-compressor configuration. The following sections will discuss the flow features in the motor gap for a smooth stator configuration and derive simple approximations for drag prediction.

### **B.2.1 Simplified flow field**

First, the flow will be assumed incompressible and the effects of rotation will be neglected. The following sections describe the motor gap flow under these conditions, then introduces the effects of rotation and entrance lengths.

**Radial velocity profile** When rotation is neglected, radial flow in the motor gap is similar to *poiseuille flow* with varying area. The radial velocity profile is then parabolic, formed by the balance between the radial pressure gradient and the radial shear on both the disk and the stator (which impose  $V_r = 0$  at these boundaries). This radial velocity profile determines the mass flow through the motor gap, but does not affect the tangential drag on the disk (when rotation is neglected).

**Tangential velocity profile** Flow in the tangential direction is similar to *couette flow*, where velocity varies linearly between a stationary plate and a parallel plate moving at a velocity  $U = \Omega r$ . The shear stress on the moving plate corresponds to a drag force, (or torque on the disk). The force (or torque) multiplied by the plate velocity (or rotation rate) is the power required to sustain motion. Reduction of the shear stress is therefore a metric for comparing drag reduction approaches.

Furthermore, this power is dissipated as heat in the fluid, which increases the temperature, the viscosity and therefore the torque. Conceptually, the proportional trend of the viscosity coefficient with temperature is a vicious circle amplifying the detriment of a high viscous drag motor design.

**Simple power dissipation model** When rotation is neglected, the solution for drag on the disk is found by integrating the tangential shear stress due to couette flow on the motor gap. We can express the torque ( $T$ ) as the integral of the shear stress ( $\tau_\theta$ ) from the inner to

outer radius<sup>3</sup>:

$$\tau_\theta = \mu \frac{\partial V_\theta}{\partial z} = \mu \frac{\Delta V_\theta}{\Delta z} = \mu \frac{\Omega r}{g_m} \quad (\text{B.1})$$

$$\begin{aligned} T &= \int_{r_{mi}}^{r_{mo}} r \tau_\theta dA = \int_{r_{mi}}^{r_{mo}} \tau_\theta \times 2\pi r^2 dr \\ T &= \int_{r_{mi}}^{r_{mo}} \mu \frac{\Omega r}{g_m} \times 2\pi r^2 dr = \mu \frac{2\pi\Omega}{g_m} \int_{r_{mi}}^{r_{mo}} r^3 dr \\ T &= \mu \frac{\pi\Omega}{2g_m} (r_{mo}^4 - r_{mi}^4) \end{aligned} \quad (\text{B.2})$$

The viscous work done by the disk on the motor gap fluid is then :

$$\begin{aligned} \dot{W}_{visc} &= T\Omega \\ \dot{W}_{visc} &= \mu \frac{\pi\Omega^2}{2g_m} (r_{mo}^4 - r_{mi}^4) \end{aligned} \quad (\text{B.3})$$

The dissipated power, which reduces the net output power of the motor, is therefore proportional to the fluid viscosity (i.e. temperature), inversely proportional to the motor gap ( $g_m$ ), and proportional to the rotational speed squared. To make the radius dependence more explicit, Eqn B.3 can be formulated as a function of area and wheel speed at the outer radius ( $\Omega r_{mo}$ ) by setting  $r_{mi} = 0$ :

$$\dot{W}_{visc} = \mu \frac{(\pi r_{mo}^2)(\Omega r_{mo})^2}{2g_m} \quad (\text{B.4})$$

The dissipated power therefore tends to be proportional to the area and to the square of  $\Omega r_{mo}$  (as  $r_{mi}$  tends to zero).

**B.2.2 Effects of rotation** For high angular velocities, we can expect rotation to affect the velocity profiles. One approach to view the effects of rotation is to evaluate the magnitude of the Coriolis and centrifugal terms in a rotating reference frame. If the momentum equations are written in a frame rotating with the fluid at a given axial position (i.e.  $\Omega_{r.f.} = V_\theta/r$ ), then the relative tangential velocity ( $V'_\theta$ ) is zero. The fictitious centrifugal and Coriolis forces per unit mass, due to the non-inertial frame, are then:

$$\vec{F}_{cent} = -\vec{\Omega}_{r.f.} \times (\vec{\Omega}_{r.f.} \times \vec{r}) = \frac{V_\theta^2}{r} \hat{e}_r \quad (\text{B.5})$$

$$\vec{F}_{cori} = -2\vec{\Omega}_{r.f.} \times \vec{V}_r = -2\frac{V_\theta V_r}{r} \hat{e}_\theta \quad (\text{B.6})$$

where the unit vector  $\hat{e}_r$  is in the outward direction, and  $\hat{e}_\theta$ , in the direction of disk rotation.

---

<sup>3</sup>Variables are defined as: axial component ( $z$ ), radial component ( $r$ ), motor gap ( $g_m$ ), rotation rate ( $\Omega$ ) and viscosity coefficient ( $\mu$ ), inner and outer radius  $r_{mi}$  and  $r_{mo}$  respectively

Since these forces depend on the magnitude of the tangential velocity ( $V_\theta$ ), they will be more prevalent near the disk (where  $V_\theta$  is large) than near the stator (where  $V_\theta$  tends to zero). When these forces are important, they will modify the tangential and radial velocity profiles so the drag may not be accurately predicted by the Couette flow approximation. The following paragraphs quantify the importance of these forces.

**Centrifugal force** The centrifugal force will change the radial velocity profile. Since the centrifugal force is directed outward (Eqn B.5), it creates larger radial velocities near the disk compared to the expected parabolic profile. The analytical solution for the radial velocity profile<sup>4</sup> at different pressure ratios ( $P2/P1$ ) are shown in Figure B.3 (as the solid line), along with a numerical solution from Fluent (as the  $\times$  symbols) for incompressible flow. They confirm the expected trends and show that the radial velocity is noticeably affected only when the external pressure ratio is less than 1.5, for the nominal speed and geometry of the motor-compressor.

The centrifugal force affects the mass flow through the motor gap, but will only affect the drag on the disk (tangential velocity profile) through  $V_r$  in the Coriolis force expression (Eqn B.6). It is therefore important for drag prediction only when the Coriolis force is also important.

**Coriolis force** The Coriolis force will directly change the linear tangential velocity profile into a profile similar to a combined Couette-Poiseuille flow, as shown in Figure B.2. From Eqn B.6, the force will be in the direction of rotation for inward radial velocities ( $V_r < 0$ ) and opposite to rotation for outward radial velocities ( $V_r > 0$ ). Inward radial velocities (when  $P2 > P1$ ) have the effect of reducing the tangential velocity gradient near the disk, therefore reducing the drag. The opposite applies for outward radial velocities, in which case the shear stress will increase. The Coriolis force can be detrimental if  $P2 < P1$ , and should be avoided not to increase the drag.

This effect can also be described using conservation of angular momentum in an absolute reference frame. As a swirling inviscid fluid moves radially inward, angular momentum is conserved by increasing the tangential velocity ( $V_\theta r = \text{constant}$ ). However, the no-slip condition at the disk reduces the tangential velocity of the fluid as it flows inward ( $\frac{V_\theta}{r} = \text{constant}$ ). The ratio of viscous forces to angular inertial forces will determine which effect dominates. If the inertial forces are important enough, the tangential velocity profile will be similar to a combined Couette-Poiseuille flow, reducing (or increasing) the shear stress at the disk.

By comparing the magnitudes of the relevant inertial and viscous terms in the momentum

---

<sup>4</sup>The analytical solution is not presented in this document.

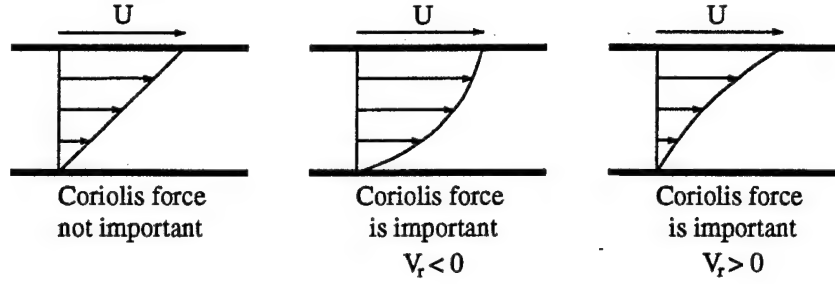


Figure B.2: Three tangential velocity profiles for situations where the Coriolis force is negligible, acting in the direction of rotation, or acting opposite to the direction of rotation.

equation, we can define a non-dimensional (Reynolds-like) number<sup>5</sup>. The convective inertial term can be approximated as:

$$V_r \frac{\partial V_\theta}{\partial r} \sim W \frac{\Omega r}{r} = W\Omega \quad (\text{B.7})$$

where  $W$  is a representative radial velocity. The viscous term can be approximated as:

$$\nu \frac{\partial^2 V_\theta}{\partial z^2} \sim \nu \frac{\Omega r}{g_m^2} \quad (\text{B.8})$$

The ratio of these two terms is then:

$$\frac{\text{inertial forces}}{\text{viscous forces}} \sim \frac{W g_m^2}{\nu r} \quad (\text{B.9})$$

More insight can be gained however by expressing the ratio as:

$$\frac{\text{inertial forces}}{\text{viscous forces}} \sim \frac{W\Omega}{\nu \frac{\Omega r}{g_m^2}} = \frac{W}{\Omega r} \frac{g_m^2}{\nu/\Omega} \quad (\text{B.10})$$

We can identify  $\sqrt{\nu/\Omega}$ , which characterizes a viscous diffusion length, so the non-dimensional ratio can be written as:

$$\frac{\text{inertial forces}}{\text{viscous forces}} \sim \left( \frac{W}{\Omega r} \right) \left( \frac{g_m}{\sqrt{\nu/\Omega}} \right)^2 \quad (\text{B.11})$$

We can therefore state that the Coriolis force will gain importance, as the motor gap ( $g_m$ ) increases compared to the viscous diffusion length<sup>6</sup> ( $\sqrt{\nu/\Omega}$ ) and when the radial velocity

<sup>5</sup>The literature on rotating flows normally uses the Rossby number ( $R_o = \frac{\text{Inertial forces}}{\text{Coriolis forces}}$ ) and the Eckman number ( $E_k = \frac{\text{Viscous forces}}{\text{Coriolis forces}}$ ) to describe the importance of the Coriolis effects. The non-dimensional ratio used here is actually a combination of both these numbers:  $\frac{\text{Inertial forces}}{\text{Viscous forces}} = \frac{R_o}{E_k}$ .

<sup>6</sup>For the Rayleigh problem, where a plate is suddenly put into translation, the thickness of the boundary layer develops in time proportionally to  $\sqrt{\nu t}$ . Similarity with our case is found by replacing  $t$  by  $1/\Omega$ .

( $W$ ) increase compared to the tangential velocity ( $\Omega r$ ). For the nominal motor-compressor configuration, the value of the above non-dimensional number is:

$$\frac{W}{\Omega r} \sim \frac{15m/s}{300m/s} = 0.05 \quad (B.12)$$

$$\frac{g_m}{\sqrt{\nu/\Omega}} \sim \frac{3}{\sqrt{\frac{2.2e-5}{1 \times 200000}}} \sim \frac{3\mu m}{10\mu m} = 0.3 \quad (B.13)$$

$$\frac{\text{inertial forces}}{\text{viscous forces}} \sim \left(\frac{W}{\Omega r}\right) \left(\frac{g_m}{\sqrt{\nu/\Omega}}\right)^2 \sim 0.05 \times 0.3^2 = 0.0045 \quad (B.14)$$

Since this number is small, the Coriolis force is not expected to modify the tangential velocity profile, or in other words, the viscous forces will overcome the inertial (or Coriolis) forces and impose a linear tangential velocity profile. The drag can therefore be approximated by the couette flow solution for our nominal motor-compressor configuration. Since the non-dimensional ratio is proportional to the square of the gap, and since increasing  $g_m$  allows for higher radial velocities (larger  $V_r$ ), increasing the motor gap will make the Coriolis effect more prevalent. These effects are confirmed by Figure B.4, which shows numerical results for the tangential velocity profile at mid-radius for  $3\mu m$  and  $10\mu m$  gaps.

### B.2.3 Entrance length effects

The previous analytical solution neglected the development of boundary layers as the flow enters at the outer radius. Two types of entrance lengths characterize the motor gap problem:

- distance over which the *tangential velocity profile* develops into a couette flow (affects the torque on the disk);
- distance over which the *radial velocity profile* develops into a poiseuille flow; (affects the mass flow through the motor gap).

Numerical solutions of the axisymmetric flow in the motor gap are shown in Figure B.5. The curves show the tangential velocity versus radius at mid-gap, for  $3\mu m$  and  $10\mu m$  gaps. Flow enters at the outer radius with zero tangential velocity. We notice the very short entrance length for the nominal  $3\mu m$  gap<sup>7</sup>. In the entrance region, the shear stress at the disk is larger than couette flow since the tangential velocity of the fluid in the gap is initially zero, while at the disk  $V_\theta = \Omega r$ . More work is done on the entering fluid since angular momentum must be imparted to the core flow.

---

<sup>7</sup>Since the gap is orders of magnitudes less than the radius, the effect of this entrance length is expected to be secondary for small gaps

To quantify the magnitude of rotation and entrance length effects, numerical results for axisymmetric flow are compared to the couette flow approximation. Table B.1 summarizes the power needed to sustain rotation ( $T \times \Omega$ ) for  $3\mu m$  and  $10\mu m$  gaps with pressure ratios of 2:1 and 4:1.

Configuration			Power (W)		
Gap	Pressure ratio	Inlet $V_\theta$	2-D axisymmet- ric computation	Couette flow approximation	% increase from couette flow
$3\mu m$	2:1	0 m/s	6.95	6.91	0.5%
	4:1	0 m/s	6.95	6.91	0.5%
$10\mu m$	2:1	0 m/s	2.16	2.07	4%
	4:1	0 m/s	2.27	2.07	10%
	4:1	150 m/s	1.93	2.07	-7%

Table B.1: Viscous drag on the disk from 2-D axisymmetric computations and the couette flow approximation (Eqn B.3).

We first notice that the deviations from the couette flow approximation are negligible for the nominal motor-compressor configuration ( $3\mu m$  gap). Entrance length and rotation effects are apparent for the  $10\mu m$  gap. We notice that the drag reduction due to the Coriolis effect is overtaken by the increase in drag due to the entrance length, so the drag is actually larger than the couette flow approximation. When the entrance length is reduced, by applying a uniform inlet tangential velocity of  $\Omega r/2$ , the calculations show a net reduction in drag. In this case, the Coriolis drag reduction is larger than the entrance drag increase. Comparing the results as a function of pressure ratio, we notice the insensitivity of the nominal configuration, while the larger motor gap drag is affected.

**Conclusion** To summarize, the Coriolis and centrifugal forces as well as the entrance lengths do not significantly affect the tangential velocity profile for the motor-compressor nominal configuration. The viscous dissipation can therefore be predicted by Eqn B.3, which assumes a linear tangential velocity profile (couette flow).

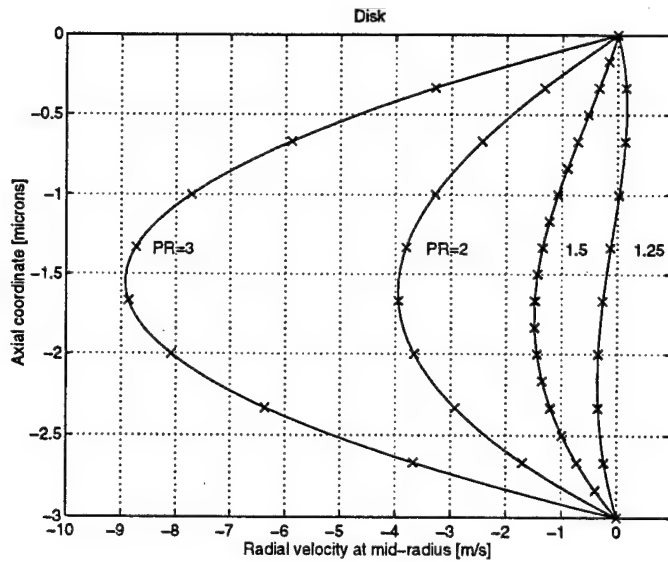


Figure B.3: Radial velocity profiles across the gap (mid-radius) for different pressure ratios ( $P_2/P_1$ ). The centrifugal force tends to induce outward radial flow ( $V_r > 0$ ) near the disk, opposite to the inward radial flow created by the external pressure ratio.

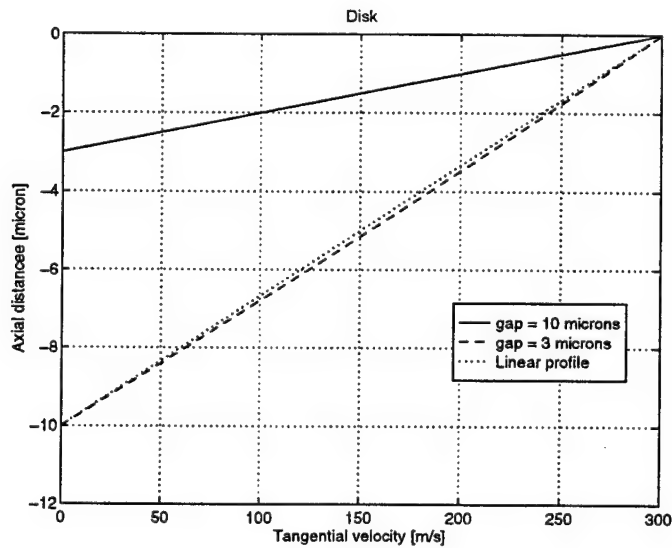


Figure B.4: Tangential velocity at mid-radius across  $3\mu m$  and  $10\mu m$  gaps. Larger gap shows a slight decrease in shear stress on the disk which is due to the Coriolis force (dotted line is a linear velocity profile).



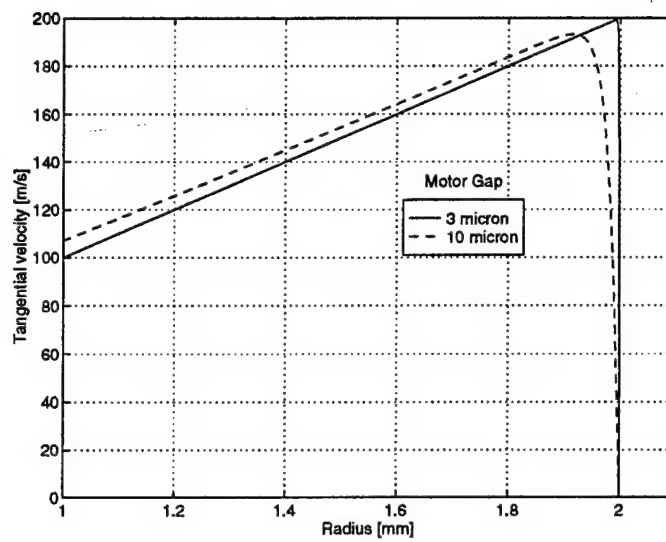


Figure B.5: Tangential velocity versus radius at mid-gap, for motor gaps of  $3\mu m$  and  $10\mu m$ . Entrance length for the nominal motor-compressor configuration ( $3\mu m$ ) is negligible. (Results from 2-D axisymmetric calculations with  $V_\theta = 0$  at the inlet -  $r = 2mm$ ).

### B.3 Grooved stator motor gap flow

One feature to reduce the drag on the disk consists of locally increasing the motor gap wherever possible. Given the requirement for the stator electrodes to remain near the rotor, all other area under the disk other than electrodes can be recessed. In particular, the radial strips between each electrode can be etched, creating 300-500 thin radial trenches on the stator surface. This section first summarizes the flow features of a grooved motor gap, based on a nominal geometry. Then, a parametric method for predicting the drag given any geometry is presented. Such a prediction tool is useful to assess design trade-offs between electric power and viscous drag while designing the motor-compressor.

#### B.3.1 Geometry

A cross section (normal to the radial direction) of the motor gap region is shown in Figure B.6, labeled with the main geometric parameters describing the geometry at a given radius: the motor gap height ( $g_m$ ), the electrode and trench widths ( $w_e$  and  $w_t$  respectively) and the trench depth ( $h_t$ ).

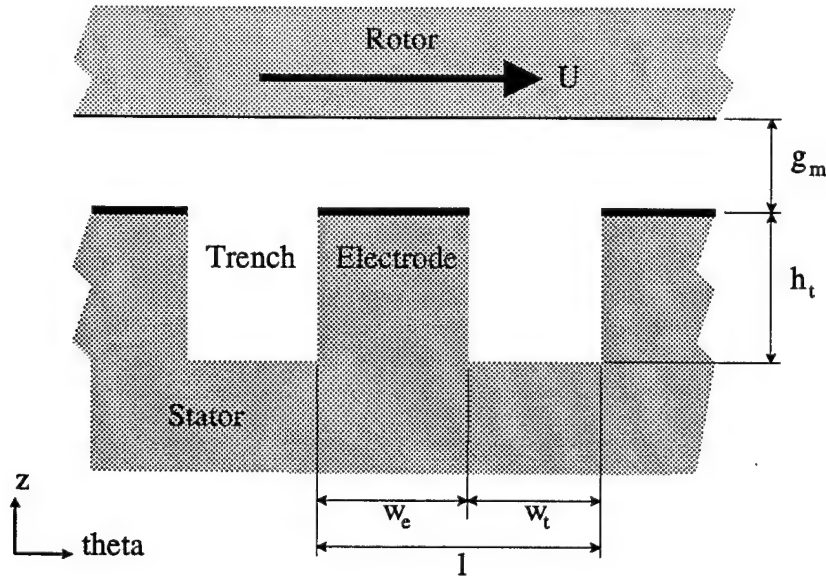


Figure B.6: Cross-section of the motor gap and the stator electrodes (view is normal to the radial direction)

Instead of directly using the widths  $w_e$  and  $w_t$ , it is convenient to use the width of an electrode-trench pair ( $l = w_e + w_t$ ) and the following ratio, referred to as the duty-cycle ( $dc$ ):

$$dc = \frac{w_e}{w_e + w_t} = \frac{w_e}{l}$$

The duty-cycle will tend to 100% as the electrodes are wider and the trenches are narrower.

### **B.3.2 Grooved stator flow features**

A 3-D numerical solution of the motor gap flow for the nominal motor-compressor parameters was first calculated to identify the physical features. The computational domain consisted of the fluid gap between the spinning disk and the stator, extending circumferentially over one electrode-trench pair (with periodic boundary conditions in the tangential direction) and extending radially from the motor inner to outer radius (with a pressure of 2 atm. at the outer radius and 1 atm. at the inner radius).

Figure B.7 shows the velocity vectors in a cross section of the motor gap for a nominal trench geometry ( $dc = 50\%$ ,  $h_t = 20\mu m$ ,  $l = 20\mu m$ ,  $\Omega r = 300m/s$ ). The resulting flow field is characterized by a couette-type flow in the gap region and a vortex in the trench.

The drag mechanism of high shear at the disk surface remains present, although slightly modified, as shown by the tangential velocity profiles in Figure B.8. Each curve corresponds to a different circumferential location, identified by vertical lines in the right view of Figure B.7. The disk is located at  $z = 0$ , the electrode surface, at  $z = -3\mu m$ , and the bottom of the trench, at  $z = -20\mu m$ . The point to notice is the uniformity of the slope of tangential velocity at the disk, over the electrode as well as over the trench. The desired reduction in drag is therefore not expected to be noticeable. Once again we can assume that the radial flow does not affect the tangential velocity profile near the disk when the Coriolis and centrifugal forces are negligible in the gap region. To confirm this, tangential velocity profile from the 3-D calculation are compared to those from a 2-D calculation in Figure B.8. The 2-D calculation is obtained for the flow in a cross section at mid-radius (as illustrated in Figure B.6). The profiles are shown to be almost identical, confirming the assumption that the effects of rotation are negligible for the grooved stator nominal configuration of the motor-compressor.

The flow in the trench is characterized by a radial vortex aligned along the trench and positioned near the gap region (top of the trench). Figure B.9 illustrates this by tracking fluid particles seeded across the gap and trench. The vortex is shown by swirling particles in the top region of the trench. Radial through-flow near the bottom of the trench is illustrated by the lower particle paths.

Radial velocities in the trench (not shown here) form profiles similar to poiseuille flow in a rectangular pipe (once developed).

### **B.3.3 Drag prediction with a grooved stator**

The complex 3-D problem can be simplified for means of drag prediction while designing the motor-compressor system. The total torque on the disk can be determined by numerically integrating the torque for annular slices of width  $dr$ . The drag per unit radius,  $f = \frac{\text{force}}{dr}$ , can be determined by calculating the 2-D flow in many cross sections as shown

in Figure B.6 but with the parameters depending on the radial location of the cross section. In this approach, the rotation and entrance effects are neglected. Empirical corrections could however be applied.

To be useful for design, the drag per unit radius will be expressed as a function of the minimal non-dimensional numbers. The dependence of drag on these non-dimensional numbers will then be determined computationally by varying the numbers in the expected ranges, creating an table for drag per unit radius for the various configurations.

### Non-dimensionalization

The drag in a 2-D cross section of the grooved stator motor gap depends on the following 7 independent parameters, which have units formed by 3 fundamental dimensions: mass (M), length (L) and time (T):

Parameter		Dimensions
Gap height,	$g_m$	$L$
Electrode+trench width,	$l$	$L$
Trench depth,	$h_t$	$L$
Duty-cycle,	$dc$	-
Velocity of the disk,	$U = \Omega r$	$L/T$
Viscosity coefficient,	$\mu$	$M/LT$
Density,	$\rho$	$M/L^3$

Table B.2: Independent parameters .

The dependent variable, drag per unit radius ( $f$ ), can be expressed generally as a nonlinear function of the 7 independent variables:

$$f = \Psi(g_m, l, h_t, dc, U, \mu, \rho) \quad (B.15)$$

Based on the Buckingham-II theorem, we can reduce the number of independent variables by the number of fundamental dimensions. In this case, we can reduce the number of independent variables from 7 to 4. The dimensionally independent subset of the independent variables is chosen as  $\{g_m, U, \mu\}$ . The drag per unit radius ( $f$ ) and the 4

remaining independent variables can be defined in dimensionless form as:

$$f^* = \frac{f}{\mu U} \quad (\text{B.16})$$

$$l^* = \frac{l}{g_m} = \frac{w_e + w_t}{g_m} \quad (\text{B.17})$$

$$h^* = \frac{h_t}{g_m} \quad (\text{B.18})$$

$$dc = \frac{w_e}{w_e + w_t} \quad (\text{already non-dimensional}) \quad (\text{B.19})$$

$$\rho^* = \frac{\rho U g_m}{\mu} = Re_g \quad (\text{B.20})$$

The functionality is therefore reduced to:

$$f^* = \Psi^*(l^*, h_t^*, dc, Re_g) \quad (\text{B.21})$$

**Non-dimensionalized solution for the smooth stator** It is informative to apply this non-dimensionalization to the motor gap flow with a *smooth stator*. Without the trenches, the drag per unit radius is only a function of 4 independent variables:  $g_m, l, U, \mu$ . The analytical dependence of drag per unit radius is given by Eqn B.1 for  $\tau_\theta$ , multiplied by the length  $l$ :

$$f_{smooth} = \mu \frac{U}{g_m} l = \Psi_{smooth}(g_m, l, U, \mu) \quad (\text{B.22})$$

which is written in non-dimensional form by dividing both sides by  $\mu U$  and noting that  $l^* = l/g_m$ :

$$f^*_{smooth} = l^* \quad (\text{B.23})$$

$$f^*_{smooth} = l^* = \Psi^*_{smooth}(l^*) \quad (\text{B.24})$$

We notice that the Reynolds number,  $Re_g$ , is not a parameter in the couette flow solution since density (representing inertial forces) does not affect the drag. Therefore, the Reynolds number mainly characterizes the trench flow (i.e. the vortex) as opposed to the flow in the gap region. The ratio of viscous to inertial forces will however determine the entrance lengths in the gap region for both the smooth or grooved stators.

## Numerical results

The drag on the disk for the grooved stator configuration was calculated over a test matrix with 27 components formed by varying each of the 3 geometric non-dimensional number

( $l^*$ ,  $h_t^*$ , and  $dc$ ) over 3 values in their expected range. For this initial data set, the Reynolds number was kept constant to a nominal value of 55:

$$Re_{g,nom} = \frac{\rho U g_m}{\mu} = \frac{1.225 \text{ kg/m}^3 \times 300 \text{ m/s} \times 3 \mu\text{m}}{2.2 \times 10^{-5} \text{ kg/ms}} = 55 \quad (\text{B.25})$$

since the effect of Reynolds number is proposed to be of second order. Future work should extend the test matrix to include the dependence on Reynolds number.

The calculated drag for the grooved stator configuration ( $f^*$ ) is best expressed as a drag reduction coefficient ( $C_d$ ) applied to the drag for the smooth stator configuration ( $f_{smooth}^*$ , given by Eqn B.24):

$$f^* = (1 - C_d) f_{smooth}^* \quad (\text{B.26})$$

$$C_d = 1 - \frac{f^*}{f_{smooth}^*} = 1 - \frac{f^*}{l^*} \quad (\text{B.27})$$

The computational results for  $f^*$  as a function of  $l^*$ ,  $h_t^*$ , and  $dc$  are shown in Figures B.10, B.11, and B.12. First and foremost, we notice that the maximum drag reduction levels below 30% for low duty-cycles, deep trenches and wide electrodes (and trenches). *This drag reduction approach is therefore limited.* The following paragraphs comment on the trends of drag reduction with respect to the 3 geometric parameters.

**Duty-cycle,  $dc$**  We notice from Figure B.10, that the drag reduction is larger at low duty-cycle (wide trenches compared to electrodes), which is intuitively expected since more disk area is at a larger gap when the duty-cycle is lowered. Also, the drag reduction is approximately linear with duty-cycle. We must also note that the drag reduction tends to zero for a duty-cycle of 90%. Very thin trenches compared to the electrodes are therefore not useful.

**Trench depth,  $h_t^*$**  The drag reduction as a function of trench depth (shown in Figure B.11) increases rapidly at shallow depths but asymptotes as the trenches are deeper. Although more calculations at low  $h_t^*$  are needed to better define maximum useful depth, it can be approximated as 1 to 3 gap heights, depending intuitively on the aspect ratio of the trench ( $w_t/h_t$ ).

**Sector length,  $l^*$**  The effect of increasing the electrode+trench length as shown in Figure B.12 appears to increase drag reduction, approximately following a linear trend.

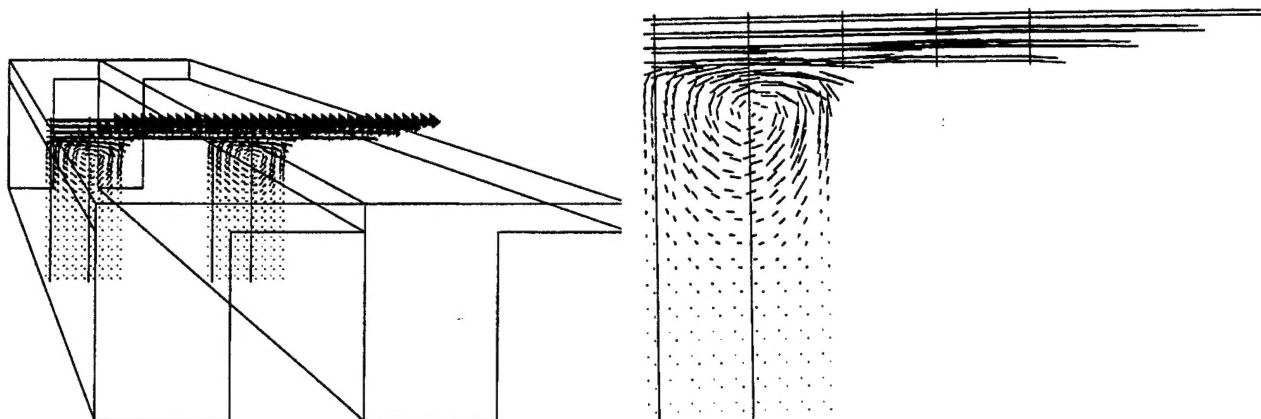


Figure B.7: Velocity vectors in a cross section of the motor gap for a nominal trench geometry ( $dc = 50\%$ ,  $h_t = 20\mu m$ ,  $l = 20\mu m$ ,  $\Omega r = 300m/s$ ). The left view shows two trenches and electrodes directed radially out of the page. The top surface is the rotating disk.

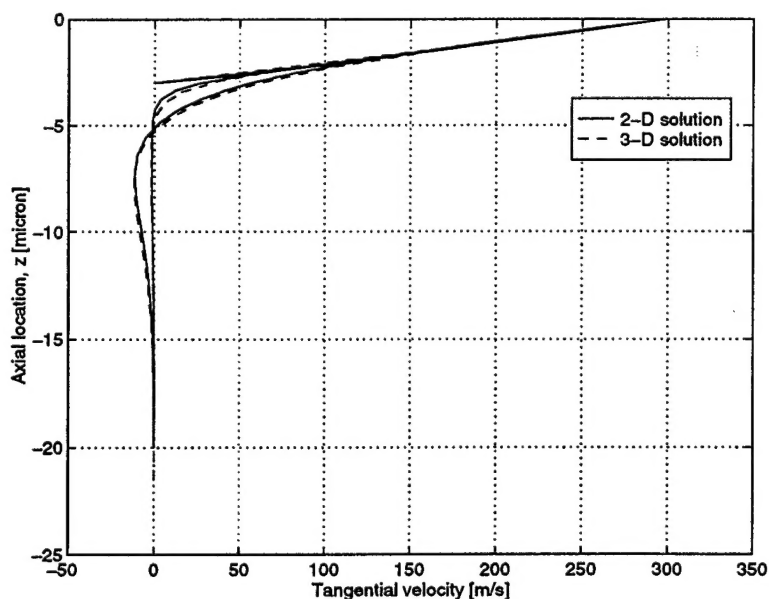


Figure B.8: Tangential velocity profiles from 3-D and 2-D calculations, showing that the 2-D solution predicts well the shear stress. Curves correspond to different circumferential location identified by the vertical lines in the cross section of Figure B.7

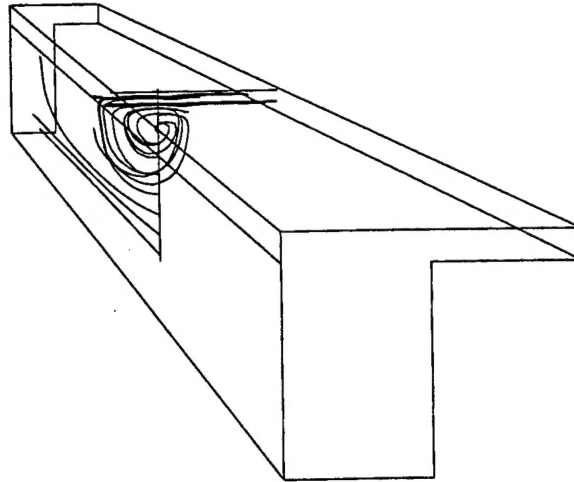


Figure B.9: Particle traces showing the vortex on the top region of the trench and the through-flow at the bottom of the trench.

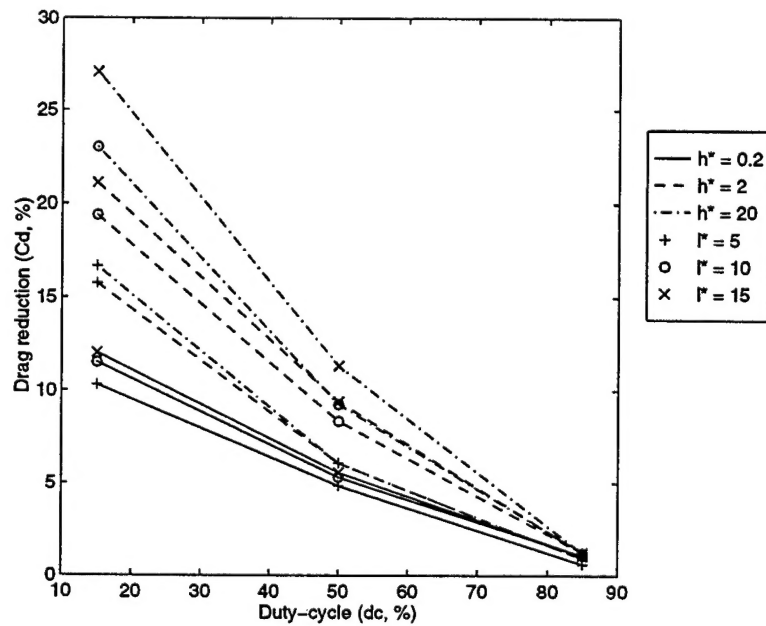


Figure B.10: Drag reduction coefficient as a function of duty-cycle (100% duty-cycle corresponds to the smooth stator).



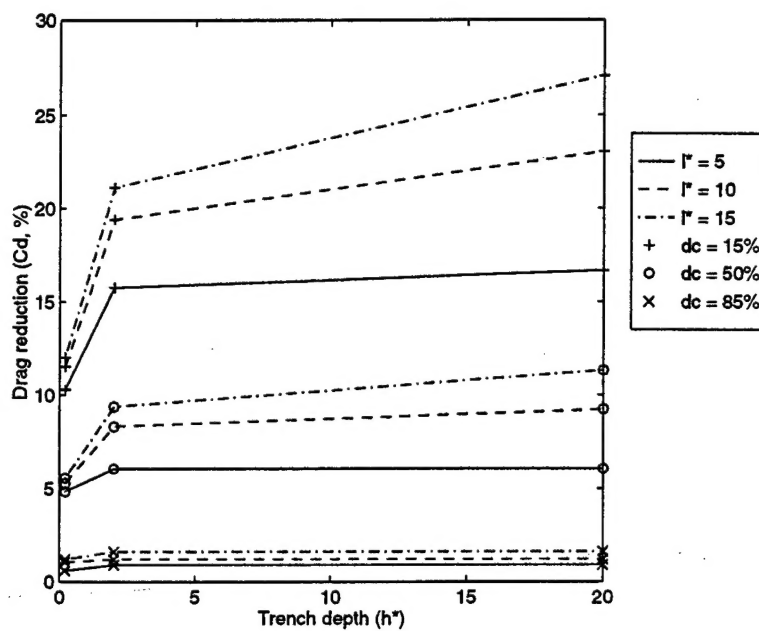


Figure B.11: Drag reduction coefficient as a function of non-dimensional trench depth ( $h_t^* = h_t/g_m$ ).

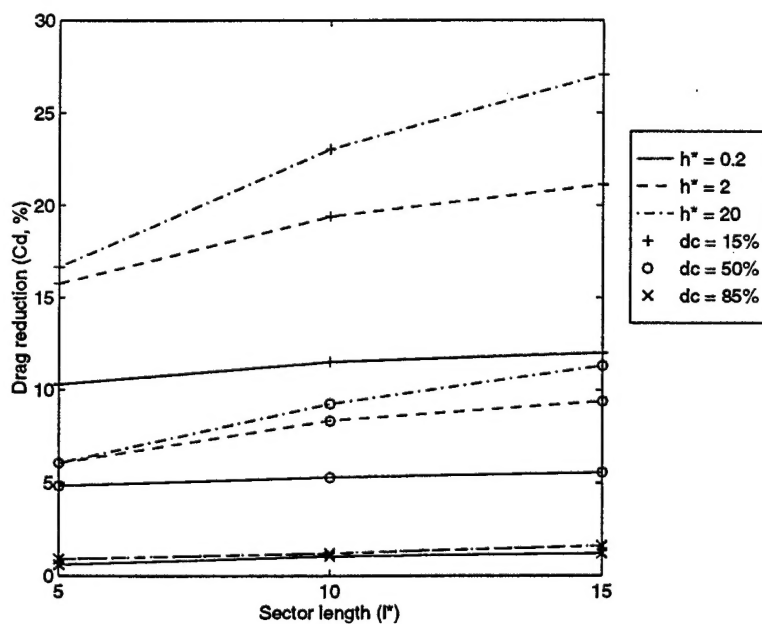


Figure B.12: Drag reduction coefficient as a function of non-dimensional sector length of an electrode+trench pair ( $l^* = (w_e + w_t)/g_m$ ).

#### **B.4 Conclusion**

Overall, drag in this motor gap is mainly dominated by the couette flow established between the stationary electrodes and the rotating disk. Locally increasing the gap between the electrodes, such to produce a radially grooved stator, does not dramatically decrease the drag. The constraint of small gaps imposed by the motor electrical design combined with the high speeds desired for a high power-density device seem intrinsically detrimental. Various modifications to the simple grooved stator configuration (not presented here) have also been evaluated but without much more drag reduction than the simple grooved stator. Further investigation on these and other possible drag reduction features are however necessary before implementing them in a device. Many other components of the motor-compressor already introduce large uncertainty in successful operation of the device, so extra risk incurred by uncertain motor gap fluid dynamics should be avoided, unless the proposed drag reduction is considerable.

The first version of the motor-compressor will therefore feature radial grooves between the electrodes. The trenches will however be limited to the thickness of the electrodes, reducing the fabrication complexity. The trench geometry of the next motor-compressor will be defined from an overall system design perspective, which considers trade-offs between the motor electrical power and the viscous losses. The modeling approach described in the last section will be used to evaluate the motor gap viscous losses. Investigation of other drag reduction mechanisms will be pursued during the next year, in parallel with the device development.